UNIVERSITY OF TROMSØ

FYS-3900

MASTER'S THESIS IN PHYSICS

Numerical studies of radial filament motion in toroidally confined plasmas

Ralph KUBE

May 18, 2010

Faculty of Science and Technology
Department of Physics and Technology
University of Tromsø

Acknowledgements

First of all, I would like to thank my supervisor Professor Odd Erik Garcia for his excellent mentoring. He has been very supportive and always found time for clarifying discussions. I learned a lot while writing this thesis and want to thank him for his time and effort.

Next, I would like to thank Amelie for all her positive words and great support while working on my degree. Having someone like you is the best motivation for me.

A big thank you goes to my friends in Norway, Germany and all the other places for being there and making life better.

I would also like to thank all my teachers at UiT, RWTH Aachen and my fellow class mates there. This includes the guy who bought the coffee machine for NORUT brakka, you rock!

Last, but not least, a great thank you to my family who have been very supporting throughout my whole life, but especially during my final year.

Contents

1 Introduction

Radial transport of filamentary structures in the outer boundary region of magnetically confined plasmas has been of great research interest in the last years, [27, 18]. Experimental data reveals, that in different confinement modes of the plasma, radial transport is mediated by radially elongated structures that appear as blobs in the drift plane, [20] They carry excess particle density and head radially outwards from the fusion plasma, thus contributing significantly to particle and heat losses from the fusion plasma. They further contribute significantly to plasma recycling processes at the main chamber reactor shield. Blob transport will be a significant loss source in future Tokamak reactors, as ITER. Thus it is of great interest to characterize blob dynamics and develop a sound theoretical understanding of the dominant physical mechanisms behind blob motions.

Tokamaks A tokamak is a toroidal device designed to confine a fusion plasma. Typical parameters for this plasma is a temperature of 100-200eV in the core of the confined plasma, and electron densities of ca. $10^{20}/m^3$. These high temperature plasmas are confined by a strong magnetic field. Characteristic for a tokamak is its toroidal field geometry. Experiments with many geometries have shown that the tokamak has a favorable geometry for confining these plasmas. The general setup for a tokamak machine is depicted in fig.(1). The principal field responsible for plasma confinement is the poloidal field, created from the poloidal field cores around the plasma walls. A toroidal field alone will not confine a plasma. It creates pressure gradients that force the plasma out over. In addition, a poloidal field is needed. To create the poloidal field, one induces a current in the plasma along the poloidal magnetic field. Commonly a current coil in the center of the tokamak is used to induce this current. The magnetic field of this coil induces a current along the toroidal direction in the tokamak plasma. It is this current that creates a secondary toroidal field to confine the plasma in the tokamak.

The plasma particles are confined within these magnetic fields, but are still free to move out over. During the design of the tokamak principle, one thought that transport across the field lines is mainly due to Bohm diffusion, where particles gyro center jumps from field line to field line due to collisions. Thus, the cross field transport was thought to be low and negligible.

The magnetic field from the primary poloidal field coils is some 10T in modern reactors. For these strong fields one need superconducting magnets to avoid enormous ohmic heating losses, that makes the magnetic field coils the most expensive parts of the whole reactor.

One finds also several toroidal field coils around the tokamak. They provide a weaker magnetic field for positioning and shaping purposes.

Around the plasma one finds a blanket. Its purpose is to absorb the fast neutrons emitted from the fusion reaction and transforms them into heat, used for electricity production. Its other tasks may include the breeding of Tritium when one uses Tritium as a fuel. The shield is to protect equipment on the outside and especially the magnets from the neutron flux of the reactor.

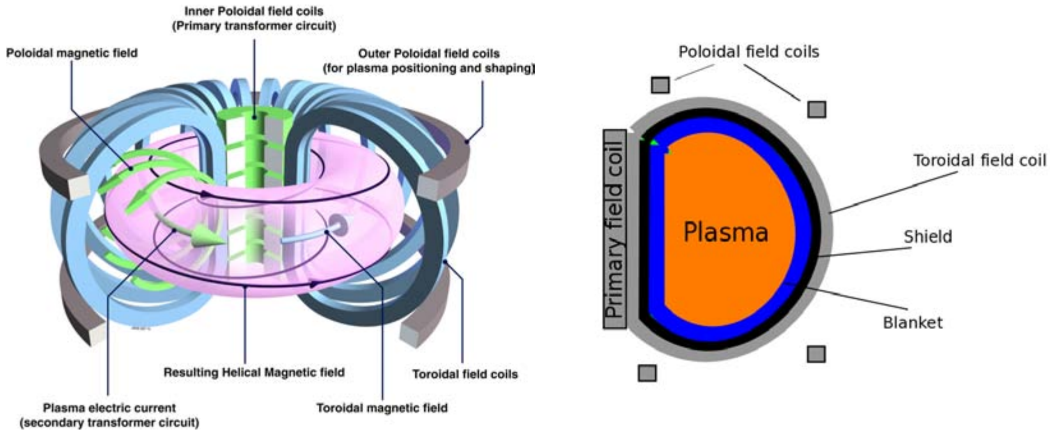

(a) The tokamak principle showing the mechanisms how the two major magnetic fields are created. Source: [1].

(b) Poloidal cross section

Figure 1: The tokamak confinement principle

Modern Tokamak reactors There are many tokamaks reactors installed where experimental work is conducted. Two prominent examples the ASDEX tokamak in Garchingen, Germany and the JET in Culham, England.

The ASDEX tokamak was built in the 1980s with an major upgrade installed in 1991. Its a minor radius $a = 0.5m$ and its major radis us $R_0 = 1.5m$ allow it to hold ca. $14m^3$ of a mixture of hydrogen, deuterium and helium plasma with temperatures between 5000 and 8600 eV. The plasmas total mass is some 3 mg and the electron density in the plasma is approx.. $10^{20}cm^{-3}$. In 1982 a new plasma confinement was discovered at the ASDEX tokamak by Wagner et al. [35]. This high confinement mode, or H mode, presents with longer confinement times at increased particle densities. It does this by forming a transport barrier at the outer plasma edge, which shows characteristic steep particle density gradients. The drawback of this confinement mode is, that it introduces a new type of MHD edge instability, edge localized modes or ELMs. This mode is characterized by a quasi-periodic relaxation of the particle density profile in the outer region of the Tokamak, thus rapidly ejecting large amount of particles and heat from the fusion plasma.

The JET tokamak in Culham is at the moment the largest operational one ever built. Its minor radius is $a = 1.25m$, its major radius is $R_0 = 3.0m$, and holding ca. $80 - 100m^3$ of plasma. The main toroidal magnetic field's strength is some $4T$ and the main plasma current ca. $7MA$. JET currently holds the record for highest ever measured peak fusion power. An experiment in 1997 recorded 16MW with an energy gain factor of $Q = 0.7$ [1].

Scrape off layer The outer regions of a magnetically confined plasma are also called for the scrape off layer, or SOL. It is designed to remove plasma entering this region from the confined plasma in a controlled fashion, before it comes in contact with the main chamber walls, plasma is scraped off.

The outer regions of a fusion plasma have different characteristic plasma parameters than the inner core. Densities typically fall from $10^{20}m^{-3}$ to $10^{16}m^{-3}$ over only some 10 cm in the outer regions. Accompanying are temperature drops from some 100 eV to some few eV, also a fall over several orders of magnitude. Here we also find both, open and closed magnetic field lines. Plasma confined in L and H mode have different characteristic pressures and temperatures in the scrape off layer, as presented in (Fill me out!). For a plasma in low confinement mode, or L-mode, the radial particle density gradients are broad, where as a plasma in the H-mode features large radial particle density gradients.

Due to the large temperature of the plasma no known material can withstand direct contact with it for any longer time period. When plasma particles come in contact with the wall, they can either be absorbed or be backscattered into the plasma. When they are absorbed, the particle, along with its kinetic energy diffuses into the wall, causing a net heat flux out of the reactor. In the wall, the plasma particle collides with the solid atoms, may scatter them into the plasma, or may diffuse itself back into the plasma. This process is known as plasma recycling.

Wall erosion causes impurities to collect in the plasma and the outwards heat flux are both inhibiting fusion reactions, they need to be minimized. In many reactors one finds a divertor for this. The idea of an divertor is as follows: The flux surfaces in the tokamak are closed, up to some point close to the walls. Open field lines in the wall region inside the reactor are designed not to go through the wall, but to a designated remote region, where plasma particles can collide with a special material surface, the divertor targets. The temperature at the divertor targets is usually some orders of magnitude less than at the core plasma, usually 10-0.1 eV. The length of a field line between two intersections is called the connection length. For Jet, the connection length varies between 30 and 150 m, [1].

The magnetic field lines in a tokamak are never aligned exactly along the toroidal direction, they are usually tilted by a small angle. This results in field lines, that spiral around the tokamak many times before they connect to themselves again. For a good confinement, these field lines do not intersect any material walls. Charged particles spiraling along field lines can follow them without any extra work, and are lost of they collide with walls. Since there is always some cross field transport for the particles, some will hit the wall eventually. To do this in a controlled fashion, some field lines are designed to intersect with the divertor targets. These field lines are called open field lines. In tokamak reactors, open and closed field lines are found in different regions, separated by the separatrix.

Fig. 1 shows these regions. Within the separatrix no field lines intersect the wall. The last closed flux surface is also depicted. The term flux surface comes from MHD stability theory, one can show that in MHD the magnetic field lines are along surfaces of constant pressure, which are called flux surfaces. Outside of the separatrix all field lines intersect the divertor.

1.1 Scrape off Layer instabilities

Turbulence in the SOL The fluctuating parameters of the boundary region in magnetically confined plasmas have been the subject of thorough investigation.

In an early review article, Wootton et al. characterized SOL turbulence by comparing plasma

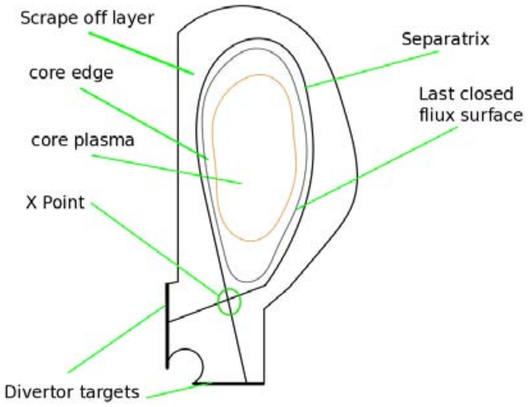

(a) Tokamak cross section showing the topology of the magnetic field lines. The separatrix separates open from closed field lines.

Figure 2: Scrape off layer in a tokamak

parameters from many experiments and show the broad range over which the parameters vary [38]. In other early work, Wagner et al. find that instabilities give a major contribution to radial ion and electron transport in different toroidal confinement devices, [36].
In this confinement mode, one observes intermittent radial transport which is associated to large scale turbulent structures, called blobs. This radial transport causes the loss of particles and heat from the fusion plasma.

A short description of ELMs Edge localized modes are an instability that occur in plasmas in H-mode. They are an explosive event, leading to ejection of large particle numbers and large amounts of energy. Experimental observations show a strong correlation between ELMs and plasma filaments travelling radially outwards from the outer mid-board region. They also show a significant extension along the magnetic field lines in the SOL region of a plasma, [25, 7]. A key feature of ELMs is that with rising turbulence amplitude, they deposite less energy in the divertor areas. In [29] Fig. 11 we see, that with increasing ELM density, the fraction of the ELM total energy that is deported into the divertor decreases with rising ELM energy. The fraction of the energy that is not lead to the divertor is transported into the main chamber wall.

Cross field transport by isolated filament structures Turbulent structures moving radially outwards towards the main chamber wall have been experimentally measured in any radial confinement machine. Experimental data from the TCV tokamak shows that edge plasma fluctuations show a universal statistical properties for a broad range of experimental data , [23, 17]. Conditional averaging of the measured particle density, show densities that present a steep front and heavy tails, features that are characteristic of radially elongated structures. An example of the diagnostics is shown in Fig. 3. We see, that the density time series presents a steep increase, followed by a long tail. This is a characteristic of radially elongated structures. Gas puffing images from different Tokamaks[34, 24], Fig. 4, where these turbulences are visualized, suggest the existence of localized density perturbations in the cross field domain that move radially outwards with large velocities. Structures observed for plasmas in high and low confinement mode share qualitative similarities as discussed in [24]. In [3], Antar et al. present that statistical properties of turbulent signals from turbulent transport in the SOL has universal. This suggests, that the mechanism behind the radial transport is common to confinement device they analyzed.

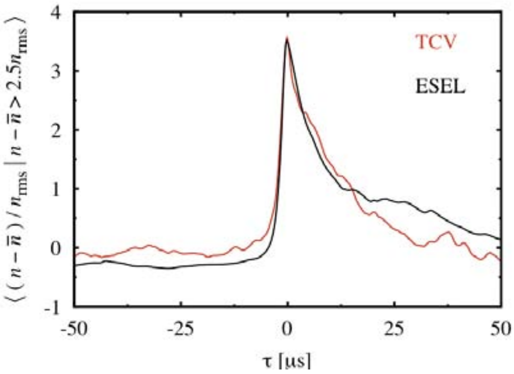

Figure 3: Conditionally averaged particle density time series, recorded from the TCV tokamak. It is compared to turbulence simulations on the SOL with the ESEL code. Reproduced from [18].

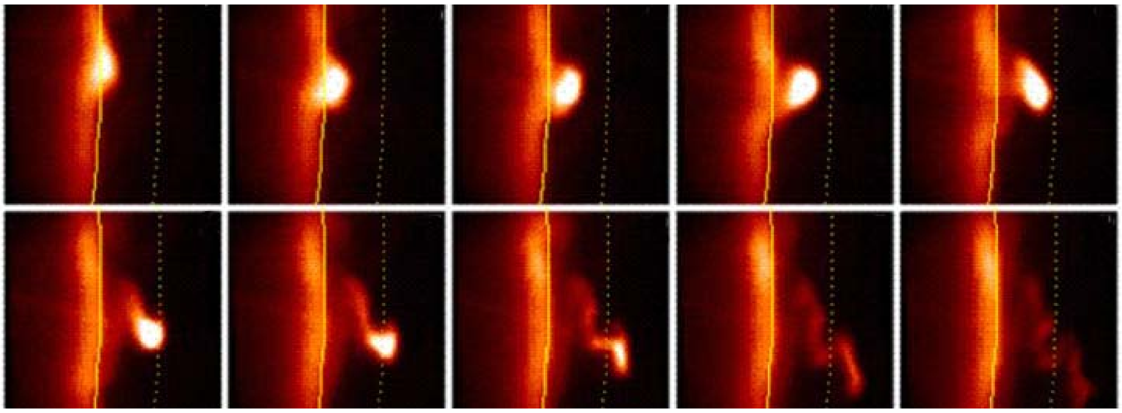

Figure 4: A Plasma blob transported radially outwards at the NSTX device. Time between each image is 8 μs. Image from Princeton Plasma Physics Laboratory

A solid mechanism for radial transport of coherent structures is given by the blob mechanism. It models the elongated plasma filaments as isolated blob-like structures in the drift plane. Their dynamics have been discussed thoroughly in literature, [26, 11, 6, 16, 15]. The results found from these studies, agree favorably with experiments. Results from numerical studies yield radial blob velocities, comparable to experimental findings, [15, 31]. Also measurements of the electrostatic potential from radially outwards moving filament structures, presented by [20], heavily suggest that the theory presented with the blob mechanism is the driving force behind radially propagating structures. Common blob models employ model closures, that include sheath parallel currents as a loss mechanism, as presented in [11, 15]. Experimental findings as discussed in [22] present strong correlations between sheath parallel currents and radial plasma transport caused by blobs.

1.2 Motivation

The radial blob velocity and its scaling are an important piece of information for estimating cross field energy and particle transport in toroidally confined plasmas. In this thesis we study a sheath connected blob model with variable amplitude. By means of numerical simulations, we quantify the effect both parameters have on radial blob dynamics. By comparing results from parameter studies to experimental results, we can assess the quality of the model and the range of parameters over which the theory is valid. It also presents the weak points of the theory and suggests further work.

2 Two field fluid equations

In this thesis we do numerical simulations of collective motions in a magnetized plasma. The model equations we simulate can readily be derived from the standard fluid description of a plasma. In the discussion below, we present the derivation of the model equation.
This section is structured as follows: Starting from the momentum equation of fluid theory, we present and discuss the various drift terms in the first subsection. We continue by calculating expressions for these drifts in toroidal geometry, where we assume local slab coordinates. With these expressions, we then present the resulting model equations in drift ordering. In the last subsection we discuss sheath dissipation, which is the dominant dissipation mechanism discussed in this thesis.

2.1 Physical setting

We are interested in simulating radial filament motion in the mid-outboard plane of toroidal confinement devies. A sketch of the setting is presented in Fig. 5(b). The toroidal confinement has a curvature vector $\underline{\kappa}$ pointing radially inward and a toroidal magnetic field pointing out of the paper plane. The strength of the toroidal magnetic field is assumed to decay with the radial coordinate R, thus ∇B points radially inward, in the same direction as the curvature vector of magnetic field $\underline{\kappa}$. In local slab coordinates, we identify the radial coordinate R with the cartesian coordinate x and the poloidal angle with the cartesian coordinate y. The simulation domain is denoted by the dashed square and is not to scale. Characteristic SOL filament lengths in the radial-poloidal domain are found to be $l \sim 1\text{cm}$.

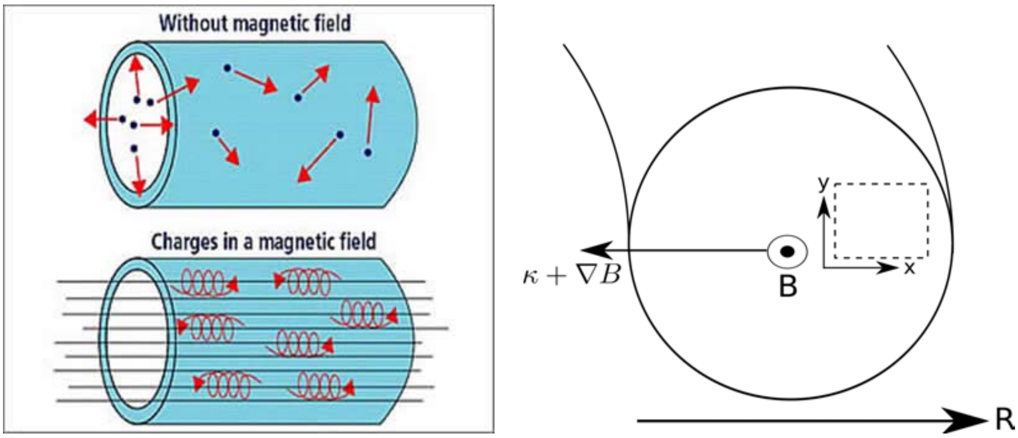

(a) Particles confined along a magnetic field. Source: www.jet.efda.org.

(b) Physical domain where the presented model equations are valid.

Figure 5: Principle of magnetic confinement and simulation domain.

We now continue with describing the plasma in the confinement device. A plasma is confined in a strong magnetic field, thus we call it magnetized. The particles feel no force when they move along magnetic field lines, and their gyration radius around them is small as presented in

Fig. 5(a). We consider a plasma consisting of electrons and one ion species. Fusion reactors are commonly fueled with a mixture of ^{1}H and ^{2}H, for simplicity we only consider singly charged ions with $m_i = 1\mathrm{u}$.

The dynamics of both particle species are described by their respective momentum equation

$$mn\left(\frac{\partial}{\partial t} + \underline{u}\cdot\nabla\right)\underline{u} = qn\left(\underline{E} + \underline{u}\times\underline{B}\right) - \nabla p - \nabla\underline{\underline{\pi}} + mn\nu_{\alpha,\beta}\left(\underline{u}_\alpha - \underline{u}_\beta\right). \tag{1}$$

We denote particle mass with m, particle density with n, velocity with $\underline{u}$, charge with q, the electric field with $\underline{E}$, the magnetic field with $\underline{B}$ with unit vector $\underline{b}$, the scalar pressure with p and the viscous stress tensor with $\underline{\underline{\pi}}$. The last term describes collisions between two different particle species which occur with a collision frequency $\nu_{\alpha,\beta}$, where the subscripts α and β denote particle species. We use $\alpha = e, i$ do denote electrons and ions. In general we omit particle species indices, and include them at the first position when we discern between particle species. The subscripts $\|$ and $\perp$ on vector quantities denote the components parallel and perpendicular to the magnetic field respectively. For example, $\underline{u}_\| = \underline{b}\cdot(\underline{u}\cdot\underline{b})$ and $\underline{u}_\perp = \underline{b}\times(\underline{u}\times\underline{b})$.

Strongly magnetizes plasmas have a high gyration frequency $\omega_c = qB/m$, they complete several larmor gyrations before they collide with another particle:

$$\nu \ll \omega_c. \tag{2}$$

We use this in the following approximation of the viscous stress tensor:

$$\nabla\underline{\underline{\pi}} \sim \eta_\perp\nabla_\perp^2\underline{u} + \eta_\|\nabla_\|^2\underline{u}.$$

This term describes momentum transfer of the velocity due to changes in velocity along different directions. The expression itself has a complex structure, as it is a tensor quantity. Its single elements can be ordered in terms proportional to either $1/\nu$, ν/ω or proportional to $1/\omega$. When calculating the full expression, we find that $\nabla_\perp\underline{\underline{\pi}} \propto \eta_\perp$, where the diffusion coefficient perpendicular to the magnetic field is the largest, $\mathcal{O}(\eta_\perp) = \nu/\omega_c$. A derivation of this tensor is shown in [8, 21].

2.2 Computation of the drift terms in toroidal geometry

We continue by identifying the important drifts in the fluid equation and computing suitable expressions for them. Crossing Eqn. (1) with the magnetic field vector, $\underline{B}$, we find for the velocity perpendicular to the magnetic field:

$$\begin{aligned}
\underline{B} \times \left(mn\frac{d}{dt}\underline{u}\right) &= +\underline{B} \times [qn(\underline{E} + \underline{u} \times \underline{B})] + \underline{B} \times (-\nabla p) + \underline{B} \times \left(-\nabla \underline{\underline{\pi}}\right) + \underline{B} \times mn\nu_{\alpha,\beta}\left(\underline{u}_\alpha - \underline{u}_\beta\right) \\
\Leftrightarrow \underline{B} \times \frac{d}{dt}\underline{u}_\perp &= -\frac{q}{m}\left(\underline{B} \times \nabla\phi\right) - \frac{T}{mn}\left(\underline{B} \times \nabla\underline{n}\right) + \frac{qB^2}{m}\underline{u}_\perp - \underline{B} \times \left(\nabla\underline{\underline{\pi}}\right) + \nu_{\alpha,\beta}\underline{B} \times \left(\underline{u}_\alpha - \underline{u}_\beta\right) \\
\Leftrightarrow \underline{u}_\perp &= \frac{(\underline{b} \times \nabla\phi)}{B} + \frac{T\left(\underline{b} \times \nabla n\right)}{qnB} + \frac{\underline{b} \times \left(\nabla\underline{\underline{\pi}}\right)}{\omega_c} + \frac{mn\nu_{\alpha,\beta}}{\omega_c}\underline{b} \times \left(\underline{u}_\alpha - \underline{u}_\beta\right) + \frac{1}{\omega_c}\left(\underline{b} \times \frac{d}{dt}\underline{u}\right).
\end{aligned} \tag{3}$$

Here we introduced the electrostatic potential ϕ via $E = -\nabla\phi$, which gives $\nabla \times E = 0$. Further we divided the fluid velocity in components parallel and perpendicular to the magnetic field. Eqn. (3) describes plasma dynamics perpendicular to the magnetic field and assumed an isothermal plasma.

Motions perpendicular to the magnetic field are constituted of

1. $\frac{1}{B}\left(\underline{b} \times \nabla\phi\right)$: The $E \times B$ drift or electric drift, caused by the electric field disturbing the particle gyrating motion. This is a drift of the plasma particles guiding center and independent of particle charge.
2. $\frac{T}{qnB}\left(\underline{b} \times \nabla n\right)$: This term describes the diamagnetic drift, a macroscopic flow due to an uneven spatial distribution of gyrating particles. Note that this flow is not caused by guiding center motion.
3. $\nabla\underline{\underline{\pi}}$: Viscous drift due to viscous stress on the plasma.
4. $\frac{mn\nu_{\alpha,\beta}}{\omega_c}\underline{b} \times \left(\underline{u}_\alpha - \underline{u}_\beta\right)$: Resistive drift caues by momentum transfer between particle species.
5. $\frac{1}{\omega_c}\left(\underline{b} \times \frac{d}{dt}\underline{u}\right)$: This term has order of magnitude $\mathcal{O}(\omega/{\omega_c}^2)$, where ω denotes the characteristic scale of perpendicular dynamics. This term is computed by inserting the solution u to order $\mathcal{O}(\omega/\omega_c)$.

The parallel part of the particle velocity is treated separately for both particle species. We assume that the ions have no velocity along the magnetic field, $u_{i,\|} = 0$. If we assume that the electrons are Boltzmann distributed,

$$n = n_0 \exp\left(-\frac{q\phi}{T}\right), \tag{4}$$

it follows, that the parallel motions of the electrons is zero, $u_{e,\|} = 0$.

If we assume a force balance for the electrons, $m_e n_e d/dt\underline{u}_{e,\|} = 0$, and neglect the viscous and resistive drift, we find:

$$\underline{u}_{e,\|} = \frac{e\nabla_\|\phi - T\nabla_\| \ln n}{m_e\nu_{ei}}. \tag{5}$$

For a magnetized plasma we can assume that the larmor gyration is the dominant motion perpendicular to the magnetic field. Any change in a particles perpendicular velocity happens over a larger time scale than gyration happens. Therefore, we neglect the time derivative, the viscous and resistive drift in Eqn. (3) to obtain a solution of order $\mathcal{O}(\omega/\omega_c^3)$ for $\underline{u}_\perp$:

$$\underline{u}_\perp = \underline{u}_E + \underline{u}_d + \underline{u}_\pi + \underline{u}_r + \mathcal{O}\left(\frac{\omega}{\omega_c^3}\right) \tag{6}$$

where ω is the characteristic frequency of perpendicular dynamics, corresponding to the time derivative in Eqn. (3).

The drift $\underline{u}_\pi$ caused by the divergence of the viscous stress tensor is not of lowest order because the tensor itself is $\mathcal{O}\left(\nu/\omega_c\right)$. The viscous stress tensor is also proportional to the particle mass, resulting in larger viscosity effects on the ions than on the electrons. We neglect it for the electron momentum equation and include it in the ion momentum equation.

Inserting these first order drifts only for u in the time derivative term in Eqn. (3), we find the polarization drift:

$$\underline{u}_p = \frac{m}{qB}\underline{b} \times \left(\frac{\partial}{\partial t} + \underline{u}_E \cdot \nabla + \underline{u}_d \cdot \nabla + \underline{u}_\parallel \cdot \nabla\right)\left(\underline{u}_E + \underline{u}_d + \underline{u}_\parallel\right) \tag{7}$$

Now we make further assumptions and begin to distinguish between electrons and ions. For the electrons, we use the fact that they are much lighter than the ions. The lightest positively charged ion, a proton has a mass m_p which is approximately 1836 times the mass of an electron, m_e. In the equation for the electron dynamics we therefore neglect the polarization drift term. We also assume cold ions, $T_i = 0$, and neglect the diamagnetic drift term in the ion equation.

The ion momentum equation reads now:

$$\underline{u}_i = \frac{1}{B}\left(\underline{b} \times \nabla\phi\right) - \frac{m}{qB^2}\left(\frac{\partial}{\partial t} + \underline{u}_E \cdot \nabla\right)\nabla_\perp\phi + \underline{u}_\pi \tag{8}$$

where we have rewritten the polarization drift for the ions as:

$$\begin{aligned}\underline{u}_{i,p} &= \frac{m}{qB}\underline{b} \times \left(\frac{\partial}{\partial t} + \underline{u}_E \cdot \nabla\right)\underline{u}_E \\ &= -\frac{m}{qB^2}\left(\frac{\partial}{\partial t} + \left(\underline{b} \times \nabla\phi\right) \cdot \nabla\right)\nabla_\perp\phi \end{aligned} \tag{9}$$

Here we used that the cross product commutes with both differential operators for a magnetic field that is constant in time and space. This is not trivial, as the convective derivative $\underline{u}_E \cdot \nabla$ is different in direction and magnitude in every point in physical space.

We also expresse the polarization drift, which is a vector quantity, through one scalar variable, the electric potential ϕ.

In the electron momentum equation we neglect the polarization drift because it is proportional to the electron mass and is thus a mechanism that transfers only little momentum:

$$\underline{u}_e = \frac{1}{B}\underline{b} \times \nabla\phi - \frac{T}{qnB}\underline{b} \times \nabla n. \tag{10}$$

When we ignore atomic reactions that create charged particles, the charge continuity equations holds:

$$\frac{\partial \rho}{\partial t} + \nabla \underline{j} = 0 \tag{11}$$

where ρ is a charge density:

$$\rho = \sum_\alpha q_\alpha \frac{\partial n_\alpha}{\partial t}.$$

An electrical current is then given by $\underline{j}_\alpha = n_\alpha \underline{u}_\alpha$. The index α is used to label particle species, in our case electrons and ions $\alpha = e, i$. Writing the continuity for $\alpha = e, i$, we get:

$$\frac{\partial n_e}{\partial t} + \nabla\left(n_e\underline{u}_E + n_e\underline{u}_{e,d} + n_e\underline{u}_{e,\|}\right) = 0 \tag{12}$$

$$\frac{\partial n_i}{\partial t} + \nabla\left(n_i\underline{u}_E + n_i\underline{u}_{i,p} + n_i\underline{u}_{i,\pi}\right) = 0. \tag{13}$$

The viscous drift $\underline{u}_\pi$ comes from the divergence of the viscous stress tensor in Eqn. (2.1), where first order solutions for $\underline{u}$ are assumed. Next we invoke quasi neutrality, as each physical system strifes towards its lowest energy state, a plasma moves against charge separation. We find approximately as many ions as electrons in a plasma volume element: $n_e \approx n_i$. Therefore the first term in Eqn. (11) vanishes.

With the vanishing diamagnetic drift for ions and vanishing polarization drift for electrons we now have:

$$\nabla \cdot \left(n\underline{u}_{e,d} + n\underline{u}_{e,\|} - n\underline{u}_{i,p} - n\underline{u}_{i,\pi}\right) = 0 \tag{14}$$

where we subtracted the continuity equations for each particle species.

The plasmas we are considering, are quasi neutral, therefore the equation above expresses that the electric current in the plasma is divergence free,

$$\nabla \underline{j} = \nabla\left(\underline{j}_\perp + \underline{j}_\|\right) = 0 \tag{15}$$

holds. We do not have a fixed expression for the parallel part of the particle motions. For the derivation of the model equations we will close Eqn. (15) with $\nabla \underline{j}_\| = 0$. That is, we

construct the model equations from the condition $\nabla_\perp \underline{j} = 0$ Later on we will consider other closures for the parallel current of the system.
Let us note, that for a uniform magnetic field, the difference between Eqn. (12) is given by:

$$\frac{d}{dt}\left(en_i - en_e\right) + \left(\frac{m_i n_i + m_e n_e}{\epsilon_0 B^2}\right)\frac{d\rho}{dt} = 0 \tag{16}$$

$$\left(1 + \frac{\rho_m}{\epsilon_0 B^2}\right)\frac{d\rho}{dt} = 0, \tag{17}$$

where we ignored diamagnetic currents, used the Laplace equation $\nabla^2\phi = \epsilon_0\rho$ and defined the mass density $\rho_m = m_i n_i + m_e n_e$. Inserting common values for a plasma yield, give $\rho_m/\epsilon_0 B^2 \approx 100$. Thus, quasi neutrality yields, that $E \times B$ advection is smaller than polarization currents.

We continue with Eqn. (12) and Eqn. (14) by deriving explicit expressions for each single term. Our goal is to obtain two independent time evolution equations from them that describe a plasma.

Let us look at Eqn. (12) first. Recall that we neglected the collision term in Eqn. (1). We now invoke it for the electron density equation only. Collisions between electrons and ions result in a random deflection of the electron velocity vector while the heavy ions remain almost unaffected. This results in a net drift acting on the electrons, the resistive drift. It is given by:

$$\underline{u}_r = m_e n \nu_{e,i}\left(\underline{u}_e - \underline{u}_i\right) \tag{18}$$

$$= m_e \nu_{e,i} \underline{b} \times \underline{u}_{e,d}, \tag{19}$$

where $\nu_{e,i}$ is the collision frequency between electrons and ions and where $\underline{u}_e$ and $\underline{u}_i$ are approximated with first order drifts and the ion diamagnetic drift is ignored as before. This allows us to readily derive an expression for the divergence of this drift:

$$\nabla\left(n\underline{u}_r\right) = \nabla\left(mn^2\nu_{e,i}\underline{b} \times \frac{T}{qnB}\underline{b} \times \nabla n\right)$$

$$\simeq \frac{m\nu_{e,i}T}{qB}\nabla_\perp^2 n.$$

We have neglected $(\nabla n)^2$ as a small quantity for this expression. We see that the resistive drift divergence acts as a diffusion in real space for the particle density. Its coefficient is of order $\mathcal{O}(\nu_{e,i}/\omega_c)$, low values mean high collisionality.
We continue by rewriting Eqn. (12) as :

$$
\begin{aligned}
\frac{\partial n}{\partial t} + \nabla \cdot \left(n\underline{u}_E + n\underline{u}_{e,d} + n\underline{u}_{e,\parallel} \right) &= \left(\frac{\partial}{\partial t} + \underline{u}_E \cdot \nabla \right) n + \nabla \cdot \left(n\underline{u}_{e,d} \right) + \nabla \cdot \left(n\underline{u}_{e,\parallel} \right) \\
&= \left(\frac{\partial}{\partial t} + \frac{1}{B}\underline{b} \times \nabla\phi \cdot \nabla \right) n + \nabla \cdot \left(n\underline{u}_{e,d} \right) \nabla \cdot \left(n\underline{u}_{e,\parallel} \right). \\
&= 0
\end{aligned}
$$

We see that the divergence of the diamagnetic drift occurs, let us derive an expression for this term that suits our purposes. We start out with the last term from Eqn. (10):

$$
\begin{aligned}
\nabla(n\underline{u}_{e,d}) &= \nabla\left(\frac{T}{eB}\underline{b} \times \nabla n \right) \\
&= \frac{2T}{eB}\underline{b} \times \nabla \ln B \cdot \nabla n,
\end{aligned}
\tag{20}
$$

where we used that $\underline{b} \times \kappa = \underline{b} \times \nabla \ln B$:

$$
\begin{aligned}
\nabla \times \underline{B} = \nabla \times B\underline{b} &= B\left(\nabla \times \underline{b}\right) + \left(\nabla B\right)\underline{b} = 0 \\
\Leftrightarrow \nabla \times \underline{b} &= (-\nabla B \times \underline{b})/B = \underline{b} \times \left(\nabla B/B\right) = \underline{b} \times \nabla \ln B \\
\text{with} \quad \nabla \times \kappa &= \underline{b} \times \kappa.
\end{aligned}
$$

When we continue by assuming that the magnetic field is a toroidal one, i.e. $\underline{B} = -\frac{B_0 R_0}{R}\hat{\underline{\theta}}$, we can rewrite $\nabla \ln \underline{B}$ as:

$$
\nabla \ln \underline{B} = \frac{\nabla \underline{B}}{B} = \frac{1}{B}\frac{\partial}{\partial R}\left(\frac{B_0 R_0}{R} \right)\hat{\underline{R}} = -\frac{1}{R}\hat{\underline{R}}.
$$

In this geometry we also have $\hat{\underline{R}} \times \hat{\underline{\theta}} = \hat{\underline{z}}$. Inserting this expression in Eqn. (20), we get for the divergence of the diamagnetic electron drift in a homogeneous toroidal magnetic field with the magnetic field along the $\hat{\underline{\theta}}$-axis:

$$
\nabla\left(n\underline{u}_{d,e} \right) = \frac{2T}{eBR}\frac{\partial n}{\partial z}. \tag{21}
$$

For Eqn. (14) we need the divergence of the ion polarization drift, Eqn. (9)

$$
\begin{aligned}
\nabla \cdot (n\underline{u}_{i,p}) &= \nabla\left(-\frac{mn}{qB^2}\left(\frac{\partial}{\partial t} + \underline{u}_E \right)\nabla_\perp \phi \right) \\
&= \frac{mn}{qB^2}\left(\nabla \ln n + \nabla \right)\left(\frac{\partial}{\partial t} + \frac{1}{B}\underline{b} \times \nabla_\perp \phi \cdot \nabla \right)\nabla_\perp \phi.
\end{aligned}
\tag{22}
$$

The divergence operator at the beginning acts both on the particle density n and on ϕ, whereas it commutes with the total time derivative in the parenthesis.
We also compute an expression for the viscous drift:

$$\begin{aligned} \nabla \cdot (n\underline{u}_\pi) &= \nabla \cdot (n\eta_\perp \underline{b} \times \underline{u}_E) \\ &= \frac{n}{B}\eta_\perp \nabla_\perp^4 \phi. \end{aligned} \tag{23}$$

For this drift, we neglect density gradients and approximate it with $\underline{u}_\pi \approx \eta_\perp \nabla_\perp^4 \phi$.
In the same manner we compute the divergence of the $E \times B$ drift:

$$\begin{aligned} \nabla \cdot \underline{u}_E &= \nabla \cdot \left(\frac{1}{B} \times \nabla\phi\right) \\ &= \frac{1}{B}\underline{b} \times \nabla \ln B \cdot \nabla\phi + \frac{1}{B}\nabla \times \underline{b} \cdot \nabla\phi, \end{aligned}$$

the first term is caused by the divergence of the current, the second term arises from field curvature. We again assume a toroidal field along the $\hat{\theta}$ axis: $\underline{B} = -B_0R_0/R\hat{\underline{\theta}}$ and find:

$$\nabla \underline{u}_E = -\frac{2}{B_0R_0}\frac{\partial\phi}{\partial z} \tag{24}$$

Let us now introduce a new physical quantity, the vorticity Ω, which is defined as $\Omega = \nabla \times \underline{u}$. In fluid dynamics one often reformulates the equation of motion in terms of the vorticity, by taking the curl of the velocity equations. If we consider only the $E \times B$ drift velocity, we can show that $\Omega = \frac{1}{B}\underline{b}\nabla^2\phi$ holds:

$$\begin{aligned} \nabla \times \underline{u}_E &= \nabla \times \left(\frac{1}{B}\underline{b} \times \nabla\phi\right) \\ &= \frac{1}{B}\left(\nabla \cdot \nabla\phi\right) - \nabla\phi\left(\nabla \cdot \frac{1}{B}\underline{b}\right) + \left(\nabla\phi \cdot \nabla\right)\frac{1}{B}\underline{b} - \left(\frac{1}{B}\underline{b} \cdot \nabla\right)\phi \\ &= \frac{1}{B}\nabla^2\phi + \mathcal{O}\left(\frac{l}{L}\right), \end{aligned}$$

because $\mathcal{O}(B) = L$, and $\mathcal{O}(\phi) = l$, where $\frac{l}{L} \ll 1$. This is, because we previously assumed a homogeneous magnetic field, thus the characteristic scales on which B varies are much larger than the scales on which the electrostatic potential varies. We use that the gradients of the fields are of the same magnitude as the fields them self: $\mathcal{O}(\nabla B) = L$, $\mathcal{O}(\nabla\phi) = l$.

2.3 Two field equations in drift ordering

When we insert the Eqn. (21) and Eqn. (22) into Eqn. (12) and Eqn. (14) and we obtain:

$$\left(\frac{\partial}{\partial t} + \underline{u}_E \cdot \nabla\right) n + \frac{2}{B_0 R_0}\frac{\partial \phi}{\partial z} + \frac{2T}{eBR}\frac{\partial n}{\partial z} = \frac{T_e}{m_e \nu_{ei}} \nabla_{\parallel}^2 \left(\frac{e\phi}{T} - \ln n\right) + \frac{m \nu_{e,i} T}{qB} \nabla_{\perp}^2 n \tag{25}$$

$$\frac{mn}{qB^2}\left(\nabla \ln n + \nabla\right)\left(\frac{\partial}{\partial t} + \underline{u}_E \cdot \nabla\right) \nabla_{\perp}\phi + \frac{2T}{eBR}\frac{\partial n}{\partial z} = \frac{T_e}{m_e \nu_{ei}} \nabla_{\parallel}^2 \left(\frac{e\phi}{T} - \ln n\right) + \eta_{\perp} \nabla_{\perp}^4 \phi. \tag{26}$$

This is a two field model for strongly magnetized, low β plasmas. They are two coupled non-linear partial differential equations for evolution of the physical fields of density n and electrostatic potential ϕ. Note that Eqn. (14) is the evolution of the ion density in the case that $n_i \simeq n_e$, we obtained it by taking a linear combination of the particle continuity equations for each particle species. In the further discussion, we assume the length on which the density varies is small compared to the length scales of the electrostatic potential. This allows us to approximate

$$\nabla \ln n \approx 0.$$

we thus ignore this term in Eqn. (26). To relate the potential and the density back to the single species densities, we have to close our model with an equation relating these parameters back to each other. This does the Poisson equation,

$$\epsilon \nabla^2 \phi = e n_e - e n_i.$$

The $E \times B$ drift advection terms $\underline{u}_E \cdot \nabla n$ and $\underline{u}_E \times \nabla_{\perp}^2 \phi$ are non-linear and introduce a coupling between all length scales of the system. To see this, we write the fields n and ϕ as their Fourier series, $n = \sum_{\underline{k}} n_{\underline{k}} \exp i(\underline{k}\underline{x} - \omega t)$ and $\phi = \sum_{\underline{k}} \phi_{\underline{k}} \exp i(\underline{k}\underline{x} - \omega t)$. Inserted into the term $\underline{u}_E \cdot \nabla n$, this yields:

$$\begin{aligned}
\underline{u}_E \cdot \nabla n &= \frac{1}{B} \underline{b} \times \nabla \phi \cdot \nabla n \\
&= \frac{1}{B}\left(\partial_y \phi \partial_x n - \partial_x \phi \partial_y n\right) \\
&= \frac{1}{B}\left(\partial_y \sum_{\underline{k}} \phi_{\underline{k}} e^{i(\underline{k}\underline{x} - \omega t)} \partial_x \sum_{\underline{k}'} n_{\underline{k}'} e^{i(\underline{k}'\underline{x} - \omega t)} - \partial_x \sum_{\underline{k}} \phi_{\underline{k}} e^{i(\underline{k}\underline{x} - \omega t)} \partial_y \sum_{\underline{k}'} n_{\underline{k}'} e^{i(\underline{k}'\underline{x} - \omega t)}\right) \\
&= \frac{1}{B}\left(-\sum_{\underline{k},\underline{k}'} \phi_{\underline{k}} n_{\underline{k}'} k_y k'_x e^{i((\underline{k}+\underline{k}')\underline{x} - \omega t)} + \sum_{\underline{k},\underline{k}'} \phi_{\underline{k}} n_{\underline{k}'} k_x k'_y e^{i((\underline{k}+\underline{k}')\underline{x} - \omega t)}\right)
\end{aligned}$$

This shows explicitly that all length scales of n and ϕ couple via the products of k and k'. A numerical computation of this term has to conserve energy to give accurate results.

2.4 Dissipation mechanisms

The model equations derived above include cross field viscosity and molecular diffusion as the major dissipation mechanisms. Both of these are intrinsic to the plasma. Confining a plasma magnetically within a toroidal confinement device, causes other dissipation mechanisms arise. In this thesis we study the effect of sheath dissipation. These are electric current channels along open magnetic field lines that intersect the divertor targets.

Open field lines are localized in the SOL of tokamak reactors. The general approach to incorporate such dissipation mechanisms in two field models is to describe the $\nabla J_\|$ term as an differential operator acting on ϕ:

$$\nabla_\| J_\| \rightarrow \sigma\phi + \nu\nabla_\perp^2\phi + \mu\nabla_\perp^4\phi. \tag{27}$$

Sheath dissipation and other dissipation mechanisms that are described by an operator of this form are presented in [27]. We continue our discussion, by modeling the effects of sheath parallel currents on the electrostatic potential. The discussion follows the introduction of [28, ch. 6].

2.4.1 Sheath dissipation

The presence of divertor targets has strong influence on the ion and electron density and velocity and on the electrostatic potential in their immediate surroundings. Secondary effects at material walls include plasma recycling and recombination among others. We ignore these effects and describe the effects of a biased surfaces in a hot plasma has on the electrostatic potential.

A sketch of the situation is presented in Fig. 6. Assume that at $x = 0$ is a boundary surface to the plasma with zero potential. The sheath surface is at negative potential $\phi_{\mathrm{sh}} = -1$, the

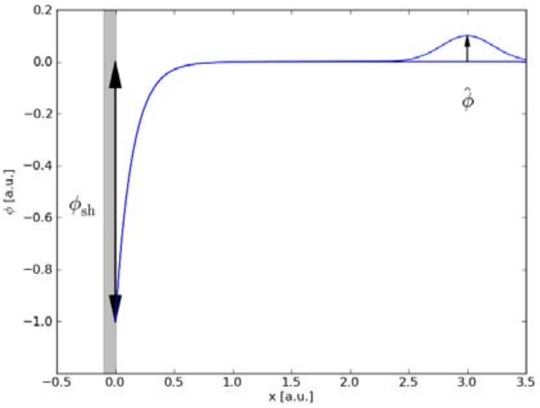

Figure 6: Electrostatic potential in the half space $0 < x$ bounded by a material surface. The sheath region is characterized by a sharp decay of ϕ.

plasma potential ϕ_{plasma} is at zero potential and perturbations to the plasma potential are denoted with $\hat{\phi}$. Consistently with our assumptions for the two field model described above, we assume cold ions ($T_i = 0$) and Maxwellian distributed electrons and neglect collisions. Debye shielding in the plasma effectively shields the potential over the length of some Debye lengths λ_D. For electrostatic potential $\phi(x)$ from the figure, this gives $\lim_{x\to 0}\phi(x) = -1$ and $\lim_{x\gg\lambda_D} = 0$. The electrons are assumed to be Boltzmann distributed. Further do they have to overcome a repulsive potential to enter the sheath region, thus we find that only electrons with a kinetic energy larger than the repulsive potential enter the sheath region:

$$n_e = n_{e,0} \times \exp\left(e(\tilde{\phi})/T\right).$$

Here $n_{e,0}$ is the electron density at the entry point to the sheath region and ϕ is the electrostatic potential within the sheath region. Since $\phi < 0$, we see that the electron density is decreasing. One can calculate, that the net flux of electrons toward the surface is given by $J_{e,\|} = nC_s\sqrt{m_i/m_e 2\pi}\exp\left(e\tilde{\phi}/T\right)$, where we defined the ion acoustic speed, $C_s = \sqrt{T_e/m_i}$. Integrating the electron velocity distribution function over real space shows, that the electron density decreases towards the sheath.

A similar behavior of the ion particle density is observed, although for a different reason. The ion velocity u_i increases towards the negatively biased surface. Flux conservation reads $n_{i,0}u_{i,0} = n_i(x)u_i(x)$, where $n_{i,0}$ and $u_{i,0}$ are the ion density and velocity at the sheath entry region. This gives, that for increasing $u_i(x)$, $n_i(x)$ must be decreasing. An energy conservation argument can now be used, to show, that the Poisson equation is only fulfilled in the sheath region, when $u_i(x) \geq C_s^2$.

This gives a net current of

$$J_\| = n_0 e C_s \left(1 - \sqrt{\frac{1}{2\pi}}\sqrt{\frac{m_i}{m_e}}\exp\left(\frac{e\phi}{T}\right)\right).$$

In a situation where no net currents flow to the surface, we can compute, that the potential ϕ is given with $\phi = kT/2e\ln(m_i/m_e 2\pi)$. This potential is called the floating potential, we denote it with ϕ_{fl} and is experimentally accessible. With this, we write the parallel electric currents at the divertor targets as:

$$J_\| = -enC_s\left(1 - \exp\left(-\frac{e\phi}{T}\right)\right). \tag{28}$$

In this expression, ϕ is the difference between the plasma potential and the floating potential of the divertor targets. We also see, that it is the heavy particle species, that give the characteristic velocity of this phenomena in a similar matter as ambipolar diffusion for example.

2.5 Model equations from the two field equations

In this section we rewrite the two field equations in MHD ordering which allows significant simplification. We argue why we can neglect some terms and present a simplified, dimensionless equation set. Two model equation set are derived from these equations. One model set is linearized for small particle density perturbations and has a reduced free parameter set. The second model allos for arbitrary particle density perturbations and includes an extra model parameter.

2.6 Two field equations in MHD ordering

When we derived the two field equations, we assumed drift ordering, we find that both the $E \times B$ drift and the diamagnetic drift are lowest order solutions for $u_\perp$. What we wish to do now, is to reduce these equations to models, for which MHD ordering is sufficient. Let us compare the magnitude of the different drifts in both orderings:

$$\begin{aligned}\text{Drift ordering}: &\quad \underline{u}_E \approx \underline{u}_d \approx \underline{u}_t \delta \\ \text{MHD ordering}: &\quad \underline{u}_E \approx \underline{u}_t \approx \underline{u}_d/\delta,\end{aligned}$$

here $\underline{u}_t = \sqrt{T/m}$ denotes thermal velocity. We see that the diamagnetic drift is one order smaller than the major drifts in MHD ordering than they are in drift ordering. The crucial difference between MHD and drift ordering is, that in MHD, the $E \times B$ drift is the only drift of lowest order, it is of the same order as the acoustic velocity: $\underline{u}_E \approx c_s \approx \sqrt{T_e/m_i}$. We therefore neglect the $n\nabla\underline{u}_d$ term in the Eqn. (26)).

Since we are interested in the interchange mechanism for blob transport, we can make another simplification. We saw earlier that blob transport is driven by the ∇B and curvature drifts. These drifts are the expressed by diamagnetic current in MHD which is of lowest order. For a MHD equilibrium we have $\underline{J} \times \underline{B} = \nabla P$, which yields $\underline{J}_\perp = 1/B^2 \underline{B} \times \nabla P$ as the lowest cross term current. Assuming isothermal electrons, this is the diamagnetic current for the electrons.

From the MHD momentum equation we obtain the Ohm's law:

$$\underline{E} + \underline{V} \times \underline{B} - \frac{1}{n_e e}\left(\underline{V} \times \underline{B} - T\nabla n_e\right) = \eta \underline{J}. \tag{29}$$

The last term on the right hand side is called the hall term. We say we are using resistive MHD when we can that term. Resistive MHD is different from ideal MHD, because it features the diamagnetic drift as a lowest order drift. This is incompatible with the MHD velocity ordering, where the $E \times B$ drift is of lowest order. This is what we find when we compare the order of the $E \times B$ and the diamagnetic current term:

$$\frac{\frac{T\nabla n}{ne}}{\underline{J} \times \underline{B}} \sim \frac{T}{veBl} = \frac{r_L}{v}\frac{T}{vlm} \sim \mathcal{O}(\delta). \tag{30}$$

We can thus neglect the diamagnetic term with the density gradient in Eqn. (29). This gives the resistive Ohm"s law, from which we readily compute the divergence of the parallel currents:

$$\begin{aligned} \underline{E} + \underline{J} \times \underline{B} &= \eta \underline{J} \\ \Rightarrow \nabla \cdot \underline{J}_{\|} &= -\frac{1}{\eta} \nabla_{\|}^2 \phi. \end{aligned} \tag{31}$$

This result shows that in MHD ordering the divergence of the parallel current is given by an operator acting on the electrostatic potential only. Comparing this to Eqn. (25) and Eqn. (26), we neglect the $\nabla_{\|}^2 \ln n$ terms when we rewrite the model in MHD ordering.

It turns out, that the compression of the $E \times B$ drift and the diamagnetic drift in the density equation can be neglected and one still retains the relevant physics from this model. Thus we neglect the $\partial \phi / \partial z$ term in Eqn. (26) and the $\partial n / \partial z$ term in Eqn. (25). This gives two simplified model equations:

$$\begin{aligned} \left(\frac{\partial}{\partial t} + \underline{u}_E \cdot \nabla \right) n &= \frac{T_e}{m_e \nu_{ei}} \nabla_{\|}^2 \left(\frac{e\phi}{T} \right) + \frac{m \nu_{e,i} T}{qB} \nabla_{\perp}^2 n \\ \left(\frac{\partial}{\partial t} + \underline{u}_E \cdot \nabla \right) \nabla_{\perp}^2 \phi + \frac{2T}{mnR} \frac{\partial n}{\partial z} &= \frac{T_e}{m_e \nu_{ei}} \nabla_{\|}^2 \left(\frac{e\phi}{T} \right) + \eta_{\perp} \nabla_{\perp}^4 \phi. \end{aligned}$$

Earlier we assumed, that the electrons are isothermal and the ions are cold. A derivation of the equations above can be done without the assumption that $T_e = \text{const}$. One finds the same equation set for a general thermodynamic variable θ, which can represent both, temperature and particle density. In our discussion, we let θ denote particle density. We write the parallel current as $J_{\|}$ to denote, that we have not made a special assumption on the character of parallel currents. The model equations read now:

$$\left(\frac{\partial}{\partial t} + \frac{1}{B} \underline{z} \times \nabla \phi \cdot \nabla \right) n = \chi \nabla_{\perp}^2 n + \nabla_{\|} J_{\|} \tag{32}$$

$$\left(\frac{\partial}{\partial t} + \frac{1}{B} \underline{z} \times \nabla \phi \cdot \nabla \right) \Omega + \frac{2T}{mnR} \frac{\partial n}{\partial y} + = \eta \nabla_{\perp}^2 \Omega + \nabla_{\|} J_{\|} \tag{33}$$

The model above incorporates all important mechanisms to study interchange motions in strongly magnetized plasma. It features the interchange instability since we included a divergence of the diamagnetic drift in the vorticity equation. Both equations feature also the non-linear divergence of the $E \times B$ drift. The dissipation coefficients η is the kinematic viscosity of the fluid. The other dissipation coefficient χ is the collisional diffusivity.

2.6.1 Dimensionless model equations

We proceed by introducing dimensionless variables for every quantity we wish not to vary. Recall, that each physical quantity can be written as:

$$\mathbf{p} = p[\tilde{p}], \tag{34}$$

where $\tilde{p}$ is a dimension, as meters or seconds for example, and p is a dimensionless number. Introducing a characteristic scale for a variable and dividing by it, we replace for example the magnetic field via: $B \to B' = B/\hat{B}$. Since both, B and $\hat{B}$ are dimensional quantities, B' is dimensionless. Let us define the following new variables:

$$\begin{aligned} t' = \gamma t \quad x' = \frac{1}{l}x \quad \phi' = \frac{1}{\varphi}\phi \quad \eta' = \frac{1}{\gamma l^2}\eta \\ R' = \frac{R}{l} \quad \rho' = \frac{l^2}{M_0}\rho \quad B' = \frac{\gamma l^2}{\varphi}B \end{aligned} \tag{35}$$

By substituting these into the vorticity Eqn. (33), we obtain new dimensionless equations:

$$\left(\frac{\partial}{\partial t'} + \underline{\hat{z}} \times \nabla'\varphi' \cdot \nabla'\right)\Omega' + \frac{2T}{\gamma^2 mlnR}\frac{\partial}{\partial y'}n = \eta'\nabla_\perp^2\Omega' \tag{36}$$

$$\left(\frac{\partial}{\partial t'} + \underline{\hat{z}} \times \nabla'\varphi \cdot \nabla'\right)n = \kappa'\nabla_\perp^2 n. \tag{37}$$

We now drop the prime from the new variables and introduce the Poisson bracket formalism:

$$\{\phi, \psi\} = \frac{\partial\phi}{\partial x} \times \frac{\partial\psi}{\partial y} - \frac{\partial\phi}{\partial y} \times \frac{\partial\psi}{\partial x}.$$

The model equations read now:

$$\frac{\partial\Omega}{\partial t} + \{\phi, \Omega\} + \frac{2T}{\rho R l \gamma^2}\frac{\partial n}{\partial y} = \kappa\nabla_\perp^2\Omega \tag{38}$$

$$\frac{\partial n}{\partial t} + \{\phi, n\} = \mu\nabla_\perp^2 n. \tag{39}$$

With proper boundary conditions, these two coupled equations can now be solved numerically as an initial value problem. Adding additional expressions for the parallel current is done by applying the same normalization as in Eqn. (35) to the corresponding terms.

They are friction coefficients for each variable and related to the Rayleigh number, Ra, and Prandtl number of classical hydrodynamics via:

$$Ra = \frac{1}{\kappa\mu} \quad Pr = \frac{\kappa}{\mu}.$$

The Rayleigh number is ratio of buoyancy and diffusion rates of momentum. While diffusion acts as a stabilizing force to the system, buoyancy tends to destabilize the system.
The Prandtl number is a measure for the ratio of viscosity and collisional diffusion.
These parameters are not to be confused with collisional frequencies between ions, electrons and neutrals.

The free parameters in the model equations Eqn. (38) and Eqn. (39) are the electron temperature T, mass density ρ, major radius of the tokamak R, the characteristic length l, the ideal interchange time $1/\gamma$ and the diffusion parameters κ, μ. By defining the ideal interchange time $1/\gamma$ correctly, we can absorb most of these parameters into the normalization of the model. This leaves us with two models, that have two and three free parameters respectively.

2.6.2 Model for small blob amplitude.

First we present a minimalistic model with diffusion coefficients for θ and Ω as the only two free parameters. We start with separating the full plasma particle density n into a constant background particle density N and a variable perturbation term $\eta(x, y)$:

$$n = N + \eta. \tag{40}$$

We insert this for the interchange term and assume small particle density perturbations, $\left|\frac{\eta}{N} \ll 1\right|$. This gives us:

$$\frac{2T}{\rho R l \gamma^2}\frac{\partial n}{\partial y} = \frac{2T}{mRNl\gamma^2}\frac{\partial \eta}{\partial y}.$$

We now introduce the characteristic particle density perturbation amplitude, Δn, defined by: $\mathcal{O}(\eta/\Delta n) = 1$:

$$\frac{2T}{mRl\gamma^2}\frac{\Delta n}{N}\frac{\partial}{\partial y}\frac{\eta}{\Delta n}.$$

The obvious definition for the ideal interchange time is

$$\gamma = \sqrt{\frac{2T}{mRl}\frac{\Delta n}{N}},$$

this choice gives unity as a factor for the interchange term in Eqn. (38). Using this, and defining the dynamic field θ in Eqn. (39) as the normalized particle density perturbation:

$$\theta = \frac{\eta}{\Delta n}, \tag{41}$$

we obtain the model equations:

$$\frac{\partial\Omega}{\partial t}+\{\phi,\Omega\}+\frac{\partial\theta}{\partial y}=\mu\nabla_\perp^2\Omega \tag{42}$$

$$\frac{\partial\theta}{\partial t}+\{\phi,\theta\}=\kappa\nabla_\perp^2\theta. \tag{43}$$

The free parameters in this model are the diffusion coefficients μ and κ. From the dimensional model equations we see, that κ is the non-dimensional diffusion coefficient, and μ is the non-dimensional viscosity coefficient.
The dynamical field θ is the particle density perturbation on a uniform background plasma. This quantity is normalized to a characteristic perturbation and assumed to be small.

2.6.3 Model for large blob amplitude

If we do not linearize the interchange term for small particle density perturbations, we write with the full particle density from Eqn. (40):

$$\frac{2T}{mR(N+\eta)l\gamma^2}\frac{\partial}{\partial y}\eta=\frac{2T}{mRl\gamma^2}\frac{\partial\,(N+\eta)}{\partial y}\frac{1}{N+\eta}=\frac{2T}{mRl\gamma^2}\frac{\partial\ln(1+\hat\eta)}{\partial y}.$$

We obtain a factor of unity for the interchange term by choosing:

$$\frac{1}{\gamma}=\sqrt{\frac{2T}{mRl}}.$$

Dividing Eqn. (39) by the full particle density n, we obtain for the non-linearized model:

$$\frac{\partial\Omega}{\partial t}+\{\phi,\Omega\}+\frac{\partial\ln n}{\partial y}=\mu\nabla_\perp^2\Omega \tag{44}$$

$$\frac{\partial\ln n}{\partial t}+\{\phi,\ln n\}=\kappa\left(\nabla_\perp^2\ln n-(\nabla_\perp\ln n)^2\right). \tag{45}$$

For this model, the dynamic field in Eqn. (39) corresponds to the logarithm of the full particle density:

$$\ln n=\ln\left(1+\frac{\eta}{N}\right)=\ln\left(1+\hat\eta\right). \tag{46}$$

Here we defined the normalized particle density perturbation $\hat\eta=\eta/N$. This dynamic variable is not the same, as the normalized particle density perturbation θ for the linearized model. They relate as:

$$\hat\eta=\frac{\Delta n}{N}\theta \quad \ln n=\ln\left(1+\frac{\Delta n}{N}\theta\right).$$

Together with the diffusion coefficients for vorticity and particle density, this model has three free parameters.

A comparison of the parameters in both models is listed in Tab. 1. Note that we use the effective gravity defined by $g = 2C_s^2/R$, with the ion acoustic speed $C_s = T_e/m_i$, for describing the ideal interchange time. Note that this implies a different normalization of the diffusion coefficients κ and μ in both models. Their numerical values are not directly comparable.

Model	Free Parameters	Inverse ideal interchange time γ
Linearized	2: κ, μ	$\gamma_l = \gamma_0\sqrt{\hat{\eta}} = \sqrt{\frac{g}{l}\hat{\eta}}$
Non linearized	3: κ, μ, $\Delta n/N$	$\gamma_0 = \sqrt{\frac{g}{l}}$

Table 1: Free parameters for both models.

2.6.4 Sheath dissipation

As a parallel current divergence, we include this effect by adding an additional term to the vorticity equations for the respective model, Eqn. (42) or Eqn. (44). Our approach is to take the average these equations along a magnetic field line. We define an averaging operator:

$$\langle \cdot \rangle = \frac{1}{2L_\parallel} \int_{L_\parallel}^{L_\parallel} dl.$$

where $2L_\parallel$ is the connection length of a magnetic field line and dl is a line element of the field line.

The vorticity equation of the linearized model reads with the parallel current term included:

$$\frac{\partial \Omega}{\partial t} + \{\phi, \Omega\} + \frac{\partial \theta}{\partial y} = \nabla_\parallel J_\parallel.$$

Assuming that the such defined averaging operator commutes with all spatial derivatives, we write

$$\langle \frac{\partial \Omega}{\partial t} \rangle = \frac{\partial \langle \Omega \rangle}{\partial t}, \quad \langle \{\phi, \Omega\} \rangle = \{\langle \theta \rangle, \langle \Omega \rangle\}, \quad \langle \frac{\partial}{\partial y}\theta \rangle = \frac{\partial}{\partial y}\langle \theta \rangle.$$

Note that in general the averaging operator does not commute with the Poisson brackets. By assuming that do commute, we implicitly assume that the structures do not vary along the field lines. We need to compute $\langle \nabla_\parallel J_\parallel \rangle$ explicitly. Assuming only slow variations along magnetic field lines assuming small potential perturbations, we Taylor expand all terms including ϕ and find:

$$\langle \nabla_\parallel J_\parallel \rangle = \frac{enC_s}{L_\parallel} \frac{e\phi}{T}.$$

We employ the normalizations from Eqn. (35) and find for the physical sheath dissipation parameter

$$\sigma_{\text{phys}} = \frac{2C_s}{L_{\|}\rho_s^2},$$

where $C_s = \sqrt{T/m}$ and $\rho_s = C_s/\omega_{c,i}$. The dimensionless, field averaged model equations read:

$$\begin{aligned}\frac{\partial \Omega}{\partial t} + \{\phi, \Omega\} + \frac{\partial \theta}{\partial y} &= \mu \nabla_\perp^2 \Omega - \sigma \phi \qquad (47)\\ \frac{\partial \theta}{\partial t} + \{\phi, \theta\} &= \kappa \nabla_\perp^2 \theta.\end{aligned}$$

where the sheath dissipation parameter σ is given by:

$$\sigma = \frac{2C_s l^2}{\gamma L_{\|}\rho_s}. \tag{48}$$

The physical picture is presented in Fig. 7. While the blob travels radially outwards with V_X, sheath currents stretch the blob along open field lines towards the divertor targets. Both processes happen simultaneously and on different characteristic scales. Radial blob transport is of order V_{X} with a characteristic blob length scale l, introduced in Eqn. (35). This defines a characteristic blob transit time scale $t = l/V_{\text{X}}$. A similar scale is introduced for the parallel dynamics via the connection length $L_{\|}$ and the acoustic velocity C_s, $\tau_{\|} = C_s/L_{\|}$.

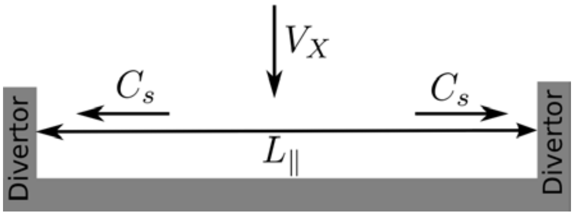

Figure 7: Simplified picture of the current system in the SOL. While the blob travels radially outwards with V_X, sheath currents expand the blob along the open field lines running into the divertor targets. The sheath currents have velocity C_s and are separated by the connection length $L_{\|}$.

3 Method

To numerically solve the model equations, we develop a Fourier-Galerkin method on a two dimensional, rectangular domain with periodic boundary conditions. This is implemented in the `2dads` program, a solver for two dimensional advection diffusion problems. Documentation for the code is found under [2]. In this chapter we present the spectral Fourier-Galerkin method, and time integration method used, for solving the model equations. Spectral methods for hydrodynamical problems are a well known tool and one finds many excellent discussions on this topic, as in [9] and [37]. We further describe the diagnostic and output routines of the `2dads` code. We choose a spectral method to solve the model equations, because their rate of convergence is usually better than any finite difference formula.

3.1 Simulation domain setup

The rectangular physical domain we simulate is $[-L_x : +L_x] \times [-L_y : +L_y]$. Periodic boundary conditions on this domain read then $u(x, y) = u(x+2L_x, y) = u(x, y+2L_y)$, where u may be θ or Ω. We discretize this grid by using a cell centered grid, using N_x equidistant points in the x direction and M_y equidistant points in the y direction. A cell centered grid, the values of the physical field lie between two adjacent grid points. The position of the gridpoints in physical space is then given by:

$$
\begin{aligned}
x_n &= -L_x + \left(n - \frac{1}{2}\right) \triangle_x \quad \text{for } n = 0, \dots, N_+1 \\
y_m &= -L_y + \left(m - \frac{1}{2}\right) \triangle_y \quad \text{for } m = 0, \dots, M_y + 1.
\end{aligned} \tag{49}
$$

This gives a spacing of $\triangle_x = 2L_x/N_x$ between two adjacent points in the x direction and a spacing of $\triangle_y = 2L_y/M_y$ between two adjacent points in the y direction. For an easy implementation of periodic boundary conditions, we also include ghost points in the domain, therefore we define $M_y + 1 \times N_x + 1$ grid points in Eqn. (49). Ghost points are positioned around the simulation domain at the same distance as the points in the physical domain, as shown in Fig. 8(a). In Fig. 8(b) we present a periodic function with period $2L_x = 2.0$. Assigning the ghost points $x_{N+1} := x_1$ and $x_0 := x_N$ guarantees that the function has the same value at $x = 0$ and $x = 2 \times L_x$ and is thus periodic. Extending this principle to a two-dimensional domain is straight forward.

3.2 Spectral discretization

The partial differential equation system we are simulating is given by:

$$
\begin{aligned}
\frac{\partial \Omega}{\partial t} + \{\phi, \Omega\} + \frac{\partial \theta}{\partial y} &= \mu \nabla_\perp^2 \Omega + \mathcal{L}_\Omega(\phi) \\
\frac{\partial \theta}{\partial t} + \{\phi, \theta\} &= \kappa \nabla_\perp^2 \theta + \mathcal{L}_\theta(\phi).
\end{aligned} \tag{50}
$$

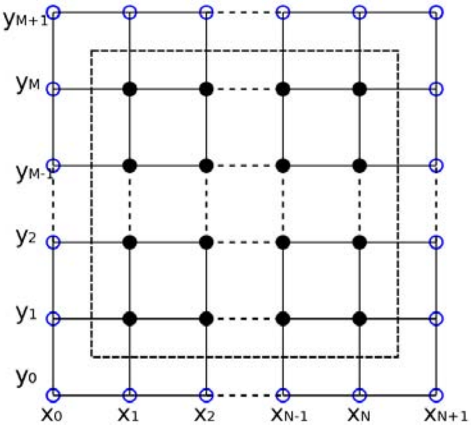

(a) Simulation grid for `2dads` . The physical domain is within the black dashed rectangle. Discretization points of the physical domain are denoted with filled black circles. Ghost points are denoted in blue.

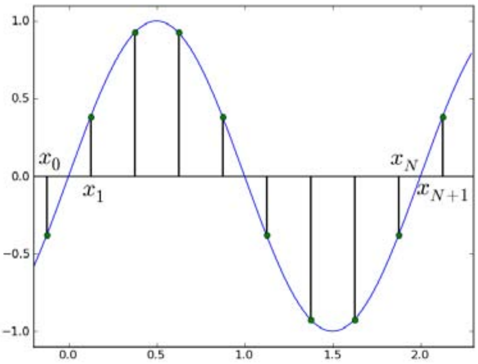

(b) A function with period $L = 2.0$ on a cell centered grid discretized with 8 gridpoints on the domain $(0.0, 2.0)$.

Here, the terms $\mathcal{L}_u(v)$ means any (non-)linear operator, acting on the field u and v. In praxis we substitute terms for sheath dissipation, and additional terms for the linearized model Eqn. (44) here. Periodic boundary conditions are assumed in both directions and initial conditions for θ and Ω are given explicity:

$$\begin{aligned}\theta(\mathbf{x}, t = 0) &= \theta_0(\mathbf{x}), \\ \Omega(\mathbf{x}, t = 0) &= 0,\end{aligned} \tag{51}$$

in case of no initial flow. A discretization with a spectral method consists of multiple steps and are well documented, as for example in [9]. We first define a linear space of test functions X_N in which we expand the function Ω and θ we wish to solve for. We also need to define a linear space of trial functions Y_N and discrete representation of the non-linear operator $\{\cdot,\cdot\}$ and the linear operators $\nabla_\perp^2$ and $\frac{\partial}{\partial y}$. We continue by expanding the fields Ω and θ in the base of the test space X_N. We denote the fields expanded in this function space with Ω^N / θ^N and substitute them into the model equations. The residual of these equations is then defined as

$$\begin{aligned} \frac{\partial \Omega^N}{\partial t} + \{\phi^N, \Omega^N\} + \frac{\partial \theta^n}{\partial y} - \mu \nabla_\perp^2 \Omega^N - \mathcal{L}_\Omega(\phi^N) \\ \frac{\partial \theta^N}{\partial t} + \{\phi^N, \theta^N\} - \kappa \nabla_\perp^2 \theta^N - \mathcal{L}_\theta(\phi^N). \end{aligned}$$

Demanding that the residuals vanish, when projected on the space of test functions Y_N is the crucial demand that all spectral methods have in common. By defining a proper orthogonal projection operator $\langle\cdot,\cdot\rangle$, we write this as:

$$\begin{aligned} \left\langle \frac{\partial \Omega^N}{\partial t} + \{\phi^N, \Omega^N\} + \frac{\partial \theta^n}{\partial y} - \mu \nabla_\perp^2 \Omega^N - \mathcal{L}_\Omega(\phi^N) v \right\rangle = 0, \\ \left\langle \frac{\partial \theta^N}{\partial t} + \{\phi^N, \theta^N\} - \kappa \nabla_\perp^2 \theta^N - \mathcal{L}_\theta(\phi^N), v \right\rangle = 0, \end{aligned}$$

where$\Omega^N, \theta^N, \phi^N \in X_N$ and $\forall v \in Y_N$. One is free to choose any set of test functions X_N and trial functions Y_N which give rise to many different spectral methods. For our study of biperiodic domains, the truncated Fourier series is suitable, as their base functions arise naturally for periodic problems. Their base functions all satisfy the boundary conditions individually and form a complete orthogonal base for continuous, infinitely smooth functions on $\mathbb{R}^2$. The physical fields Ω and θ are assumed to be included in this space. We can also make use of readily available implementations of the discrete Fourier transformation.

3.3 Spectral Fourier Galerkin method

For a Fourier-Galerkin method we choose the trial space $X_N \otimes X_M$ and the space of test functions $Y_N \otimes Y_M$ to be the product of all trigonometric polynomials with degree $\leq N/2$ and $\leq M/2$, respectively.

$$X_N \otimes X_M = Y_N \otimes Y_M = \{e^{ik_n x} e^{ik_m y} \mid n = -N/2, \ldots, N/2-1,\ m = -M/2, \ldots, M/2-1\}.$$

The operator $\otimes$ denots the vector space product. This basis set is associated with the discrete Fourier transformation. It is well discussed in standard literature, [37, 9] present a thourough and well written discussion. Along with these functions, we introduce the wave numbers k_n and k_m

$$k_n = \begin{cases} n \triangle_{k_x}, & \text{for} \quad n = 0 \ldots N_x/2, \\ (n - N_x) \triangle_{k_x}, & \text{for} \quad n = N_x/2 + 1 \ldots N_x - 1, \end{cases}$$

with k_m is defined analog. We also define the spacing between two wavenumbers as $\triangle_{k_n} = 2\pi/2N_x$ and $\triangle_{k_m} = 2\pi/2M_y$.

The expansion of a field $u(x, y, t)$ in these base functions defines the discrete Fourier coefficients of a real valued function on the domain $[-L_x : L_x] \times [-L_y : L_y]$:

$$\widehat{u}_{k_n,k_m} = \sum_{j=1}^{N_x} \sum_{l=1}^{M_y} u(x_j, y_l) e^{-ik_n x_j} e^{-ik_m y_l}. \tag{52}$$

From the definition of k_n and k_m above, we note, that Eqn. (52) is periodic in n and m with length N_x and M_y. Asuming $\mathcal{O}(N) = \mathcal{O}(M)$, which we do for the rest of this section, the operation count according to this formula in $\mathcal{O}(N^2)$. In praxis one uses Fast Fourier transformations (FFT) which have an operation count $\mathcal{O}(N \log N)$. The inversion formula is given by:

$$u(x_j, y_l) = \frac{1}{N_x M_y} \sum_{k_n=-N_x/2}^{N_x/2-1} \sum_{k_m=-M_y/2}^{M_y/2-1} \hat{u}_{k_n,k_m} e^{ik_n x_j} e^{ik_m y_l}, \tag{53}$$

which presumes the orthogonality relation

$$\frac{1}{N_x} \sum_{j=0}^{N_x-1} e^{(-ipx_j)} = \begin{cases} 1 & \text{if} \quad p = Nz, z \in \mathbb{Z} \\ 0 & \text{otherwise} \end{cases} \tag{54}$$

Note that in Eqn. (53), k_n and k_m respectivly vary over negative and positive values, whereas in Eqn. (52) i and j in Eqn. (52) vary over positive values only. This is due to the periodicity of k_n: $k_n(n) = k_n(n + N)$, a summation $k_n = 1 \dots N_x$ in Eqn. (53) is equivalent to our formulation. This hold for k_m respectively. We choose this convention since it is often found in literature, [9].

Inverse Fourier transformation are also computed with a FFT algorithm and have an operation count of $\mathcal{O}(N \log N)$. In this thesis we use the discrete Fourier transform, DFT , for the transformation from the field grid point values in real to their Fourier coefficients in Eqn. (52) and the inverse discrete Fourier transformation, IDFT for the transformation of the Fourier coefficients to the field grid points in Eqn. (53). Assuming that the $u(x_j, y_l)$ are real, the presented discrete Fourier transformation maps $N_x M_y$ real values to $N_x M_y$ complex values. One can compute, that the discrete Fourier transformation has a hermitian symmetry for real values:

$$u(x_j, y_l) \text{ is real} \rightarrow \widehat{u}(k_x, k_y) = \widehat{u}^\dagger(-k_x, -k_y). \tag{55}$$

This shows, that half of the numbers in the Fourier series are rendundant, and we can interpret the discrete Fourier transformation as $1 : 1$ mapping between $N_x M_y$ real valued numbers and $N_x M_y/2$ complex numbers. Implementations, as [13] used for our work, use this to save half the memory used for storing Fourier coefficients.

Approximating the fields θ and Ω with their truncated Fourier series gives:

$$\Omega^{N_x,M_y}(x_j,y_l) = \sum_{n=-N_x/2}^{N_x/2-1}\sum_{m=-M_y/2}^{M_y/2-1} \hat{\Omega}_{k_n,k_m} e^{(ik_n x_j)} e^{(ik_m y_l)} \tag{56}$$

$$\theta^{N_x,M_y}(x_j,y_l) = \sum_{n=-N_x/2}^{N_x/2-1}\sum_{m=-M_y/2}^{M_y/2-1} \hat{\theta}_{k_n,k_m} e^{(ik_n x_j)} e^{(ik_m y_l)}, \tag{57}$$

where we use the same number N_x and M_y of modes for the Fourier transformation along the x and y direction as we use for grid points. Notice that the ghost points are not included in the Fourier Transformation. The fields are to be periodic with lengths $2L_x$, $2L_y$. Including these points in the Fourier transformation will consider the function to be periodic with lengths $2(L_x + \triangle_x)$, $2(L_y + \triangle_y)$, thereby introducing artificial ringing artefacts.

We obtain an ordinary differential equation (ODE) for each Fourier coefficient $\widehat{\Omega}_{k_n,k_m}$ and $\widehat{\theta}_{k_n,k_m}$ by inserting the truncated Fourier series representation of the fields ,Eqn. (56) and Eqn. (57), into the model equations and require that the residual is orthogonal to every test function in $Y_n \times Y_m$,

$$\left\langle \frac{\partial \Omega}{\partial t}^{N_x,M_y} + \{\phi^{N_x,M_y},\Omega^{N_x,M_y}\} + \frac{\partial \theta^{N_x,M_y}}{\partial y} - \mu\nabla_\perp^2\Omega^{N_x,M_y} - \mathcal{L}_\Omega(\phi^{N_x,M_y}), Y_n \times Y_m \right\rangle = 0 \tag{58}$$

$$\left\langle \frac{\partial \theta}{\partial t}^{N_x,M_y} + \{\phi^{N_x,M_y},\theta^{N_x,M_y}\} - \kappa\nabla_\perp^2\theta^{N_x,M_y} - \mathcal{L}_\theta(\phi^{N_x,M_y}), Y_n \times Y_m \right\rangle = 0. \tag{59}$$

As an orthogonal projection operator for $\langle\cdot,\cdot\rangle$ we use the scalar product

$$\langle u, v\rangle = \int_{-L_y}^{L_y} dy \int_{-L_x}^{L_x} dx\ u \times v^\dagger,$$

where $\dagger$ denotes complex conjugation. With this definition, the test and trial functions obey the orthogonality relation $\langle X_n X_m, Y_{n'} Y_{m'}\rangle = \delta_{n,n'}\delta_{m,m'}$. Applying this to the demand that the residuals of the discretized partial differential equations (PDEs), vanish when projected on the trial functions, Eqn. (58), and Eqn. (59), we obtain a system of $2 \times N_x \times M_y$ coupled ODEs

$$\frac{\partial \hat{\Omega}_{k_n,k_m}}{\partial t} + \{\widehat{\phi^{N_x,M_y},\Omega^{N_x,M_y}}\}_{k_n,k_m} + k_n\hat{\theta}_{k_n,k_m} = -\mu(k_n^2+k_m^2)\hat{\Omega}_{n,m} + \widehat{\mathcal{L}_\Omega(\phi^{N_x,M_y})}_{k_n,k_m} \tag{60}$$

$$\frac{\partial \hat{\theta}_{k_n,k_m}}{\partial t} + \{\widehat{\phi^{N_x,M_y},\theta^{N_x,M_y}}\}_{k_n,k_m} = -\kappa(k_n^2+k_m^2)\hat{\theta}_{k_n,k_m} + \widehat{\mathcal{L}_\theta(\phi^{N_x,M_y})}_{k_n,k_m}, \tag{61}$$

Array index	1	...	$\frac{N}{2}$	$\frac{N}{2}+1$	...	$N-1$	N
Pos. frequency	0	...	$\frac{1}{2}$	$\frac{N}{2}$	...	$\frac{N-1}{N}$	1
Neg. frequency	0	...	$\frac{1}{2}$	$-\frac{1}{2}$	...	$1-\frac{1}{N}$	$-\frac{1}{N}$

Table 2: Position of frequency elements in 1 dimensinoal arrays used in `2dads`

one equation for each single Fourier coefficient $\widehat{\Omega}_{n,m}$ and $\widehat{\theta}_{n,m}$.
The initial condition for the Fourier Coefficients $\widehat{\theta}_{k_n,k_m}$ and $\widehat{\Omega}_{k_n,k_m}$ are given by the truncated Fourier Series of Eqn. (51):

$$\widehat{\theta}_{k_n,k_m}(t=0) = \sum_{j=1}^{N_x} \sum_{l=1}^{M_y} \theta_0(x_j, y_l) \exp(-ik_n x_j) \exp(-ik_m y_l) \tag{62}$$

$$\widehat{\Omega}_{k_n,k_m}(t=0) = 0. \tag{63}$$

This is a well defined initial value problem that can be solved by time integration of the Fourier coefficients. In our implementation we employ the `FFTW` library which readily provides routines for arbitrary size DFTs. Special attention is payed to the order in which the Fourier coefficients are stored to correctly implement spatial derivation routines. Spatial derivation is given for Fourier series by:

$$\frac{\partial}{\partial x} \widehat{u}^N = ik_x \widehat{u}^N.$$

The position in which the Fourier coefficients for each frequency is stored is presented in Tab. 2. The frequencies are stored in rising order, and the associated negative frequencies are listed below. When this scheme is extended to two dimensions, only the first $\frac{N}{2}+1$ frequencies are stored along the first array dimension, due to the hermitian property of the Fourier coefficients for real fields from Eqn. (55).

A special treatment is required for the Fourier coefficients of the poisson brackets. They are given by:

$$\begin{aligned}
\widehat{\{\phi^{N_x,M_y}, \Omega^{N_x,M_y}\}} &= \frac{\partial}{\partial x}\phi^{N_x,M_y} \frac{\partial}{\partial y}\Omega^{N_x,M_y} - \frac{\partial}{\partial y}\phi^{N_x,M_y} \frac{\partial}{\partial x}\Omega^{N_x,M_y} \\
&= \left(\frac{2\pi i n}{N_x}\right) \left(\sum_{n=-N_x/2}^{N_x/2-1} \sum_{m=-M_y/2}^{M_y/2-1} \widehat{\Omega}_{k_n,k_m} \right) \times \left(\frac{2\pi i m'}{M_y}\right) \left(\sum_{n'=-N_x/2}^{N_x/2-1} \sum_{m'=-M_y/2}^{M_y/2-1} \widehat{\phi}_{k_{n'},k_{m'}} \right) \\
&\quad - \left(\frac{2\pi i m}{M_y}\right) \left(\sum_{n=-N_x/2}^{N_x/2-1} \sum_{m=-M_y/2}^{M_y/2-1} \widehat{\Omega}_{k_n,k_m} \right) \times \left(\frac{2\pi i n'}{N_x}\right) \left(\sum_{n'=-N_x/2}^{N_x/2-1} \sum_{m'=-M_y/2}^{M_y/2-1} \widehat{\phi}_{k_{n'},k_{m'}} \right).
\end{aligned}$$

This is a convolution in spectral space, with an operation cost of approxemately $\mathcal{O}(N^4)$. By transforming the fields into real space, performing a component-wise multiplication of the spatial derivated fields there and transforming the product back into Fourier space, the operation cost for the evaluation of the term reduces to $\mathcal{O}(N^2 \log N)$.

$$\begin{aligned}\widehat{\{\phi^{N_x,M_y}, \Omega^{N_x,M_y}\}} =& \text{DFT (IDFT } \left(\frac{\partial}{\partial x}\phi^{N_x,M_y}\right) \times \text{IDFT } \left(\frac{\partial}{\partial y}\Omega^{N_x,M_y}\right)) \\ &- \text{DFT (IDFT } \left(\frac{\partial}{\partial y}\phi^{N_x,M_y}\right) \times \text{IDFT } \left(\frac{\partial}{\partial x}\Omega^{N_x,M_y}\right)).\end{aligned}$$

By doing this, we introduce an aliasing error, which arises since we use truncated Fourier series and not their infinite counterpart. Let a general quadratic product term be

$$w(x,y) = u(x,y)v(x,y),$$

where u and v are real valued two-dimensional fields. Assuming that both u and v are represented by their infinite Fourier series, we find for the truncated Fourier Series of w:

$$\widehat{w}_{k,l} = \sum_{k_x+k'_x=k} \sum_{k_y+k'_y=l} \widehat{u}_{k_x,k_y} \widehat{v}_{k'_x,k'_y}.$$

In this summation, $k_x, k'_x = -N_x/2 \dots N_x/2-1$ and $k_y, k'_y = -M_y/2 \dots M_y/2-1$.
If we instead assume, that u and v are given by their truncated Fourier series, we get:

$$\widehat{w}_{k,l} = \sum_{k_x+k'_x=k} \sum_{k_y+k'_y=l} \widehat{u}_{k_x,k_y} \widehat{v}_{k'_x,k'_y} + \sum_{k_x+k'_x=k\pm N} \sum_{k_y+k'_y=l\pm M} \widehat{u}_{k_x,k_y} \widehat{v}_{k'_x,k'_y}. \tag{64}$$

The second term on the right hand side is called the aliasing error. It arises because the inverse transformation back to Fourier space of the product $\widehat{u}_{k_x,k_y}\widehat{v}_{k'_x,k'_y}$ wraps large frequencies back to the frequencies included in the original transform. Summation over k_y and k'_y, or k_x and k'_x respectively, give additional terms that satisfy Eqn. (54), and are non-zero. For example, if $N = M = 128$, the frequency $k = 3$ includes contributions from the frequency pairs $(k_x, k'_x) = (-61,-64), (-62,-63), (-63,-62)$ and $(-64,-61)$ for Eqn. (64). This is schematically drawn in Fig. 8. We read from the figure, that the power of large frequencies are artificially increased. This source of artificial energy shows that energy is not exactly conserved in the method we use.

There are many methods used to remove the aliasing error. One method is to zero pad all frequencies $|k|, |l| \geq 2N/3, 2M/3$. Other approaches are to multiple the Fourier coefficients with a filter function. We choose not to remove the aliasing error, as in prominent opinion, it is not needed for good accuracy in Pseudospectral methods. (Reference: Spectral methods in hydrodynamics, p.211). Our simulations are aliased.

In order to evaluated the advection terms in configuration space, we use the arakawa scheme, presented in [4]. It is a finite difference scheme for the poisson bracket, which exactly conserves

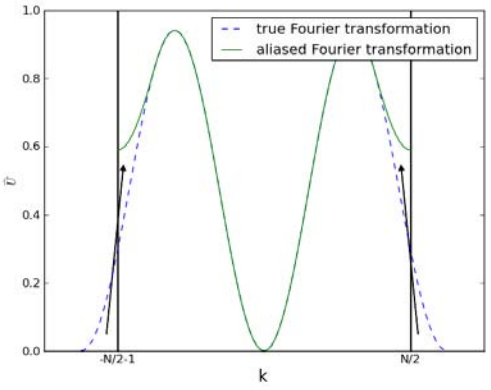

(c) Interpretaion of the aliasing error. Frequencies $|k| \geq N/2$ for the infinite Fourier transformation are wrongly assigned to frequencies $|k| < N/2$ for the discrete Fourier transformation. Taken from [37]

Figure 8: Aliasing error

.

energy and enstrophy. This is important, as non-linear terms couple all different length scales of the system, and thereby have the possibility to exchange energy between them. It is implemented via:

$$\begin{aligned}
\{u, v\} = -\frac{1}{12\triangle x \triangle y}((&u_{i,j-1} + u_{i+1,j-1} - u_{i,j+1} - u_{i+1,j+1}) \times (v_{i+1,j} - v_{i,j}) \\
&+ (u_{i-1,j-1} + u_{i,j-1} - u_{i-1,j+1} - u_{i,j+1}) \times (v_{i,j} - v_{i-1,j}) \\
&+ (u_{i+1,j} + u_{i+1,j+1} - u_{i-1,j} - u_{i-11,j+1}) \times (v_{i,j+1} - v_{i,j}) \\
&+ (u_{i+1,j-1} + u_{i+1,j} - u_{i-1,j-1} - u_{i-1,j}) \times (v_{i,j} - v_{i,j-1}) \\
&+ (u_{i+1,j} + u_{i,j+1}) \times (v_{i+1,j+1} - v_{i,j}) \\
&+ (u_{i,j-1} + u_{i-1,j}) \times (v_{i,j} - v_{i-1,j-1}) \\
&+ (u_{i,j+1} + u_{i-1,j}) \times (v_{i-1,j+1} - v_{i,j}) \\
&(u_{i+1,j} + u_{i,j-1}) \times (v_{i,j} - v_{i+1,j-1})).
\end{aligned}$$

The error of this scheme is of order $\mathcal{O}(\triangle^4)$. We read that it only depends on the nearest neighbors on the simulation grid. To evaluate this expression for the nodes $x_{n,1}$ for $n = 1 \ldots N_x$ and $y_{m,1}$ for $m = 1 \ldots M_y$, we need ghost points. This is another reason to include ghost points in the simulation.

Order	α_0	α_1	α_2	α_3	β_1	β_2	β_3
1	1	1	0	0	1		0
2	3/2	2	$-1/2$	0	2	-1	0
3	11/6	3	$-3/2$	1/3	3	-3	1

Table 3: Values for the α and β coefficients for stiffly stable time integration for first, second and third order accuracy.

Time integration Time integration is done by a K$^{\mathrm{th}}$ order stiffly stable time integration, presented in [14]. It is used to integrate the generalized diffusion equation:

$$\frac{\partial U}{\partial t}(x,t) = \kappa \frac{\partial^2 U}{\partial^2 x} + \mathcal{L}(U), \tag{65}$$

where $\mathcal{L}$ is a well defined differential operator, acting on U. Let u denote a discretization of U, a stiffly stable time integration scheme for u is then defined by:

$$\frac{1}{\triangle_t}\left(\alpha_0 u^i - \sum_{k=1}^{K} \alpha_k u^{i-k}\right) = \kappa \delta_{\mathbf{x}}^2 u^i + \sum_{k=1}^{K} \beta_k \mathcal{L}(u^{i-k}) + \mathcal{O}(\triangle_t^K).$$

In the equation above, the operator $\delta_{\mathbf{x}}$ denotes spatial differntiation. Upper indices denote the time index. In the form above, the scheme has an error $\triangle_t^K$, where K is a natural number. The coefficients α_k and β_k are determined by the order of the scheme K. In Tab. 3 we present the coefficients used for first, second and third order time integration.

Choosing $K = 1$ yields a first order forward finite difference scheme, which converges for any choice of $\triangle_t$. Due to its low accuracy, a higher order scheme is commonly used. In all applications of this time integration scheme, we use third order accuracy whenever possible. The first K timesteps have to be integrated with lower accuracy though. Starting with $K = 1$, one succesively increases accuracy for each time integration in the first $K - 1$ time steps.

We see that the diffusion part of Eqn. (65) is treated implicitly, whereas all other terms in the equation are treated explicitly. Solving the previous equation for u^i, we get:

$$u^i = \frac{1}{\alpha_0 - \kappa \delta_x^2} \sum_{k=1}^{K} \left(\alpha_k u^{i-k} + \beta_k \mathcal{L}(u^{i-k})\right) + \mathcal{O}(\triangle_t^K). \tag{66}$$

Extending the above scheme to two spatial dimensions, we get a stiffly stable scheme for the time integration of the Fourier coefficients $\widehat{u}^i_{\underline{k}}$ of the two fields by:

$$\widehat{u}^i_{\mathbf{k}} = \frac{1}{\alpha_0 + \kappa(k_x^2 + k_y^2)} \sum_{k=1}^{K} \left(\alpha_k \widehat{u}^{i-k} + \beta_k \mathcal{L}(\widehat{u}^{i-k})\right) + \mathcal{O}(\triangle_t^K). \tag{67}$$

When we integrate the Fourier coefficients $\widehat{\theta}_{k_n,k_m}$ and $\widehat{\Omega}_{k_n,k_m}$ with Eqn. (66), the spatial derivative operator is replaced with the exact relation $\delta_{\mathbf{x}}^2 \widehat{\theta}_{k_x,k_y} = -(k_x^2 + k_y)^2 \widehat{\theta}_{k_x,k_y}$.

Parameter	Name	Description
xleft	x_{left}	Left simulation domain boundary
xright	x_{right}	Right simulation domain boundary
yup	x_{up}	Upper simulation domain boundary
ydown	x_{down}	Lower simulation domain boundary
Nx	N_x	Number of discretization points along x direction
My	M_y	Number of discretization points along y direction
tlevs	K	Time levels used for time integration
deltat	Δ_t	Time step length
tend	t_{end}	Time when simulation ends
tout	t_{out}	Time between full solution output
tdiag	t_{diag}	Time between diagnostic output
nthr	n_{thread}	Number of threads
chunk	chunk	Chunksize

Table 4: Input parameters, their symbols and their description used in the `2dads` program.

3.4 Simulation setup

To run a simulation with `2dads` , we need to provide proper initial conditions for the fields θ and Ω, and we need to provide parameters to the simulation, time step and simulation domain size among others. Simulation parameters are listed in Tab. 4. The first four parameters are used to set the simulation domain. They are related to the lengths in x– and y–direction via $L_x = x_{\text{right}} - x_{\text{left}}$ and $L_y = y_{\text{up}} - y_{\text{down}}$. The number of discretization points N_x and M_y determine the number of Fourier modes that are computed for the fields θ, Ω and ϕ. This corresponds to the number of grid points used in configuration space for the discretization. The order of the stiffly stable time integration scheme is given by K . The first i, $i < K$ steps are integrated with a lower order of i. By choosing a time step length of Δ_t , diagnostic output is written out every $t_{\text{diag}} / \Delta_t$ time integrations, and full output is written out every $t_{\text{out}} / \Delta_t$ time integrations. Parallelization is supported by the `FFTW` library and has been implemented with `OpenMP` by `2dads` as a part of this thesis. The number of threads working on a problem is set by n_{thread} . For loop parallelization, this is divided among the n_{thread} threads in `2dads` , so that each thread works on *chunk* matrix elements parallel.

3.5 Full output

`HDF5` was chosen as a data container, because the output grows very large and this data format is designed to handle large and complex data sets. It allows hierarchical data storage and allows data to be stored in a binary format.

The `2dads` program is rewritten to include output routines for the full solutions of the fields θ, Ω and ϕ in the `HDF5` format. Setting the parameter *tout* in file *input.ini* configures in which time intervalls the full output of the solution is written. In cases when we integrate the two parameter model with linearized interchange term, we write

$$\begin{aligned}\theta(x_n, y_m) n &= 1 \dots N_x \; m = 1 \dots M_y \\ \Omega(x_n, y_m) n &= 1 \dots N_x \; m = 1 \dots M_y \\ \phi(x_n, y_m) n &= 1 \dots N_x \; m = 1 \dots M_y\end{aligned}$$

to the output file.

The dynamic variable θ is the normalized particle density perturbation of a background particle density for the linearized model:

$$\theta = \frac{\eta}{\Delta n}$$

and the full normalized particle density for the non-linearized model:

$$\theta = 1 + \frac{\eta}{N}.$$

A `HDF5` container file `output.hdf5` is created when the `2dads` program starts. In this file, we create a data tree with nodes *omega*, *theta* and *strmf*. Each time step where full output is to be written, we append the output as a new dataset in the according group and enumerate them, starting from 0. The data tree in the file looks like:

```
output.hdf5 / Omega / 000 - (Nx * My) array of double precision numbers
/ 001 - (Nx * My) array of double precision numbers
...
/ Omega / (tend/dtout) - (Nx * My) array of double precision numbers
/ Theta / 000 - (Nx * My) array of double precision numbers
/ 001 - (Nx * My) array of double precision numbers
/ (tend/dtout) - (Nx * My) array of double precision numbers
...
/ Strmf / 000 - (Nx * My) array of double precision numbers
/ 001 - (Nx * My) array of double precision numbers
/ (tend/dtout) - (Nx * My) array of double precision numbers
...
```

A method to read data as initial conditions for θ and Ω from the `HDF5` container file has also been developed. This allows simulations to resume if they are aborted for any reason. A drawback is that the first K time steps have to be integrated with lower order time integration schemes.

3.6 Diagnostic output

The original `2dads` code writes many diagnostic output data. A full list is presented in Tab. 3.6. The parameter `tdiag` in the input file gives the time intervall, in which diagnostic output is written to the according files. The output format for the files is plain ascii, with tab delimited values. All output for one time step is written in one line.

In this thesis we discuss blob motions with the help of COM coordinates. Here we motivate the use of these coordinates and discuss them briefly.
The center of mass coordinates X_{COM} and Y_{COM} are defined via:

$$\begin{aligned} X_{\mathrm{COM}} &= \frac{1}{\int d\underline{x}\theta} \int d\underline{x} x \theta \\ Y_{\mathrm{COM}} &= \frac{1}{\int d\underline{x}\theta} \int d\underline{x} y \theta \end{aligned} \tag{68}$$

and the respective velocities are their time derivatives:

$$\begin{aligned} V_{\mathrm{X}} &= \frac{dX_{\mathrm{COM}}}{dt} \\ V_{\mathrm{Y}} &= \frac{dY_{\mathrm{COM}}}{dt} \end{aligned}$$

To describe the dynamics of a spatially extended structure, one could use other definitions of position and velocity. One could think of the dynamics of a pronounced, typical feature of the whole structure, as a trailing front for example. One advantage of using center of mass coordinates is that they are independent of any parameter. One can also show, that for a domain with periodic boundary conditions in both directions, the radial COM velocity is proportional to the convective radial flux:

$$\frac{\partial X_c}{\partial t} = V_x = \frac{1}{Q} \frac{\partial}{\partial t} \int d\underline{x} x \theta \tag{69}$$

$$= -\frac{1}{Q} \int d\underline{x} \theta \phi_y . \tag{70}$$

The radial flux is the plasma density transported with the radial component of the $E \times B$ drift, ϕ_y. The equation states, that all properties of the convective radial flux of the simulated plasma filaments are given by the radial COM velocity.
The integrated particle density is written out in the variable tint :

$$\mathrm{tint} = \sum_{n=1}^{N_x} \sum_{m=1}^{M_y} \theta(x_m, y_m)_x \times \Delta_y \tag{71}$$

Since θ is used for different dynamic variables in the linearized and non-linearized model, the COM velocity has is not directly comparable between the two models. When we assume an

Variable	Explanation	Defined in eq.
X_{COM}	Radial center of mass coordinate	Eqn. (68)
V_{X}	Radial center of mass velocity	Eqn. (69)
tint	Integrated dynamic variable θ for particle density	Eqn. (71)

Table 5: Compendium of `2dads` diagnostic output

initial condition $\theta(t=0) = \exp\left(-\underline{x}^2/2\right)$ for the linearized model and $\hat{n} = 1 + \Delta n/N \times \theta(t=0)$ for the non-linearized model, we find:

$$V_X^{\mathrm{lin}} = \frac{1}{2\pi} \int d\underline{x}\ \underline{x}\theta \tag{72}$$

$$V_X^{\mathrm{nonlin}} = \frac{\frac{\Delta n}{N}}{A + \frac{\Delta n}{N}} \times V_X^{\mathrm{lin}}. \tag{73}$$

To obtain comparable diagnostic output for both models, we compute the COM velocity for the non-linear model with the field $\hat{n} - 1$. Using this in the equations for V_X^{nonlin} above, we eliminiate the factor in front of the integral and both COM velocities are of the form in Eqn. (72).

4 Variation of Rayleigh number

Varying the Rayleigh number allows us to categorize the motions that the two fluid model allows. We study the blobs dynamic and evolution under variation of the Rayleigh number, which is defined as.

$$\mathrm{Ra} \; = \frac{1}{\kappa\mu}.$$

Here κ is the dimensionless viscosity parameter and μ is the non-dimension diffusion parameter of the model. It can be interpreted as the ratio between buoyancy forces to dissipative forces. Buoyancy forces are the strength of the effective gravity mechanism in our model.

We begin by presenting convergence studies of the spectral `2dads` code. Here, we determine parameters, such as resolution, and number of Fourier modes we need, for a converged simulation. We continue by presenting a discussion of the simulation results. This covers blob evolution, where we discuss the phenomena we see in the simulation, as well as center of mass dynamics of the structures.

The simulation results are then be compared to results from the original `2dads` code, where periodic boundary conditions are used in the radial direction. A final result of this chapter is the scaling of V_{X} with increasing Rayleigh number.

4.1 Simulation setup and convergence tests

A plasma blob structure is modelled by an initial gaussian density profile without any initial vorticity:

$$\begin{aligned}\theta(x,y) &= \exp\left(-\frac{x^2}{2} - \frac{y^2}{2}\right)\\ \Omega(x,y) &= 0.\end{aligned}$$

Vorticity will be generated by the interchange term in Eqn. (26)), the y derivative of the initial particle density.

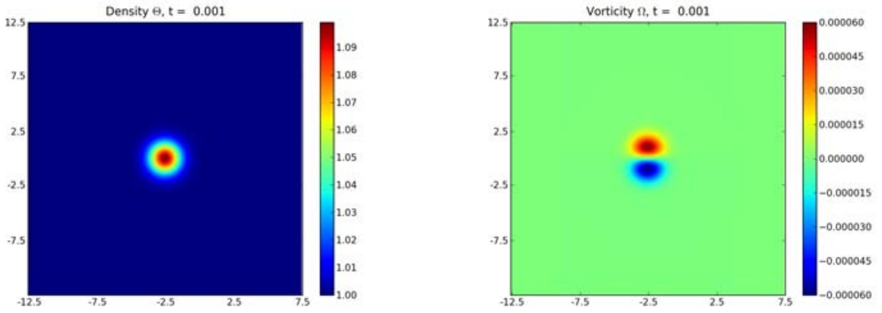

(a) Density perturbation at $t = 0.0$

(b) Vorticity at $t = 1 \times 10^{-3}$

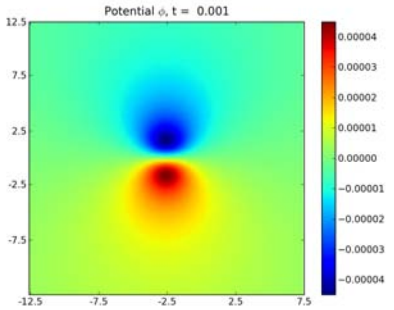

(c) Electrostatic potential at $t = 1 \times 10^{-3}$

Figure 9: Initial development of the phyical fields. Simulation parameters: $\kappa = \mu = 10^{-2}$, $\Delta t = 10^{-3}$, 512×512 modes on a 50×50 domain.

Low resolution parameter scan To qualitatively asses the variety of motions that occur by variation of the Rayleigh number, we run the parameter scan in Tab. 6). In all simulations the Prandtl number is held to unity. We do not use the results of these simulations for parameter scaling studies, as we run all simulations with low resolutions and have not achieved convergence.

The result of these simulations are used for convergence tests with different parameters. We need to determine box size and number of modes for which the simulation results change little when increased further. Contour plots of θ and Ω show, that with increasing Rayleigh number structures on increasingly smaller scales evolve. They demand a increasingly high resolution, an increasing number of modes. Before we discuss these structures, we determine box sizes and number of modes, for which these structures are resolved well enough with a fixed Rayleigh number. These so determined parameters are used for simulations with smaller Rayleigh number, to give a converged simulation.

Run #	Resolution	Domain	Δ_t	κ	μ	$Ra(\kappa, \mu)$
1	256×256	$[-5:30] \times [-15:15]$	1.0×10^{-3}	5×10^{-1}	5×10^{-1}	4×10^{0}
2	256×256	$[-5:30] \times [-15:15]$	1.0×10^{-3}	2×10^{-1}	2×10^{-1}	2.5×10^{1}
3	256×256	$[-5:30] \times [-15:15]$	1.0×10^{-3}	1×10^{-1}	1×10^{-1}	1×10^{2}
4	256×256	$[-5:30] \times [-15:15]$	1.0×10^{-3}	5×10^{-2}	5×10^{-2}	4×10^{2}
5	256×256	$[-5:30] \times [-15:15]$	1.0×10^{-3}	2×10^{-2}	2×10^{-2}	2.5×10^{3}
6	256×256	$[-5:30] \times [-15:15]$	1.0×10^{-3}	1×10^{-2}	1×10^{-2}	1×10^{4}
7	256×256	$[-5:30] \times [-15:15]$	1.0×10^{-3}	5×10^{-3}	5×10^{-3}	4×10^{4}
8	384×384	$[-5:30] \times [-15:15]$	1.0×10^{-4}	2×10^{-3}	2×10^{-3}	2.5×10^{5}
9	384×384	$[-5:30] \times [-15:15]$	1.0×10^{-4}	1×10^{-3}	5×10^{-3}	1×10^{6}
10	512×512	$[-5:30] \times [-15:15]$	1.0×10^{-4}	5×10^{-4}	5×10^{-4}	4×10^{6}
11	512×512	$[-5:30] \times [-15:15]$	1.0×10^{-4}	2×10^{-4}	2×10^{-4}	2.5×10^{7}
12	512×512	$[-5:30] \times [-15:15]$	1.0×10^{-4}	1×10^{-4}	1×10^{-4}	1×10^{8}

Table 6: Rayleigh number parameter scan with a low resolution parameter set.

Test for convergence, $Ra = 10^2$ A low Rayleigh number means that dissipative forces dominate over effective buoyancy forces. The blob evolves slowly shows pronounced dispersion, damping the evolution of small scale structures, due to collisional diffusion. In Fig. 4.1 we present the radial COM position and velocity of the plasma blob. It has a sharp peak at $t \approx 6$, aftwards the velocity decreases uniformly.

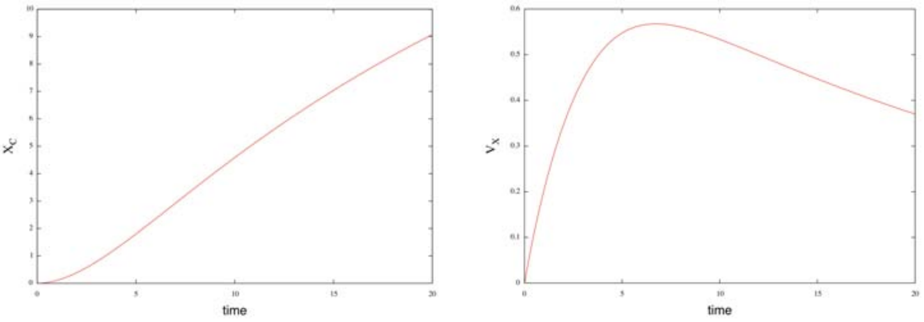

(a) Radial COM coordinate

(b) Radial COM velocity

Figure 10: Center of mass coordinates for blob simulation on 35x30 domain with 256×256 modes resolution

The influence of the domain size on V_X can be understood by Fig. 4.1. In physical space, θ and Ω have exponentially decaying tails in both directions whereas the potential ϕ has an algebraically decaying tail. This can cause ϕ to become box filling. On a finite domain size with biperiodic boundary conditions we always have to enforce an artificial zero crossing for the potential. This effects the shape of the potential over the whole domain, causing unphysical effects in the advection terms $\{\phi, \theta\}$ and $\{\phi, \Omega\}$.

We have to increase the box size so far, that ϕ has sufficiently enough decayed towards the simulation domain boundaries, so that the enforced zero crossing has no significant influence on the shape of ϕ. On the other hand, the resolution decreases linearly with the simulation domain when the number of modes is fixed. Therefore the simulation domain should not be made too big, just big enough.

A simulations is converged with respect to box size, when the finite size effects influences on the electrostatic potential is negligible. In Fig. 4.1 we present the decay of the electrostatic potential along the poloidal direction at the radial position where ϕ assumes its maximum. For a domain size of 50×50 we see a strong forced zero crossing, along with a gradient of $\mathcal{O}(10^{-2})$ at the domain boundaries. With increasing resolution, the gradient of the tail of the potential decreases to $\mathcal{O}(10^{-4})$ on a 400×400 domain. The finite size effect on the radial COM velocity is shown in Fig. 11, comparing run #2, #3, #4 and #12 from Tab. 7. For a domain size of 50×50, the time and position of the velocity peak is strongly affected by finite size effects. For run #3, #4 and #12, the variation of $\max(V_\text{X})$ is of order $\mathcal{O}(10^4)$ and the time of peak velocity varies from 7.09 - 7.16 ideal interchange times. We see that finite size effects have less impact on $\max(V_\text{X})$ than they have on the time where the blob reaches its peak velocity, $t(V_\text{X} = \max(V_\text{X}))$.

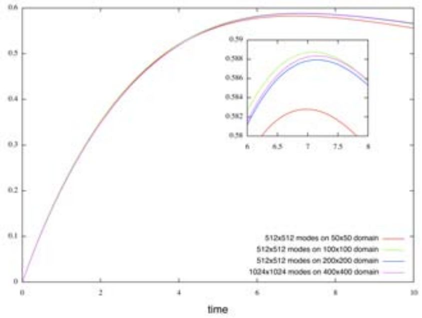

Figure 11: Finite box size effects on radial COM velocity peaks for Ra $= 10^2$. We see a variation in peak velocity amplitude and position.

In Fig. 4.1 we see that the COM velocity decreases when we keep increasing the domain size. We see a decrease in V_X with increasing box size. For simulation with 512×512 the differences between the curves is larger than for 1024×1024, because the Nyquist frequency is lower for 1024×1024. This shows the demand for a high number of modes for large domain sizes. Simulations with a domain sizes over 200×200 are too craving to be considered.

Next, we increase the number of modes until the simulation is converged with respect to resolution. For $Ra = 10^2$ we have done this procedure for different simulation domains to estimate the resolution needed on a broader variety of domains. In Fig. 14 we present the radial COM velocity for an increasing number of modes on different simulation domains. We see that the velocity increases with increasing mode number. With decreasing number of modes the velocity decreases, as was found with increasing simulation domain. From Tab. 7 we see that $\max(V_\text{X})$ is a robust quantity, it varies little even when the simulation has not

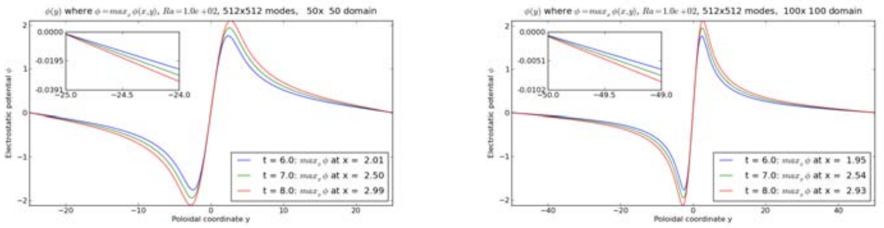

(a) Domain 50 × 50, Gradient $\phi_y \approx= -0.027$ for $t = 7.0$, at the left boundary

(b) Domain 100 × 100, Gradient $\phi_y \approx= -0.007$ for $t = 7.0$, at the left boundary

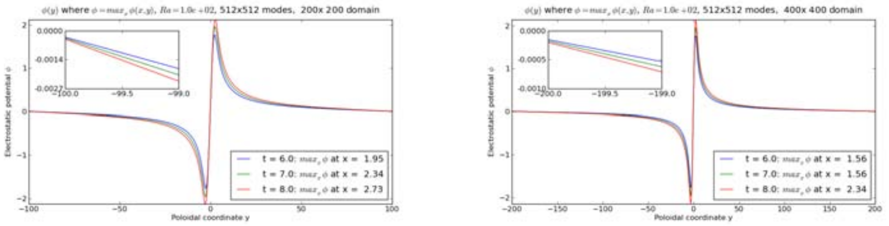

(c) Domain 200 × 200, Gradient $\phi_y \approx= -0.001$ for $t = 7.04$, at the left boundary

(d) Domain 400 × 400, Gradient $\phi_y \approx= -0.0008$ for $t = 7.0$, at the left boundary

Figure 12: Decay of ϕ for increasing box sizes, Ra $=10^2$, resolution: 512 × 512 modes.

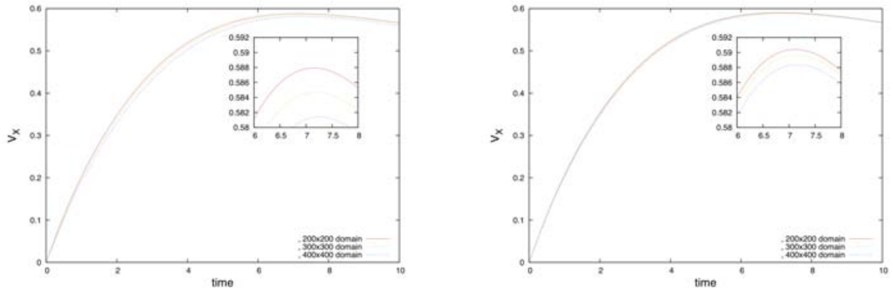

(a) Ra $=10^2$, resolution: 512 × 512

(b) Ra $=10^4$, resolution: 1024 × 1024

Figure 13: Variation for radial COM velocity V_X with increasing simulation domain.

converged yet.

For the radial COM velocity curves in Fig. 14 we find exactly the same behaviour. The COM velocity increases for increasing resolution and decreases for insufficient resolution. The COM velocity increases very little above a resolution of 512 × 512 on a 200 × 200 domain. When we increase the domain size, the convergence is slower. On a 400 × 400 domain, one needs at least 1024 × 1024 modes resolution for convergence.

For high resolution simulations with $Ra \leq 10^2$ we therefore use a resolution of 512 × 512 modes on a 200 × 200 domain.

run #	Domain size	Resolution	$\max(V_\mathrm{X})$	$t(v = \max(V_\mathrm{X})\ )$	change of $\max(V_\mathrm{X})$
1	30 × 30	256 × 256	0.56751984	6.74	–
2	50 × 50	512 × 512	0.58279198	6.98	–
3	100 × 100	512 × 512	0.58873445	7.09	101,02% rel. to run #2
4	200 × 200	512 × 512	0.58792788	7.15	100,88% rel. to run #2
5	300 × 300	512 × 512	0.58470076	7.19	100,32% rel. to run #2
6	400 × 400	512 × 512	0.58140004	7.26	99,76% rel. to run #2
7	200 × 200	768 × 768	0.58974326	7.13	100,31% rel. to run #4
8	300 × 300	768 × 768	0.58823854	7.16	100,61% rel. to run #5
9	400 × 400	768 × 768	0.58604425	7.18	100,80% rel. to run #6
10	200 × 200	1024 × 1024	0.59040397	7.12	100,42% rel. to run #4
11	300 × 300	1024 × 1024	0.58965820	7.14	100,84% rel. to run #5
12	400 × 400	1024 × 1024	0.58834738	7.16	101,19% rel. to run #6

Table 7: Convergence test for Ra $= 10^2$, presenting $\max(V_\mathrm{X})$ and $t(V_\mathrm{X} = \max(V_\mathrm{X}))$ for different resolutions. The last column shows the change in $\max(V_\mathrm{X})$ relative to other runs from column 1.

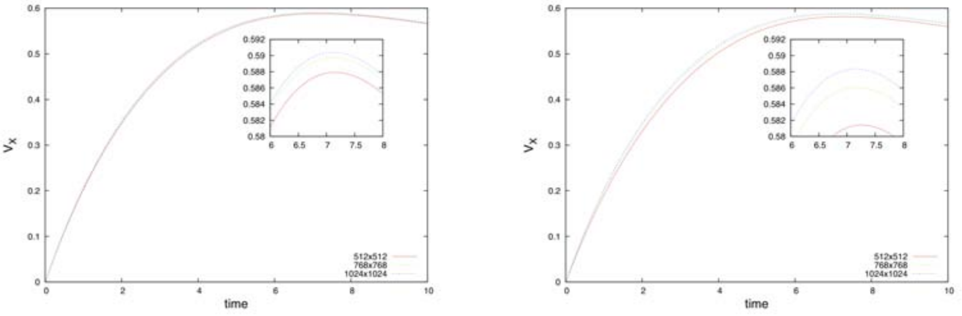

(a) 200 × 200 Domain

(b) 400 × 400 Domain

Figure 14: Convergence behaviour on different domains, Ra $=10^2$

Test for convergence, $Ra = 10^4$ Increasing the effective buoyancy will cause smaller scale structures to develop. To resolve this numerically we need a higher resolution than for $Ra = 10^2$. The initial blob velocity has the same characteristics as the previous run, but it reaches its peak velocity quicker, already at $t \approx 5.0$ as shown in Fig. 15. We also see that the peak velocity has increased from about 0.6 with Ra $= 10^2$ to about 0.82. After it has reached its maximum velocity, the blob quickly decelerates, reaches a plateau and decelerates again. These are effects due to dispersion of the blob structure.

In Fig. 16 we study convergence for the box size. We again demand that the potential and its gradient are negligible at the boundaries of the simulation domain in the time where the blob approaches its maximum velocity. Keeping the number of modes fixed to 512 × 512, we study the decay of ϕ for a 50 × 50, 100 × 100 and 200 × 200 domain. For a domain size

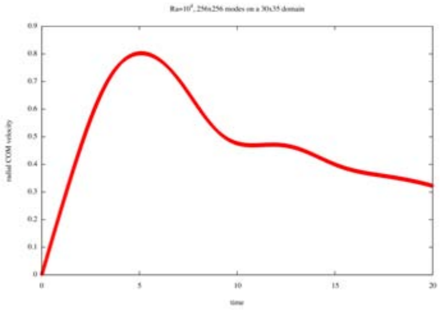

Figure 15: COM velocity for unconverged run, 256 × 256 modes, domain: $30x35$

of 50 × 50, the forced zero crossing leads to a large gradient of ϕ in the poloidal direction. A simulation domain of 100 × 100 shows also a negligible value of ϕ at the boundaries, Its gradient is $\phi_y \approx 0.005$ at the boundaries for $t = 5.0$ when the blob has reached peak velocity. After reaching peak velocity, the blob will diffuse which leads to a larger spatial extension of the potential (red curve in Fig. 16). A domain size of 200 × 200 shows am even better decay, the gradient of ϕ is negligible value at the boundary. We can gain further insight in the magnitude of the finite size effects by comparing ϕ at $y = 50$ for simulations with different resolutions. Comparing $\phi(y = 50)$ for 200 × 200 with 100 × 100, we find that for 200 × 200, it has decayed to ca. 0.01. This gives an estimate, of how strong the finite size effect are for a simulation domain of 100 × 100. The increasing demand for a number of modes and the decayed value at $\phi(y = 50)$ for the simulations on 200 × 200 are reasons for choosing a domain size of 100 × 100 for simulations with Ra =10^2.

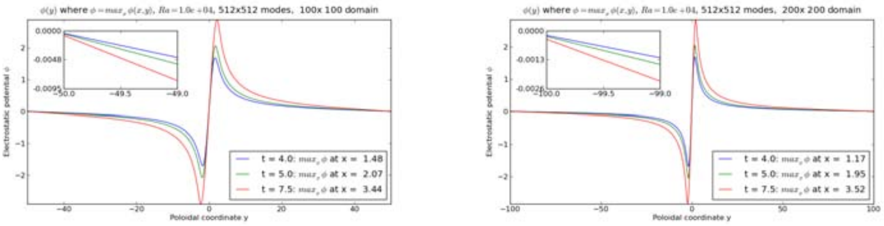

(a) Domain 100 × 100, Gradient $\phi_y \approx= -0,0045$ for $t = 5.0$, at the left boundary

(b) Domain 200 × 200, Gradient $\phi_y \approx= -0,0013$ for $t = 5.0$, at the left boundary

Figure 16: Decay of ϕ for increasing box sizes, Ra =10^4, resolution: 512 × 512 modes

We now continue by increasing the number of modes on the 100 × 100 domain, these are run # 5 – run # 7 in Tab. 8. Increasing the number of modes gives an increasing value of max(V_X) , although it is very little. Increasing the resolution increases max(V_X) by 0.5%.

The full curves are presented in Fig. 17(a), they show that although the simulations have converged with respect to $max(V_{com})$, the further evolution of the blob differs. For converged simulations we use 1536 × 1536 modes on a 100 × 100 domain when $10^2 < Ra \leq 10^4$. A

run #	Domain size	Resolution	max(V_X)	change of max(V_X) rel. to run 3
1	30×30	256×256	0.80242860	98.33 %
2	50×50	512×512	0.81462723	99.83 %
3	100×100	512×512	0.81604481	– %
4	200×200	512×512	0.80446297	98.58 %
5	100×100	768×768	0.81855297	100.31 %
6	100×100	1024×1024	0.81943268	100.41 %
7	100×100	1536×1536	0.82006007	100.48 %

Table 8: Convergence with number of modes for Ra $= 10^4$, presenting max(V_X) for different resolutions. The last column shows the change in max(V_X) relative to run #3 in column 1.

particle density profile for this simulation is shown in Fig. 17(b).

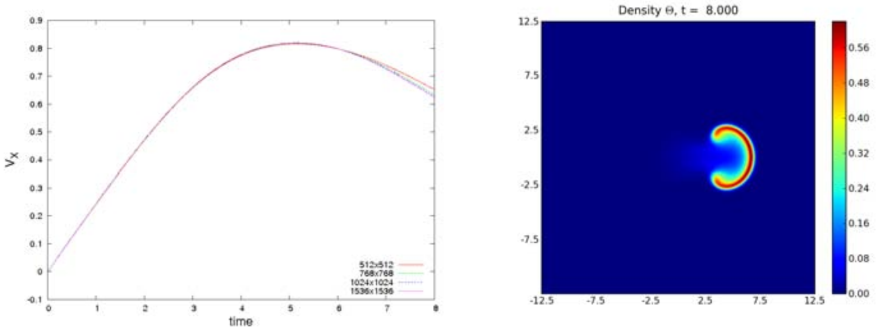

(a) max(V_X) curves for an increasing number of modes, Ra $= 10^4$, 100×100 simulation domain.

(b) Particle density at $t = 8.0$, 1536×1536 on a 100×100 domain

Figure 17: COM dynamics for an increasing number of modes and contour plot of particle density for convergence test simulations, Ra $= 10^4$.

Test for convergence, $Ra = 10^6$ In this regime,increased effective buoyancy drives the evolution of even finer scale structures. We test again for convergence on the V_X curves. In Fig. 18 we present the result from the low resolution simulation run # 9 from Tab. 6. It shows the characteristic initial acceleration and deceleration, with an increased velocity peak compared to run # 6 from the same table. The evolution after the peak velocity is also different than the previous curve.

Fig. 19 shows the amplitude of ϕ along the poloidal direction at the radial coordinate where $\phi = max(\phi)$. The gradient of ϕ is negligibly small for a box size of 100×100. On the smaller 50×50 domain, the potential shows a larger gradient. Using a larger domain is favorable to eliminate the effects of introducing an artificial decay of ϕ. Therefore we use a simulation domain of 100×100 for simulations with Ra $=10^6$, even though the simulations demand a large number of Fourier modes.

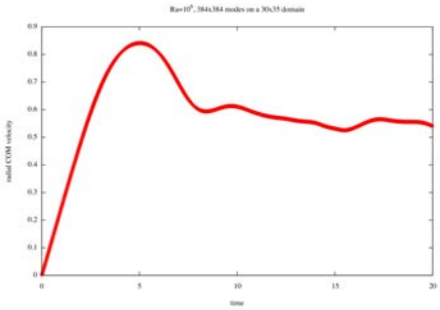

Figure 18: COM velocity for Ra =10^6. 384 × 384 modes, domain: $30x35$

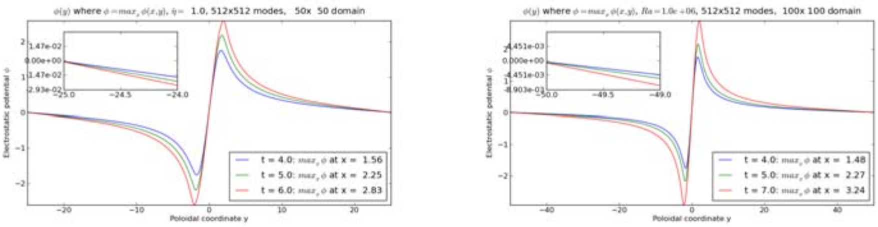

(a)

(b)

Figure 19: Decay of ϕ for increasing box sizes, Ra =10^6, resolution: 512 × 512

run #	Domain size	Resolution	max(V_X)	relative to. #3
1	30x35	384 × 384	0.84110719	98.71%
2	50 × 50	512 × 512	0.85087442	99.86%
3	100 × 100	512 × 512	0.85203522	–
4	200 × 200	512 × 512	0.83409464	97.89
5	100 × 100	1024 × 1024	0.85676980	100.56%
6	100 × 100	1536 × 1536	0.85804659	100.71 %
8	100 × 100	2048 × 2048	0.85851866	100.76 %
8	100 × 100	3072 × 3072	0.85886526	100.80 %

Table 9: Convergence with number of modes for Ra $= 10^6$, presenting max(V_X) for different resolutions. The last column shows the change in max(V_X) relative to run #3 in column 1.

Tab. 9 shows the variation in the maximal radial COM velocity when varying the number of modes. The complex small scale structures begin evolving after the blob has reached maximum velocity. Velocity curves for the test runs are presented in Fig. 20(a). We find that the curves are very close and hardly differ. But looking at the contour plots for θ we still find artefacts for resolutions ≤ 3072. In Fig. 20(b) we show cross section of the particle density at the symmetry axis $y = 0$. The artifacts in the plot for 1536 × 1536 modes show that the simulation has not converged. This is not evident from the velocity curves and underlines the importance of analyzing the fields themselves when testing for convergence.

A converged simulation is shown in Fig. 4.1 for 3072 × 3072 modes on a 100 × 100 domain. We choose this resolution for simulations where $10^4 < Ra \leq 10^6$.

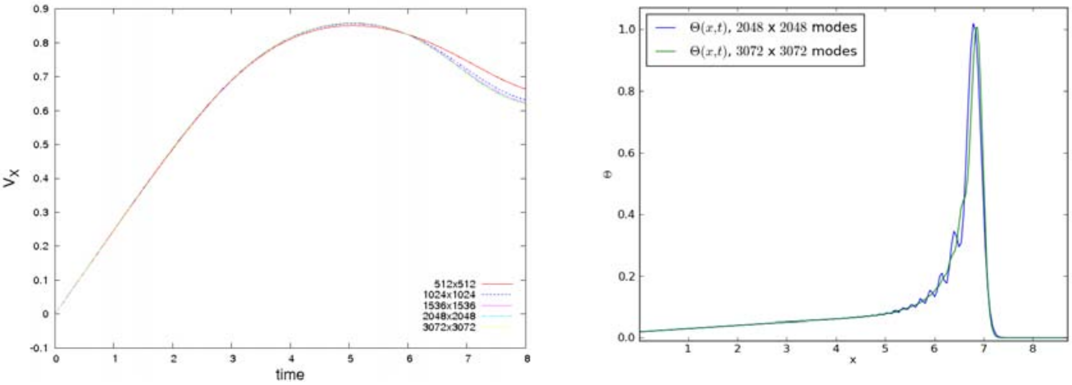

(a) Convergence with number of modes on a 100 × 100 domain.

(b) Cross section of particle density θ at $y = 0$, $t = 8.0$, Ra $=10^6$

Figure 20: Convergence with respect to number of modes for $Ra = 10^6$

4.2 Parameter scan

We now redo the simulations from Tab. 6 with the previously identified simulation parameters. This parameter scan is listed in Tab. 10.

Run	Resolution	Domain	Δ_t	κ	μ	$Ra(\kappa, \mu)$
1	512 × 512	200 × 200	10^{-3}	5×10^{-1}	5×10^{-1}	4×10^{0}
2	512 × 512	200 × 200	10^{-3}	2×10^{-1}	2×10^{-1}	2.5×10^{1}
3	512 × 512	200 × 200	10^{-3}	10^{-1}	10^{-1}	10^{2}
4	1024 × 1024	100 × 100	10^{-3}	5×10^{-2}	5×10^{-2}	4×10^{2}
5	1024 × 1024	100 × 100	10^{-3}	2×10^{-2}	2×10^{-2}	2.5×10^{3}
6	1024 × 1024	100 × 100	10^{-3}	10^{-2}	10^{-2}	10^{4}
7	3072 × 3072	100 × 100	10^{-3}	5×10^{-3}	5×10^{-3}	4×10^{4}
8	3072 × 3072	100 × 100	10^{-4}	2×10^{-3}	2×10^{-3}	2.5×10^{5}
9	3072 × 3072	100 × 100	10^{-4}	10^{-3}	10^{-3}	10^{6}
10	4096 × 4096	100 × 100	10^{-4}	5×10^{-4}	5×10^{-4}	4×10^{6}
11	4096 × 4096	100 × 100	10^{-4}	2×10^{-4}	2×10^{-4}	2.5×10^{7}
12	4096 × 4096	100 × 100	10^{-4}	10^{-4}	10^{-4}	10^{8}

Table 10: Rayleigh number parameter scan with a low resolution parameter set.

For different regions of Rayleigh numbers we find quiet a different behavior of the blob. We begin by discussing some characteristic blob evolutions for different Rayleigh numbers.

Discussion of blob evolution for $Ra = 10^2$ Blob movement with low Rayleigh numbers is characterized by dominant collisional diffusion. This diffusion inhibits the charge polarization of the interchange mechanism, so that radial advection is damped. The radial COM coordinate and velocity for simulation # 3 are presented in Fig. 21.

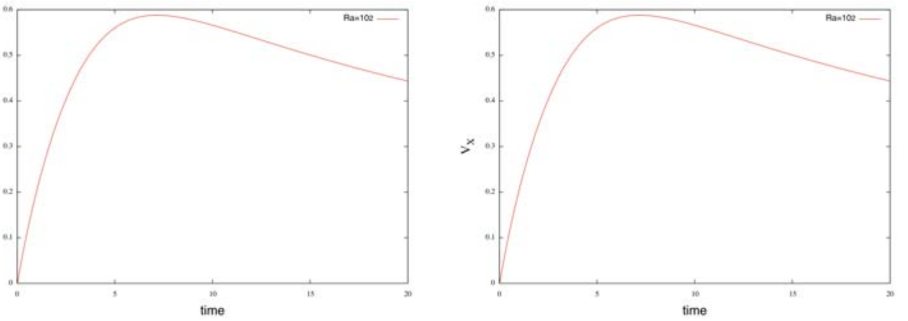

(a) COM position

(b) COM velocity

Figure 21: COM coordinates for Ra $=10^2$, simulation # 3 from Tab. 10.

The blob is immediately advected radially outwards by interchange motions as shown in Fig. 22. At $t = 5$ we see that the initially gaussian blob structure has shifted its peak some 4 units radially outward and measures now some 8 units along the poloidal and some 6 units along the radial direction. At the front a density peak has developed with a steeper gradient radially outwards than inwards. Its vertical gradients cause faster interchange motions by which vorticity is created. At the same time the plasma follows the electrostatic field lines. Differential rotation with different directions of rotation in the upper and lower half plane cause a poloidal spreading of the blob structure.

The vorticity profile has also diffused. It is drawn together to the center front of the blob and has spread apart at the right end of the blob.

At $t = 15$ the blob is bulged out in the radial direction, at the front there is a large horizontal density gradient. The vertical density gradients that have formed in the arms cause advection of vorticity outwards in the poloidal direction. The vorticity extrema are positioned right behind the high density plateau of the bulge structure. Notice that the vorticity has grown in amplitude from some 0.3 at $t = 0.5$ to some 0.9 at $t = 15$, this causes a growing swirling in the upper and lower part of the blob.

The electric potential gives the flow lines for the plasma.

At $t = 20$ we see that the particle density peak amplitude of the blob has decayed to ca 0.1, which is 10% of the initial maximum. More plasma is transported to the vorticity maxima centers, which is right behind the maximum density of the plasma.

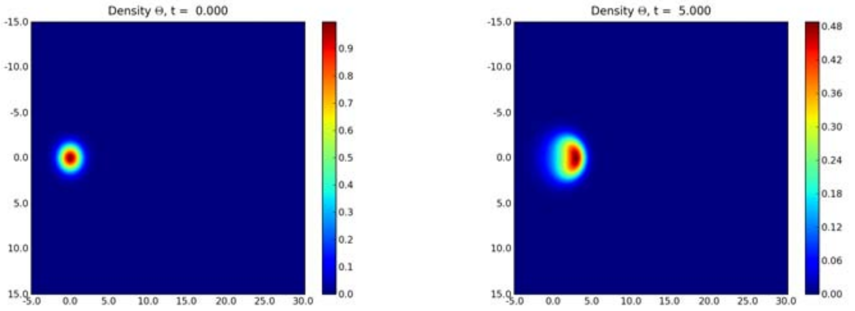

(a) Initial density, $t = 0.0$

(b) Density, $t = 5.0$

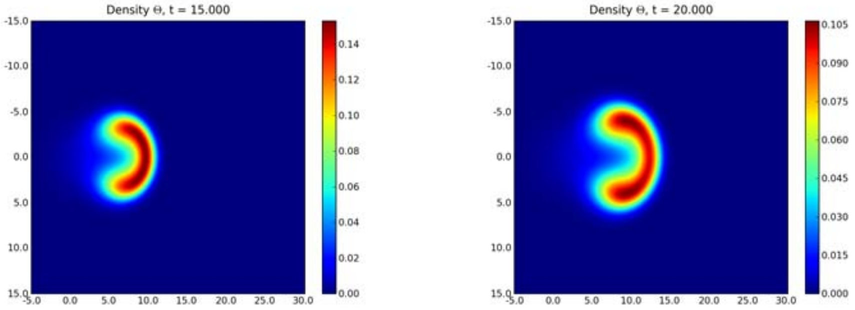

(c) Density, $t = 15.0$

(d) Density, $t = 20.0$

Figure 22: Evolution of density for $Ra = 10^2$

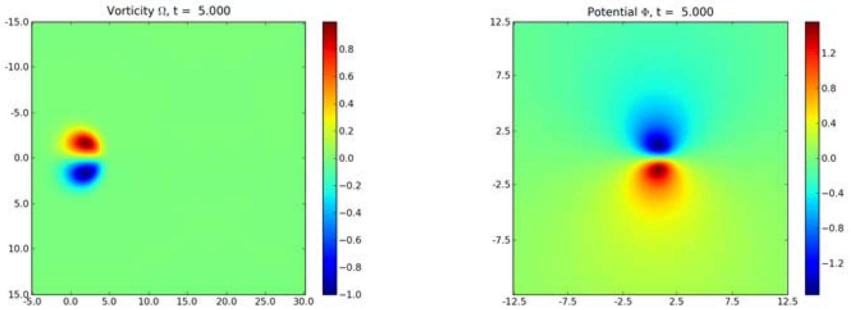

(a) Vorticity, $t = 5.0$

(b) Potential, $t = 5.0$

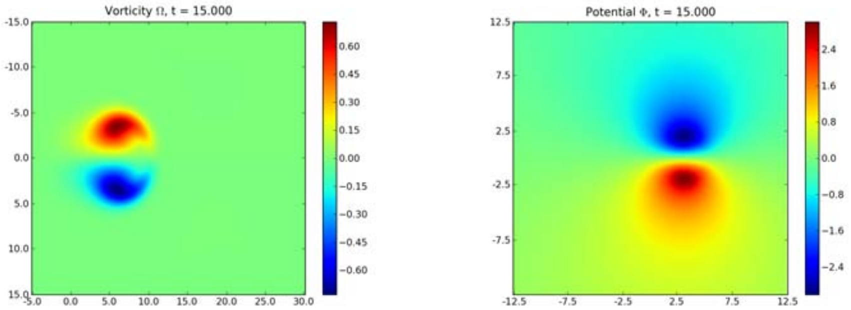

(c) Vorticity, $t = 15.0$

(d) Potential, $t = 15.0$

Figure 23: Evolution of vorticity and potential for $Ra = 10^2$

Discussion of blob evolution for $Ra = 10^4$ Increasing the effective buoyancy forces, reproduces the initial blob evolution for the low Rayleigh number case. We see a radial motion of the blob structure due to plasma polarization. During first 5 interchange time units, the evolution is comparable to the previous case. At later times though we see some significant changes. The upper and lower arms of the blob curl inwards and have large gradients for θ, the density increases and decreases over a very small spatial scale in the arms. This behavior creates a vorticity double layer through the interchange term and also contributes to increased mixing in the arm region.
Vorticity is also carried along the plasma outwards into the arms, where it causes a spiraling behavior of the arms.

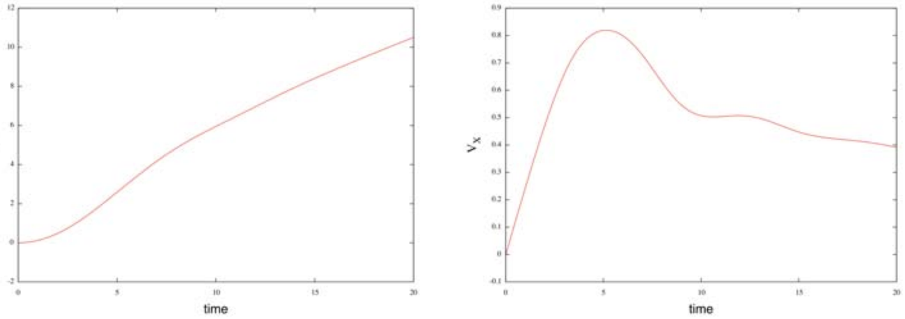

(a) COM position

(b) COM velocity

Figure 24: COM coordinates for Ra $=10^4$, simulation # 6 from Tab. 10.

At $t = 10.0$ we see that the blob as curved more than it did for $Ra = 10^2$ as shown in Fig. 25(a) The arms have curled inwards and we see a slight trail going radially inwards from the mushroom C cap. Plasma transport along the potential curves has increased causing the poloidal gradients in θ to generate more vorticity.
In the upper half it has curled counterclockwise inwards, and has stretched some 2 units further outward along the poloidal direction. This movement of the vorticity maxima is what causes the (counter–) clockwise curling of the blob arms. The vorticity structure has moved along with the particle density front as shown in Fig. 25(c).
At $t = 15.0$ we find that the particle density peak at the front of the blob has decreased considerably. The density profile for $t = 15$ is presented in Fig. 25(b), the vorticity profile is presented in Fig. 25(d).

Most of the plasma has been transported into the upper and lower lobe . Differential rotation has been transported into the curled up structures and inhibits secondary polarization of these structures. The connecting bridge between the upper and lower lobe has thinned out. The density has now spread over some 12 units in the poloidal and over some 8 units along the radial direction.
At later times the diffusive character of the plasma begins to dominate. We see further spreading of the structure which reduce poloidal density gradients, thus dampening interchange motions and vorticity generation.

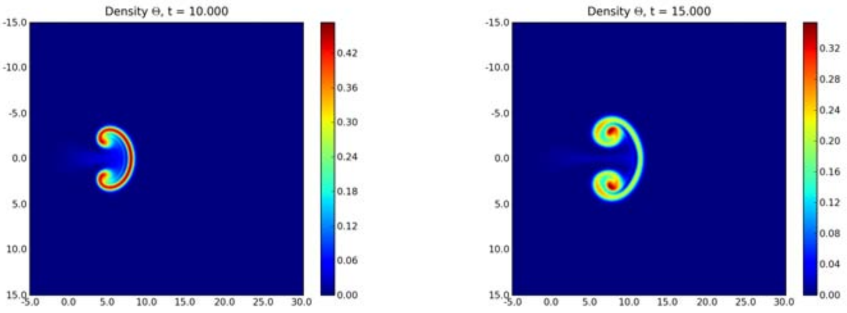

(a) Density, $t = 10.0$

(b) Density, $t = 15.0$

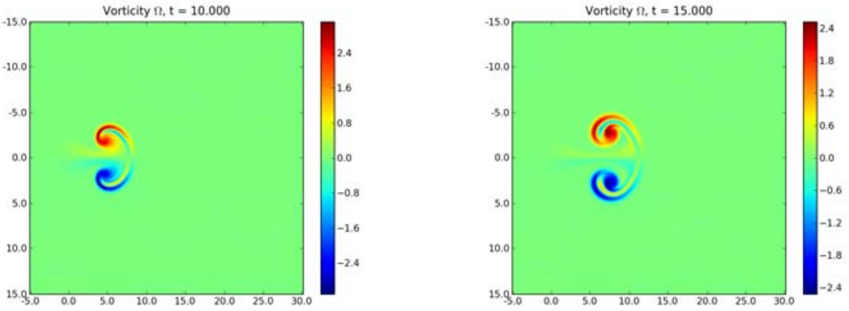

(c) Vorticity, $t = 10.0$

(d) Vorticity, $t = 15.0$

Figure 25: Evolution of density and vorticity for $Ra = 10^4$

Discussion of blob evolution for $Ra = 10^6$ Increasing the Rayleigh number to 10^6 gives a similar initial blob evolution as in the previous cases. The COM velocity in Fig. 29 presents a distinct maximum, that is followed by a region, where V_X varies only little. This is different from Fig. 24, where the COM velocity decreases continuously after the blob has reached its peak velocity.

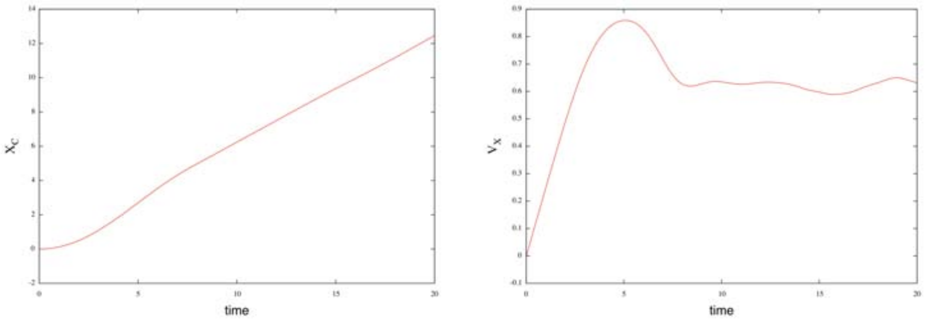

(a) COM position

(b) COM velocity

Figure 26: COM coordinates for Ra $=10^6$

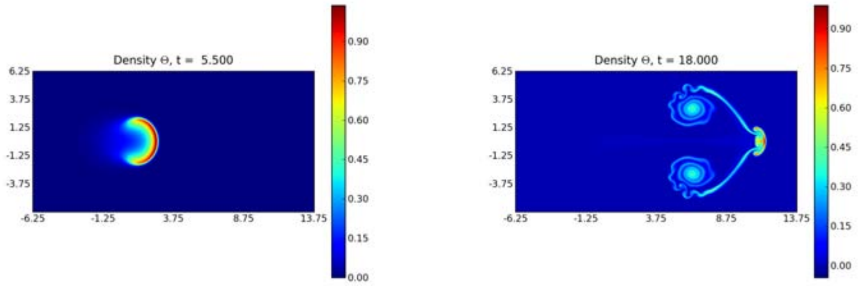

(a) Particle density, at $t(V_{\mathrm{X}} = \max(V_{\mathrm{X}}))$ $t = 5.0$

(b) Emission of a secondary blob at $t = 18.0$

Figure 27: Blob evolution for $Ra = 10^6$, simulation # 9 from Tab. 10.

A major difference is the density distribution. Due to a more rapid radial velocity, most of the plasma accumulates at the blob front. Steeper gradients in the poloidal and radial direction are the result. The curling behavior in the arms is the same, but the evolution of the front differs. Due to charge polarization at the center of the front, a plasma accumulation forms and leaves the first plasma blob with a high velocity in the radial direction. In Fig. 27 we show the blob at its time of maximum velocity and when it emits the secondary blob. We see that it is strongly dissipated and shows fine scale structures at the lobes. In Fig. 28 we present cross section at the symmetry axis $y = 0$ for the blob structure and the radial component of the electric drift, $-\phi_y$. This shows that the maximal velocity lags behind the blobs density front, amounting particles at the front. The maximum electric drift velocity increases, leading to a steep front. At $t = 18.0$, when a secondary blob is emitted from the front, we see a local increase in the radial electric drift component at the same position, where the density front is. We also observe a local maximum at $t = 18.0$ in the COM velocity curves in Fig. 26.

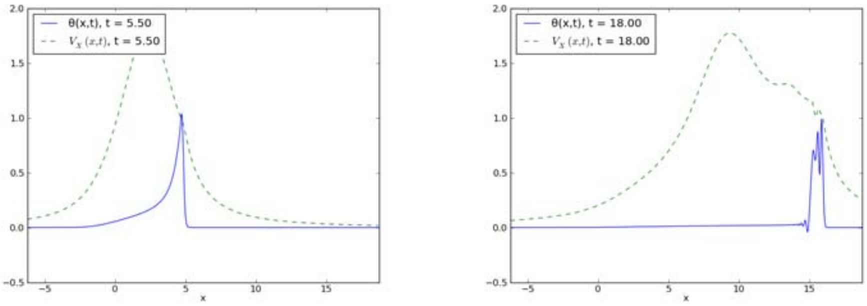

(a) $t = 5.0$

(b) $t = 18.0$

Figure 28: $E \times B$ velocity and θ cross sections at $y = 0$ for simulation with Ra $= 10^6$ on a 100×100 domain with 3072×3072 modes resolution.

4.3 Scaling properties

Quantifying the changes the blob makes over the range of Rayleigh numbers we simulated gives an insight into the nature of the blob dynamics. Comparing velocity curves in Fig. 29 we find, that the maximum for V_X becomes more pronounced with increasing Rayleigh number. Depending on the strength of the collisional forces, the time where the blob reaches its peak velocity decreases. Also does $\max(V_\mathrm{X})$ increase with increasing Rayleigh number. The evolution after its peak velocity is also different for various Rayleigh number. For lower Rayleigh numbers, the curve is smooth and shows only slight variations from a uniform decline. This is what we saw in the surface plots for the density in the earlier discussions. For larger Rayleigh numbers, we saw a different behavior. Here the strong collisional diffusion prevents the blob structure from distorting due to non-linear mixing. Ths blob structure maintains a coherent blob-like shape.

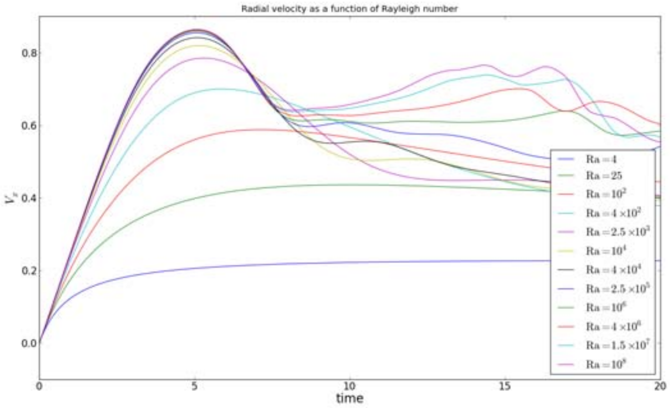

Figure 29: Radial COM velocities for all simulations from Tab. 10. The velocities increase with increasing Rayleigh number.

In Fig. 30(a) we present the scaling of V_X with Ra and compare our results to earlier results from [15]. At about Ra $= 10^5$ we see a transition into a regime, where the velocity varies only little with increasing Rayleigh number. Here $\max(V_\mathrm{X})$ approaches a limit velocity slightly less than one. Averaging $\max(V_\mathrm{X})$ for Ra $\geq 10^5$ from this figure yields 0.858 as a limit. We find a similar behavior for $t(V_\mathrm{X} = \max(V_\mathrm{X}))$. For Ra $\gtrsim 10^5$, the plasma blob reaches its peak velocity at $t \approx 5$ ideal interchange units. The results obtained in this parameter study agree with earlier obtained numerical results. This indicates that results from the developed numerical code are reliable.

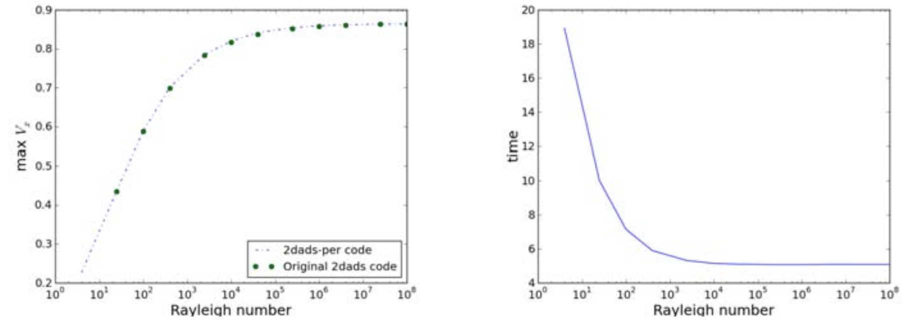

(a) $\max(V_{\mathrm{X}})$ scaling with Rayleigh number (b) $t(V_{\mathrm{X}} = \max(V_{\mathrm{X}}))$ scaling with Rayleigh number

Figure 30: Scaling of $\max(V_{\mathrm{X}})$ and $t(V_{\mathrm{X}} = \max(V_{\mathrm{X}}))$ with increasing Rayleigh number

5 Sheath dissipation effects

Here we study the effects of the parallel sheath current on the blob dynamics. Our interest is a quantitative figure of the blob dynamics and velocity scaling with the sheath dissipation parameter. We introduce the sheath dissipation term on the right hand side of the model equations as discussed in Sec. 2.6.4. The most obvious effect this parameter has on blob dynamics, is the dampening of long wavelengths. Neglecting the non-linear terms of Eqn. (47), its Fourier transformation reads:

$$\frac{\partial \hat{\Omega}_{\mathbf{k}}}{\partial t} = -k_y \hat{\theta}_{\mathbf{k}} - \mu k_\perp^2 - \frac{\sigma}{k_\perp^2} \hat{\Omega}_{\mathbf{k}}.$$

This shows that the time evolution of long wavelength terms are attenuated. Equivalent to this is a attenuation of large scales structures on blob dynamics. The strength with which long wavelengths are damped increases with increasing sheath dissipation parameter.
First in this section, we present a convergence scan for blob simulations with sheath dissipation for the linear model. We proceed by discussing the simulation results, focusing on blob evolution and radial COM dynamics of the blob. We then present results for a scaling analysis for the observed parameters with σ and Ra . A physical interpretation of the results is presented in Sec. 8.4.

5.1 Convergence test

Dampening of large length scales causes the electrostatic potential ϕ to decay strongly in magnitude towards the simulation domain boundaries. Its length scale is now given by the blob size and not the initial size. This allows the domains we test for convergence on to be much smaller than in the previous sections. It also decreases the demands on the number of modes we have to use to achieve convergence. Tab. 11 lists the simulation parameters we test for convergence. Since the dampening of long wavelengths in the system increases with increasing sheath dissipation parameter, we extrapolate the found simulation parameters for a converged simulation to the next value of σ we tested for convergence. For a given Rayleigh number, we use the simulation parameters we determined for $\sigma = 0.01$ for simulations with $0.1 \geq \sigma < 0.1$, the simulation parameters determined for $\sigma = 0.1$ for all simulations with $0.1 \geq \sigma < 1.0$ and so on.

run #	Ra	σ	Domain size	Resolution
1 a/b/c	10^2 /10^4 /10^6	0.01 /1	30×30	512×512
2 a/b/c	10^2 /10^4 /10^6	0.1 /1	50×50	512×512
3 a/b/c	10^2 /10^4 /10^6	1.0 /1	30×30	768×768
4 a/b/c	10^2 /10^4 /10^6	10.0 /1	30×30	1024×1024

Table 11: Convergence test for sheath dissipation. All runs have $t_{\text{end}} = 10$.

Convergence for $\mathrm{Ra} = 10^2$ Analyzing the domain variation we find, that already for a sheath dissipation parameter of $\sigma = 0.1$, the electrostatic potential has vanished at the boundaries of the simulation domain on a 30×30 domain. Consequently, a lower resolution than in simulations without sheath dissipation is sufficient for convergence. The COM velocity curves for resolutions 512×512, 768×768 and 1024×1024 modes resolution are presented in fig.(31(b)). No significant difference is recognizable, the surface plots for all three simulation also show no signs of artifacts from insufficient resolution. For Rayleigh numbers $\mathrm{Ra} = 10^2$ we use a resolution of 1024×1024 modes on a 100×100 domain for all values of $\sigma < 0.1$ and a resolution of 768×768 modes on a 30×30 domain for all values of $\sigma \geq 0.1$.

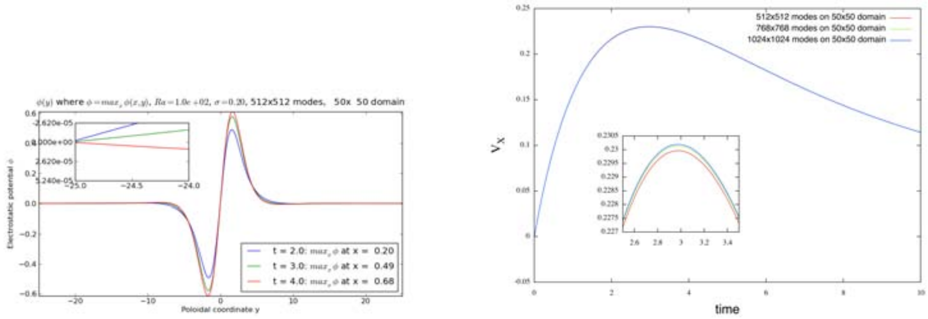

(a) Decay of the electrostatic potential ϕ. (b) Convergence for number of modes, $\max(V_\mathrm{X})$ is marked with a vertical line.

Figure 31: Decay of ϕ and convergence with respect to number of modes for $\mathrm{Ra} = 10^2$, $\sigma = 10$

.

Convergence for $\mathrm{Ra} = 10^4$ **and** $\mathrm{Ra} = 10^6$ Increasing the Rayleigh number does not affect the spatial scales of the potential as discussed before. We find the same convergence behavior with respect to domain size for all higher Rayleigh numbers. Convergence with respect to number of modes is shown in Fig. 5.1. We use a resolution of 2048×2048 modes on a 100×100 domain for $\sigma < 0.1$ and a resolution of 1024×1024 on a 30×30 domain for $\sigma \leq 0.1$.

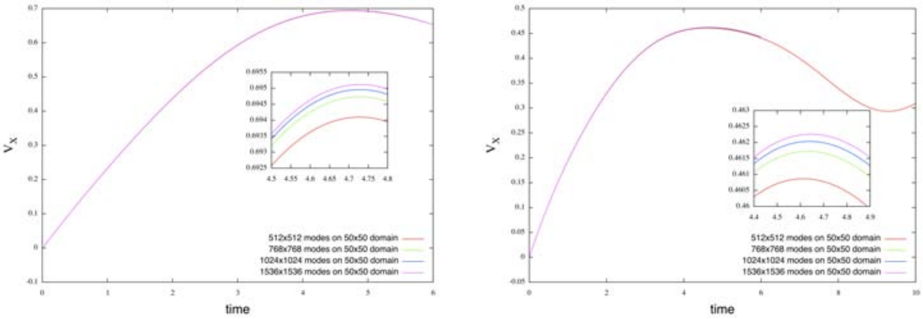

(a) Convergence for $\mathrm{Ra} = 10^4$, $\sigma = 0.2$ (b) Convergence for $\mathrm{Ra} = 10^6$, $\sigma = 0.2$

Figure 32: Convergence for radial COM velocity with number of modes.

5.2 Sheath dissipation parameter scan

We proceed by analyzing blob dynamics with varying the sheath dissipation parameter σ for a fixed Rayleigh number and unity Prandtl number. We use the determined resolution from the convergence studies and vary σ for different Rayleigh numbers, as shown in tab.(5.2). Solutions of the two field model are written out every 0.5 time units, diagnostic output is written out every 0.01 time units. A uniform time step of $\Delta t = 10^{-3}$ was used for all simulations.

Run	Ra	σ	t_{end}
1 / 11 / 21	10^2 /10^4 /10^6	1×10^{-2}	30
2 / 12 / 22	10^2 /10^4 /10^6	2×10^{-2}	30
3 / 13 / 23	10^2 /10^4 /10^6	5×10^{-2}	30
4 / 14 / 24	10^2 /10^4 /10^6	1×10^{-1}	30
5 / 15 / 25	10^2 /10^4 /10^6	2×10^{-1}	30
6 / 16 / 26	10^2 /10^4 /10^6	5×10^{-1}	30
7 / 17 / 27	10^2 /10^4 /10^6	1×10^{0}	30
8 / 18 / 28	10^2 /10^4 /10^6	2×10^{0}	30
9 / 19 / 29	10^2 /10^4 /10^6	5×10^{0}	30
10 / 20 / 30	10^2 /10^4 /10^6	10×10^{1}	30

Table 12: Sheath dissipation parameter scan in σ

Discussion, $\sigma = 0.1$ In Fig. 33 we present simulations with a sheath dissipation coefficient $\sigma = 0.1$ for $\mathrm{Ra} = 10^2$ and $\mathrm{Ra} = 10^6$. Blobs with a small Rayleigh number and low sheath dissipation parameter show a pronounced diffusive behavior. They move radially outwards with a low velocity and bend only slightly into the characteristic mushroom shape. For medium Rayleigh number the mushroom shape evolves clearly. The structure is elongated in the radial direction and the front is unstable to the Rayleigh Taylor mode. We see the formation of a secondary blob structure that disconnects from the front region of the initial blob. The curling of the arms is strongly dampened as they are transported vertically outwards. For large Rayleigh numbers we see an increased curling behavior of the arms compared to medium Rayleigh numbers. At the front we observe a cascade of secondary blob emissions due to Rayleigh Taylor instabilities. Due to small scale flows, the blob structures show large dispersion in the radial direction.

Additionally, we see that the electrostatic potential has local extrema both, at the primary and the secondary blob structure. Plasma is coherently transported along the radial direction within the blob structure along the potential lines.

In Fig. 34 we compare the center of mass coordinates between all three simulations. At low Rayleigh number there is a distinct peak velocity followed by a monotonous deceleration phase. Simulations with medium Rayleigh numbers show the same behavior, but also feature additional acceleration phases after the deceleration, after $t \approx 12$. Emissions of secondary blobs from the unstable blob front cause the variations with multiple peaks. Emissions of these blobs are shown in Fig. 33(b).

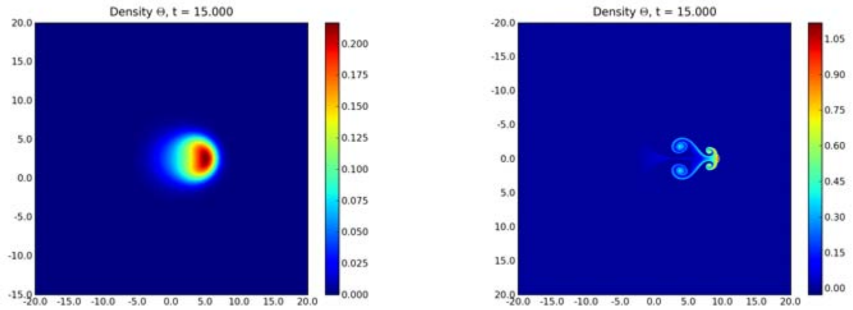

(a) Particle density $\mathrm{Ra} = 10^2$, $t = 15.0$

(b) Particle density $\mathrm{Ra} = 10^6$, $t = 15.0$

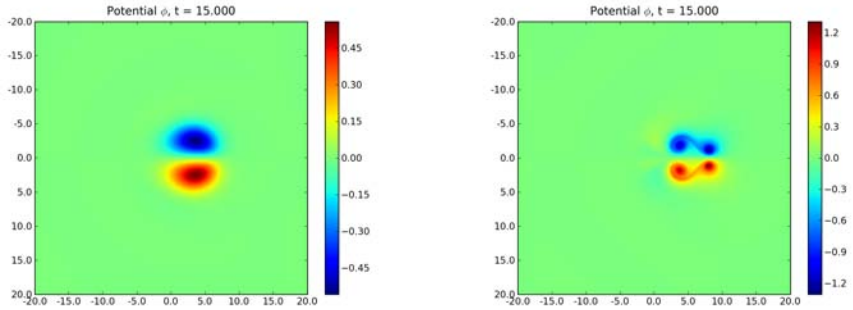

(c) Electrostatic potential $\mathrm{Ra} = 10^2$, $t = 15.0$

(d) Electrostatic potential $\mathrm{Ra} = 10^6$, $t = 15.0$

Figure 33: Particle density and electrostatic potential profiles with sheath dissipation parameter $\sigma = 0.1$. The simulation with $\mathrm{Ra} = 10^2$ shows little blob movement, the simulation with $\mathrm{Ra} = 10^6$ has emitted a secondary blob structure at the front.

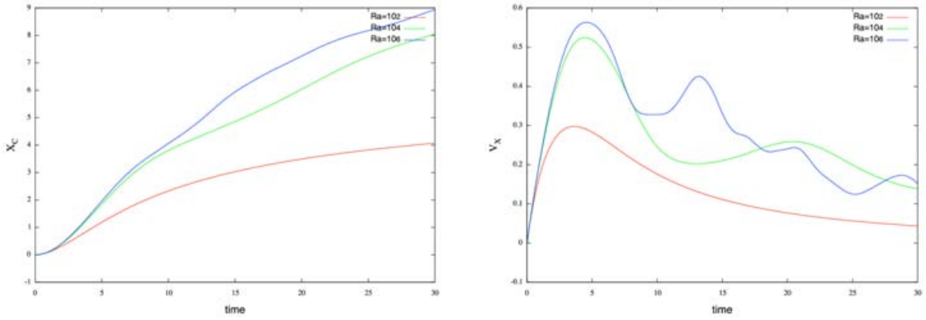

(a) COM position

(b) COM velocity

Figure 34: Center of mass coordinates for simulations with $\sigma = 0.1$

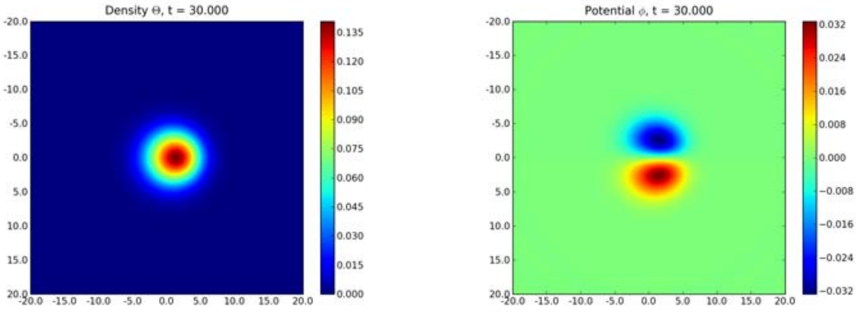

(a) Particle density n, Ra = 10^2, $t = 30.0$ (b) Electrostatic potential ϕ, Ra = 10^2, $t = 30.0$

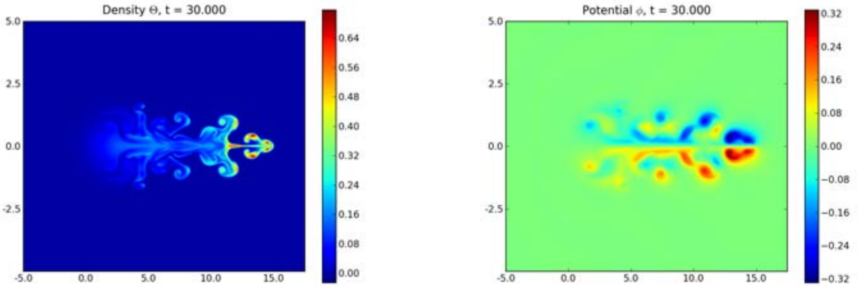

(c) Particle density n, Ra = 10^6, $t = 30.0$ (d) Electrostatic potential ϕ, Ra = 10^6, $t = 30.0$

Figure 35: Blob evolution for $\sigma = 1.0$, Ra = 10^2 and Ra = 10^6.

Discussion, $\sigma = 1.0$ Intermediate sheath dissipation parameters have significant influences on blob evolution. In Fig. 35 we present the particle density for Ra = 10^2 and Ra = 10^6 to demonstrate the effect of sheath connected currents on the blob evolution.

For small Rayleigh number we observe that the blob shows a dominant diffusive behaviour. Its diameter has nearly doubled and the peak amplitude has decayed from 1.0 at $t = 0$ to $\max(\theta) \approx 0.135$ at $t = 30.0$. The blob presents no significant radial elongation and keeps its initial radial shape for 30 ideal interchange time units, shown in Fig. 35(a).

For intermediate Rayleigh numbers we see a strong dampening of dissipation along the poloidal direction. Lobes that were observed in previous simulations for Ra = 10^4 do not emerge from the initial gaussian structure and the diffusion in the poloidal direction is weak. We observe a strong horizontal elongation of the blob structure. For large Rayleigh numbers, the simulations show a blob structure that shows pronounced radial dispersion. Lobes form along the poloidal direction, but are not transported outwards, due to attenuated large scale transport, as it happens without sheath dissipation. The front of the blob develops a typical mushroom shape and is hastily transported radially outwards. A cascade of Rayleigh Taylor instabilities lead to the development of several secondary plasma blobs that eject themselves from the front of the mushroom.

In Fig. 36 we present the center of mass coordinates for different Rayleigh numbers with $\sigma = 1.0$. The small Rayleigh number simulation features a distinct peak velocity in the initial motion and a monotonic deceleration afterwards. Sheath dissipation has a strong influence on the blob velocity, its peak velocity has decreased from approximately $\max(V_\mathrm{X}) \approx 0.6$ at $t \approx 7.5$ without sheath dissipation, to $\max(V_\mathrm{X}) \approx 0.1$ at $t \approx 1.5$ with $\sigma = 1.0$, compared to Fig. 21.

The medium Rayleigh number features a velocity plateau from $t \approx 4 - 8$ ideal interchange times. In this phase the blob front travels outwards faster than the surrounding of the blob, ejecting itself from the bulk plasma. This behavior can be interpreted as a Rayleigh-Taylor instability where the formation of a blob is enhanced and the bulk plasma is accelerated outwards. This accelerated plasma leaves behind a particle density tail that moves at a low velocity, further elongating the plasma filament. In Fig. 37 we present the evolution of the cross section of particle density and radial drift velocity at the symmetry axis $y = 0$. For $t = 10.0$ the velocity profile has two peaks. At $x = 2$ the velocity peak is stationary while the peak at $x = 4$ is moving radially outwards. It grows in amplitude and comes to a stop at $t = 20$. It extends in spatial extension and at $t = 30$ we see that it splits up, with another peak moving radially outwards. The particle density profile develops accordingly. We see an increased density to the right of the velocity peaks.
This form of behavior can also be found in Fig. 35(c). In this simulation the blob structure has been subject to multiple emissions of secondary blobs from the blob front.

Simulations with a large Rayleigh number show a velocity curve with more peaks after the initial peak.
We see the same characteristic behavior as for $\mathrm{Ra} = 10^4$, with increased occurrence of blob emissions from the structures front. The velocity curve evolution is comparable to the curves with lower Rayleigh number, instabilities begin to occur at $t \approx 5.0$. After this time, we observe that the front is subject to a cascade of Rayleigh Taylor instabilities. Due to small collisional diffusion and viscosity, lobes form in the regions where secondary blobs left the bulk plasma.

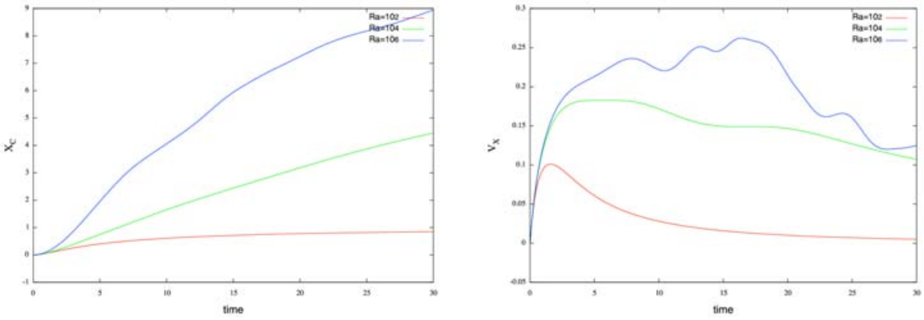

(a) Radial COM position (b) Radial COM velocity

Figure 36: Center of mass coordinates for simulations with $\sigma = 1.0$.

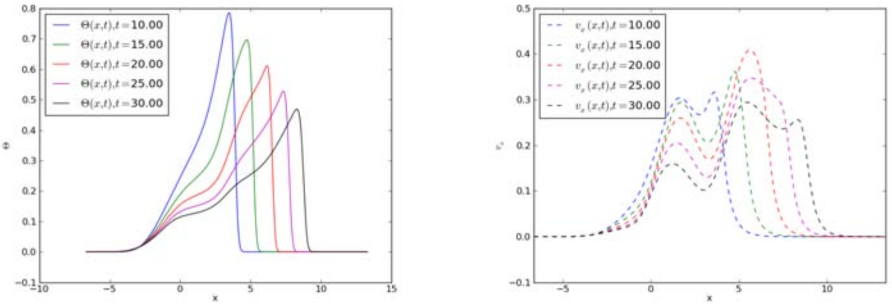

(a) Particle density (b) Radial $E \times B$ velocity

Figure 37: Evolution of profiles at the symmetry axis $y = 0$ for $\mathrm{Ra} = 10^4$ and $\sigma = 0.1$

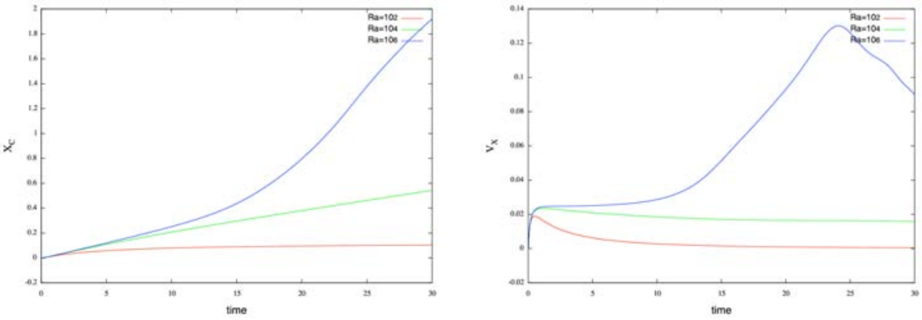

(a) COM position (b) COM velocity

Figure 38: Center of mass coordinates for simulations with $\sigma = 10.0$

Discussion, $\sigma = 10.0$ The effect of large sheath dissipation on radial blob dynamics is shown in Fig. 38. For all Rayleigh numbers, the radial motion almost comes to a full stop. Blob movement in this regime features a short initial acceleration phase, where the blobs reach only low velocities.
For $\mathrm{Ra} = 10^2$, the blob decelerates to a full stop, whereas for $\mathrm{Ra} = 10^4$, the blob decelerates only little after reaching its peak velocity of $\max(V_\mathrm{X}) \approx 0.02$ at $t \approx 1.2$.

Large Rayleigh number simulations show the same initial acceleration phase. After the blob velocity stagnates at a plateau from $t \approx 2.0 - 5.0$, we see a large increase in V_X . The surface plots of the blob evolution in Fig. 39 show that the blob does not move as a bulk structure, but rather a tilting of the particle density maximum outwards. This tilting is elucidated by Fig. 40. The figures for $t = 10$ show a that the particle density builds a steep front with the maximum radial velocity being behind this front. The electrostatic potential in Fig. 39(b) also shows that plasma is transported along the center $y = 0$ towards the front of the blob. The front becomes unstable to the Rayleigh-Taylor instability and detaches from the original

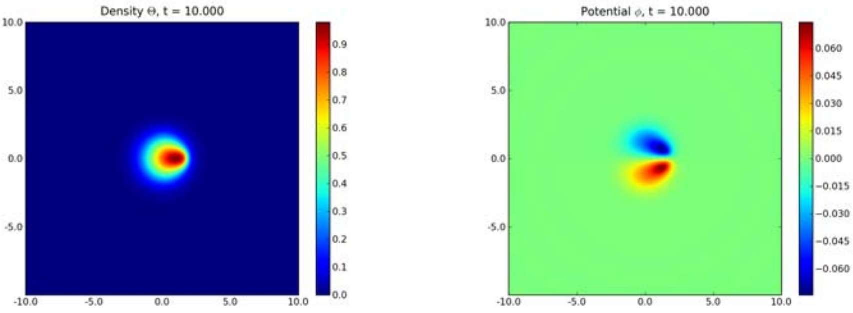

(a) Particle density, $t = 10.0$ (b) Electrostatic potential, $t = 10.0$

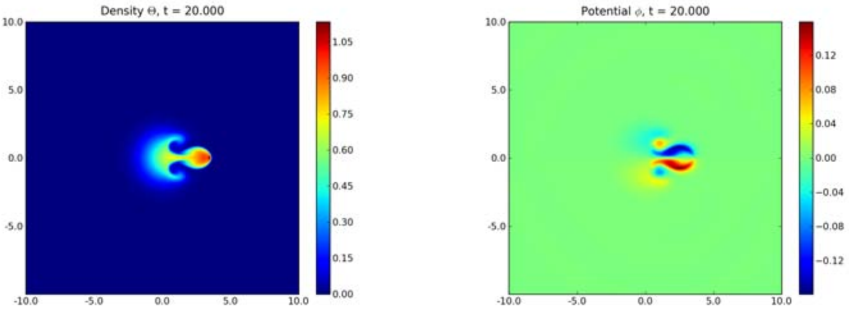

(c) Particle density, $t = 20.0$ (d) Electrostatic potential, $t = 20.0$

Figure 39: Particle density and electrostatic potential for $\mathrm{Ra} = 10^6$ and $\sigma = 10.0$.

blob, which rests at its initial position, as shown in Fig. 39(c). The radial velocity at $y = 0$ is maximal at $x \approx 2$ for $t = 20$, plasma particles are transported from the original blob to the secondary blob front.
The further evolution of the blob is shows a cascade of secondary blobs being emitted from the front. At $t = 30$ we see multiple local particle density maxima in Fig. 40(a). The particel density at the origin has decayed to less than half its initial value, while the particle density at the front of the structure is larger than the initial particle density maximum. The radial velocity cross section in Fig. 40(b) shows multiple velocity peaks.

All simulations with $\sigma = 10$ have shown the strong dampening, coherent plasma structures experience in their radial motion due to sheath currents. They act as a sink for the kinetic energy in the simulation domain.

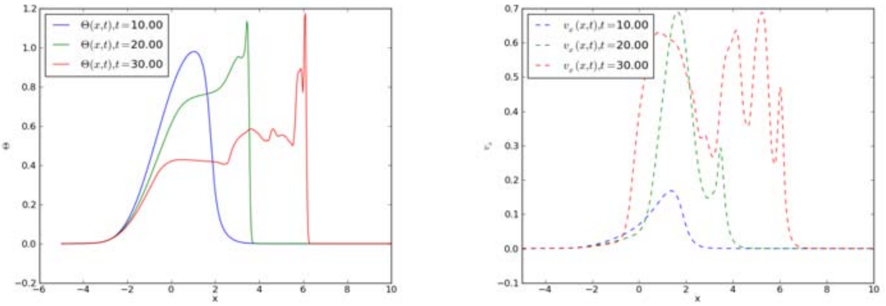

(a) Particle density cross sections

(b) Radial $E \times B$ velocity

Figure 40: Evolution of profiles at the symmetry axis $y = 0$ for $\mathrm{Ra} = 10^6$ and $\sigma = 10$

5.3 Scaling behavior

In Fig. 5.3 we present the COM velocity curves for all simulations in Tab. 5.2. We clearly see the dissipative effect parallel currents have on the blobs initial dynamics. Both, $\max(V_\mathrm{X})$ and the length of the initial acceleration phase decrease significantly with increasing sheath dissipation parameter. This effect is most pronounced for simulations with $\mathrm{Ra} \ = 10^2$ and diminishes with increasing Rayleigh number.

To quantify the effect of σ on $\max(V_\mathrm{X})$ and $t(V_\mathrm{X} = \max(V_\mathrm{X}))$, we first present the method, how we define $\max(V_\mathrm{X})$. Simulations for $\mathrm{Ra} \ = 10^4$ and $\sigma \geq 1$, as well as simulations for $\mathrm{Ra} \ = 10^6$ and $\sigma \geq 0.5$ do not present a pronounced maximum velocity. Instead they present intervalls, where blob acceleration stagnates. These intervalls are due to the radial elongation the blobs showed in simulations. We are interested in $\max(V_\mathrm{X})$ in the phase of blob evolution, where the blob shows a strongly localized structure.

To do so, we define a cutoff parameter for the COM curves, $t_{\max} = min_{t_i}\{t_i \mathrm{where} V_\mathrm{X}{}'(t_i) = \min\}$. That is, we determine the time, where the derivative of V_X is minimal. This assumes that there is an inflection point in the V_X curve, before blob dynamics are dominated by instabilities. We identify $\max(V_\mathrm{X})$ then in the interval $[0 : t_{\max}]$. The cutoff parameters are shown for simulations with all Rayleigh numbers and $\sigma \geq 0.5$ in Fig. 45. This method yields acceptable cutoff times, still for some simulations a cutoff was set manually. All simulations with $\sigma \leq 0.2$ present a clear maximum. Here we determined $\max(V_\mathrm{X})$ over the whole V_X curve. The error we include with this method is small, $\max(V_\mathrm{X})$ varies little over the phase, where the blob acceleration stagnates.

The result of the analysis for the simulation from Tab. 5.2 is presented in Fig. 42. We find that for $\sigma \geq 0.5$, $\max(V_\mathrm{X})\ (\sigma)$ is suitable described with a power law:

$$\max(V_\mathrm{X})\ (\sigma) = \alpha\sigma^{\beta} \tag{74}$$

, with $\beta \leq 0$. The results of a least squres fit for $\max(V_\mathrm{X})$ on $\sigma = [0.5 : 10]$ are presented in Fig. 42(a). The obtained results from the fit are almost exact. We find that for an increasing Rayleigh number, the exponent β approaches negative one, while the linear factor

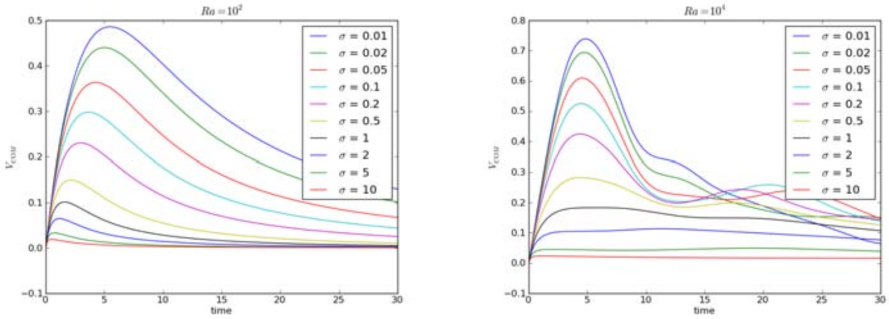

(a) Ra $= 10^2$

(b) Ra $= 10^4$

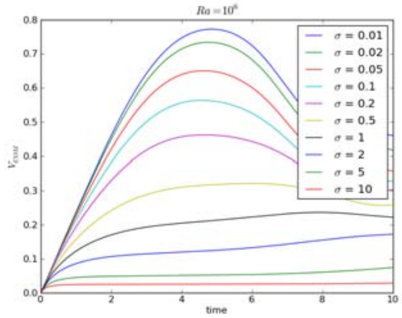

(c) Ra $= 10^6$

Figure 41: Radial COM velocities for varying sheath dissipation parameter σ

α approaches 0.2.

An analysis of the initial acceleration phase of the blob with increasing sheath dissipation coefficient reveals a similar behavior. Here, the problems with determining $t(V_{\mathrm{X}} = \max(V_{\mathrm{X}}))$ is more significant than for determining $\max(V_{\mathrm{X}})$. The large time intervalls over which radial blob velocity stagnates do not allow a proper determination of $t(V_{\mathrm{X}} = \max(V_{\mathrm{X}}))$. Due to this large error, we choose not to quantify the functional relation $t(V_{\mathrm{X}} = \max(V_{\mathrm{X}}))\ (\sigma)$. From Fig. 42(b) we see, that a power law as in Eqn. (74) is a good assumption.

To further elucidate the behavior with of $\max(V_{\mathrm{X}})$ for large σ, we run simulations with Ra $= 4\times10^4$, Ra $= 2.5\times10^5$ and Ra $= 10^8$ and unit Prandtl number for $\sigma = 0.5, 1.0, 2.0, 5.0$ and 10.0. Simulation parameters are the same as for run # 26 – # 30 from Tab. 5.2. Determining $\max(V_{\mathrm{X}})$ and $t(V_{\mathrm{X}} = \max(V_{\mathrm{X}}))$ is done with the same procedure as for simulations with Ra $= 10^2$, Ra $= 10^4$ and Ra $= 10^6$. The position of $t_{\max}$ is marked with a black circle in Fig. 45.

We find similar decrease in $\max(V_{\mathrm{X}})$ with increasing σ, as shown in Fig. 42(a), radial blob dynamics are damped increasingly, with increasing σ.

We now study the effect the sheath dissipation parameter σ has on blob dynamics in different regimes of Rayleigh numbers. The maximal radial COM velocity dependent on the Rayleigh

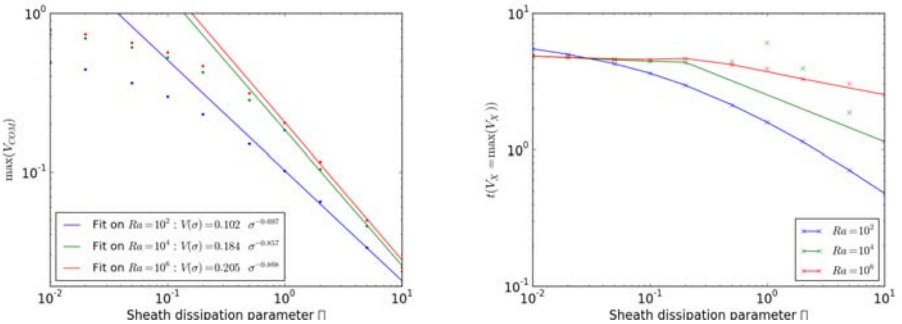

(a) Scaling of $\max(V_\mathrm{X})$ with increasing sheath dissipation parameter

(b) Scaling of $t(V_\mathrm{X} = \max(V_\mathrm{X}))$ with increasing sheath dissipation parameter

Figure 42: Radial COM velocity scaling properties with sheath dissipation coefficient.

number is presented for different sheath dissipation parameters in Fig. 43. We find, that the Rayleigh number gives a significant variation of $\max(V_\mathrm{X})$ for $\sigma = 0.5$, whereas for large values of σ, the influence of Ra on $\max(V_\mathrm{X})$ is negligible. For all values of σ we find that the maximum velocity becomes independent of Ra and approaches a theoretical maximum that is a function of σ.

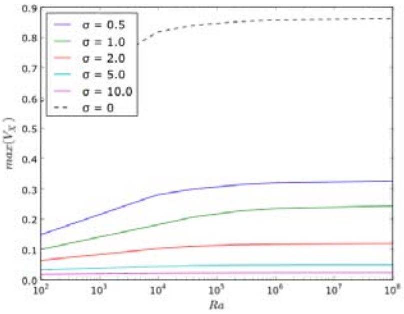

Figure 43: Scaling of $\max(V_\mathrm{X})$ with Rayleigh number for different values of σ.

This trend can also be observed in the decay of $\max(V_\mathrm{X})$ with increasing σ for a fixed Rayleigh number. Least squares fits for $\max(V_\mathrm{X})$ on the interval $\sigma = [1 : 10]$ for Ra $= 4 \times 10^4, 2.5 \times 10^5$ are executed and the obtained fit parameters are almost exact. In Fig. 44 we present the found fit parameters for Ra $= 10^2, 10^4, 4 \times 10^4, 2.5 \times 10^4$ and 10^6. We find that the fit coefficient α asymptotically approaches a numerical value of $\alpha_0 \approx 0.24$ from below for Ra $\to \infty$. The fit exponent β shows a decays to a value of $\beta_0 \approx -1.0$ for Ra $\to \infty$.

The scaling found is similar to the scaling presented in Fig. 30, in the sense, that a parameter converges to a limit for increasing Rayleigh number.

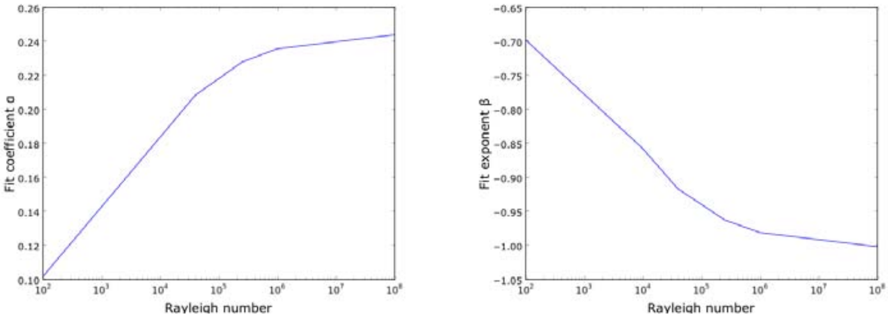

(a) Coefficient α

(b) Exponent β

Figure 44: Variation of fit parameters of Eqn. (74) with Rayleigh number.

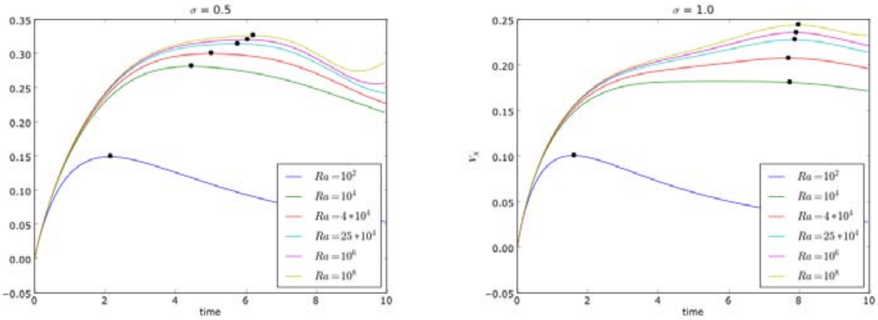

(a) V_{X} for different Rayleigh numbers and $\sigma = 0.5$. Cutoff parameter for Ra $= 10^6$ is manually set to $t = 7.0$.

(b) V_{X} for different Rayleigh numbers and $\sigma = 1$. Cutoff parameter for Ra $= 10^4$ is manually set to $t = 7.7$.

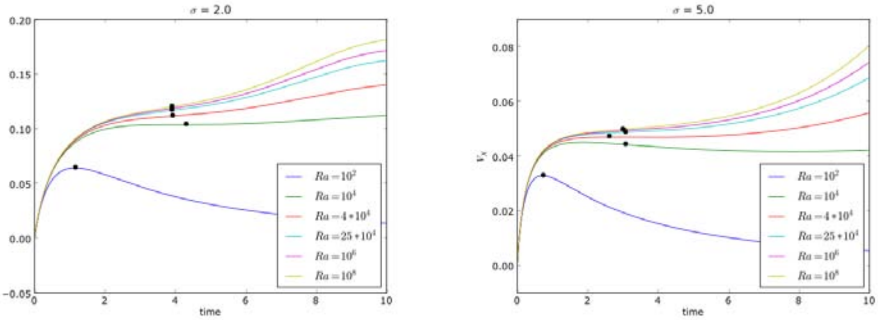

(c) V_{X} for different Rayleigh numbers and $\sigma = 2$. Cutoff parameters for Ra $> 10^4$ are manually set to $t = 4.0$.

(d) V_{X} for different Rayleigh numbers and $\sigma = 5$. Cutoff parameter for Ra $= 10^4$ is set manually to $t = 3.0$

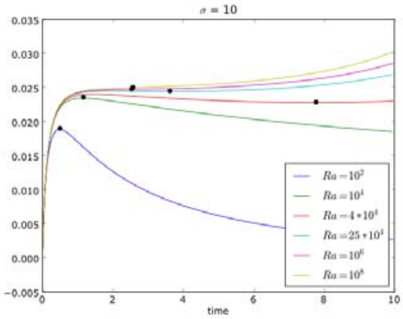

(e) V_{X} for different Rayleigh numbers and $\sigma = 10$

Figure 45: COM velocities used. The position of the cutoff parameter $t_{\max}$ for each curve is marked with a black circle.

6 Simulations with large blob amplitude

We now turn our attention to the non-linearized model from Sec. 2.6.3: We use the term non-linearized, to denote that we did not linearize the interchange term. The model equations are still non-linear themselves.

Again, we simulate the evolution of an initial gaussian particle density profile. For these simulations, we have three free parameters: the relative particle density perturbation amplitude $\hat{\eta}$ and the diffusion coefficients for vorticity μ and particle density, κ. Initial values θ and Ω are provided by:

$$\begin{aligned} \theta(x, y) &= 1 + \hat{\eta}\ \exp\left(-\frac{x^2 + y^2}{2}\right) \\ \Omega(x, y) &= 0. \end{aligned}$$

We study the effects large amplitude has on blob motions and scaling properties of the plasma flux with this parameter. The effects of varying diffusion parameters are thoroughly discussed for the linearized model. In Sec. 6.4 we study the effects of sheath dissipation for large blob amplitude.

In this text we use $\hat{\eta}$ and $\Delta\theta/\Theta$ synonymous for the blob amplitude. As described previously, this model features a non-linear interchange term. This gives a different normalization for the ideal interchange time. The parameters κ and μ, as well as the time units used in simulations are not directly comparable between the models. When we denote the time used in the non-linearized model with t_{nl} and the diffusion coefficients used in the non-linearized model with κ and μ, we find the corresponding quantities t_l, κ' and μ' of the linearized model via:

$$\begin{aligned} t_l &= t_{nl} \times \sqrt{\hat{\eta}}\,, \\ \kappa' &= \kappa/\sqrt{\hat{\eta}}\,, \\ \mu' &= \mu/\sqrt{\hat{\eta}}\,. \end{aligned} \tag{75}$$

From the discussion in Sec. 3.6 we take, that the radial center of mass velocity, V_X is directly comparable between the models, since we remove the background particle density when computing V_X for the non-linearized model. Note that plots presenting simulation results from both models simultaneously, the results are subject to a different normalization and are not to compare directly.

6.1 Convergence study

Convergence tests for this model follow the outline presented in the previous sections. For a fixed characteristic particle density perturbation $\hat{\eta}$, we increase the simulation domain until finite size effects on the electrostatic potential are negligible. We then proceed by increasing the number of spectral modes, until the changes in the COM velocity curve are insignificant

and no evidence of an under-resolved simulation are visible in the particle density field and its cross section at $y = 0$.
From the parameter scan in Sec. 4 we remember that an increasing Rayleigh number increases the demands for the number of modes. The discussion above shows, that increasing the particle density perturbation amplitude for the non-linearized model implies increasing the Rayleigh number for the linearized model. Simulations with increasing values of $\hat{\eta}$ increases demand on computational cost in the same sense as it increases with increasing Rayleigh number. We test convergence for simulations with $\hat{\eta} = 0.1, 1.0$ and 10.0. Simulations with intermediate values of $\hat{\eta}$ are run with parameters that yield a converged simulation for the next larger value of $\hat{\eta}$ we have tested convergence for.
Previous convergence runs were run until $t_{\text{end}} = 8.0$, translated values of t_{end} for the non-linearized model are 25.0, 8.0 and 2.6 for $\hat{\eta} = 0.1, 1.0, 10.0$. We have chosen longer simulation times to study convergence in the regime when the blob structure has strongly dispersed.
In Tab. 13 we present the simulation parameters that are tested for convergence in the sense described above. Simulation parameters that have converged with respect to resolution and domain size are denoted with a $\surd$.

$\hat{\eta}$	Domain size	Resolution	t_{end}	Converged
0.1 / 1.0 / 10.0	200 × 200	512 × 512	30.0 / 10.0 / 10.0	- / - / -
0.1 / 1.0 / 10.0	200 × 200	768 × 768	30.0 / 10.0 / 10.0	- / - / -
0.1 / 1.0 / 10.0	100 × 100	1024 × 1024	30.0 / 10.0 / 10.0	- / - / -
0.1 / 1.0 / 10.0	100 × 100	1536 × 1536	30.0 / 10.0 / 10.0	$\surd$ / - / -
0.1 / 1.0 / 10.0	100 × 100	2048 × 2048	30.0 / 10.0 / 10.0	$\surd$ / - / -
1.0 / 10.0	100 × 100	2560 × 2560	10.0 / 10.0	$\surd$ / -
10.0	100 × 100	3072 × 3072	10.0	$\surd$
10.0	100 × 100	4096 × 4096	10.0	$\surd$

Table 13: Convergence scan for non-linearized model. All simulations are run with $\kappa = \mu = 10^{-3}$ and a time step of $\Delta_t = 10^{-3}$.

In Fig. 46 we show the cross-section of the electrostatic potential at the radial coordinate where $\phi = \max \phi$ for $\hat{\eta} = 10.0$. The finite size effects are visible for the smaller simulation domain. On a 200 × 200 domain, the electrostatic potential has decayed to $\phi \approx \pm 0.15$ at $y = \pm 50$, or ca. 0.1 % of its maximum at $t = 3.0$ and has a gradient of $\phi_y \approx \pm 0.007$. Choosing a domain size of 100 × 100 yields a gradient of $\phi_y \approx \pm 0.013$ at $y = \pm 50$. With this domain size, finite size effects are larger than in simulations for the linearized model. On the other hand, rises the computational demand with the simulation domain size, that renders larger box sizes unfavorable.

We now determine the number of modes which give converged simulations. In fig.(47) we present the radial COM velocity curves from the convergence scan and surface plots for θ. The curves for V_X show good convergence and the presented surface plots do not exhibit any signs of insufficient resolution.

The simulation results show convergence for $\hat{\eta} \leq 0.1$ for a resolution of 1536 × 1536 on a

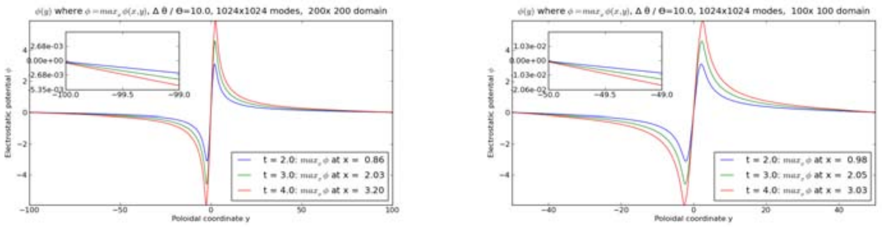

(a) Simulation domain 200 × 200

(b) Simulation domain 100 × 100

Figure 46: Decay of electrostatic potential ϕ for $\hat{\eta} = 10$

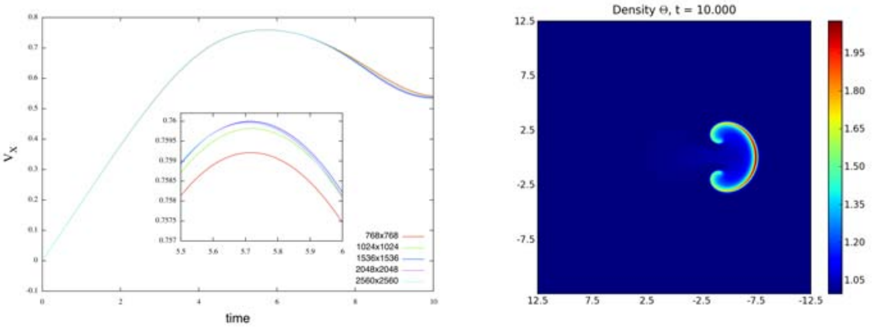

(a) Radial COM velocity for increasing number of modes on a 100 × 100 domain, $\hat{\eta} = 1.0$.

(b) Particle density θ for $\hat{\eta} = 1.0$, $t = 10.0$ 2560 × 2560 modes on a 100 × 100 domain.

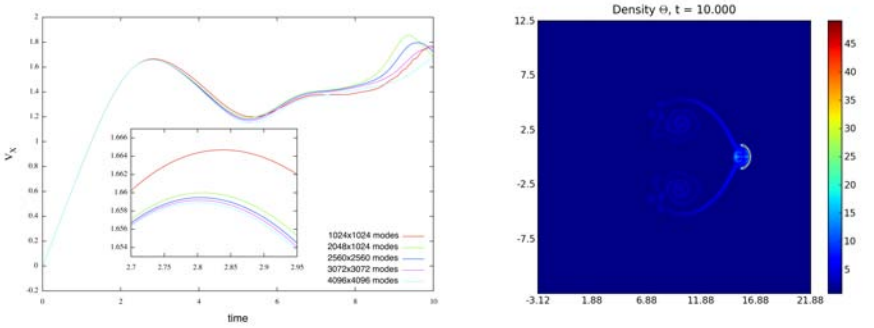

(c) Radial COM velocity for increasing number of modes on a 100 × 100 domain, $\hat{\eta} = 10.0$.

(d) Particle density θ for $\hat{\eta} = 10.0$, $t = 10.0$ 3072 × 3072 modes on a 100 × 100 domain.

Figure 47: Results for convergence test for number of modes for the non-linearized model.

100 × 100 grid. An increased amplitude of $\hat{\eta} = 1.0$ requires 2560 × 2560 modes resolution, and 3072 × 3072 modes are required to converge simulations with $1.0 < \hat{\eta} \leq 10.0$, both on a 100 × 100 grid. From Fig. 46 see that a large blob amplitude has only a small effect on the spatial extension of the electrostatic potential ϕ. It extends over the same spatial scales we found in convergence studies for the linearized model.

Run nr.	$\hat{\eta}$	t_{end}	$\max(V_{\text{X}})$	$t(V_{\text{X}} = \max(V_{\text{X}}))$
# 1	0.01	75.0	0.081880637	51.42
# 2	0.02	75.0	0.11721187	36.18
# 3	0.05	75.0	0.18684137	22.89
# 4	0.10	45.0	0.26399755	16.29
# 5	0.20	30.0	0.36993963	11.67
# 6	0.50	20.0	0.56511486	7.66
# 7	1.00	20.0	0.75994992	5.71
# 8	2.00	15.0	0.9947924	4.38
# 9	10.0	10.0	1.658917	2.80
#10	20.0	5.0	1.9743165	2.47
#11	50.0	5.0	2.399163	2.18
#12	100	5.0	2.7202127	2.03
#13	200	5.0	3.0378931	1.92
#13	500	5.0	3.4505634	1.80
#14	1000	5.0	3.7565880	1.74
#15	2000	5.0	4.0571766	1.68
#16	5000	5.0	4.4464970	1.63

Table 14: Relative amplitudes and simulation end times for non-linearized model simulations. All simulations are run with $\kappa = \mu = 10^{-3}$.

6.2 Variation of relative amplitude

We begin by studying the effects a varying amplitude has on blob movements. All simulations are run with $\kappa = \mu = 10^{-3}$ and a time step of $\Delta_t = 10^{-3}$. Diagnostic output is written out every 0.01 time units, full output every 0.5 time units. Resolution and domain sizes determined in the previous section are used for the simulations. In Tab. 14 we list the simulations executed and the time of the peak velocity. The end times of simulations #1 to #10 are chosen, so that they roughly correspond to 15 ideal interchange times for the linearized model. Simulations #10 to #17 are run with the same simulation parameters as were determined in the convergence test for a characteristic particle density perturbation $\hat{\eta}$ =10. An analysis of cross sections at $y = 0$ and surface plots for θ showed no artefacts indicating an under-resolved simulation.

Discussion for $\hat{\eta} \leq 1.0$. Simulations with a blob amplitude of $\hat{\eta} = 0.01$ present all features that were discussed in the simulation of the linearized model with Ra $= 10^4$ and Pr $= 1$. Surface plots for θ and Ω for the linearized model were presented in Fig. 25. The blob moves radially outward, the front steepens and plasma is transported along the isopotential lines poloidally outwards to form lobes. Vorticity with different sign inherent to the lobes causes a (counter-) clockwise rotation of the (lower) upper lobe. The lobes separate poloidally and the mushroom shape flattens out during the radial outwards movement of the plasma filament. In Fig. 48 we present the COM coordinates and velocities for simulations with $\hat{\eta} \leq 0.05$.

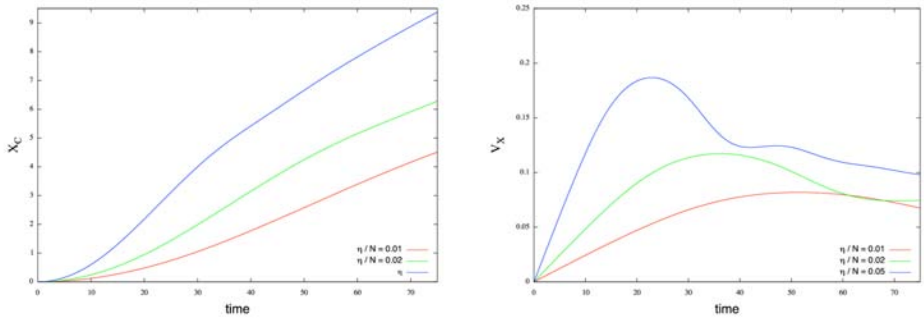

(a) COM position (b) COM velocity

Figure 48: Radial COM coordinate and velocity or $\hat{\eta}$ $= 0.01, 0.02$ and 0.05.

We see a quick rise in $\max(V_\mathrm{X})$ from 0.08 to 0.186 and the time where the blob travels at maximum radial velocity decreases from 51.42 to 22.89 ideal interchange time units when $\hat{\eta}$ increases from 0.01 to 0.05.

As mentioned previously, the simulation parameters $\kappa = \mu = 10^{-3}$ and $\hat{\eta}$ $= 0.01$ translate to $\kappa' = \mu' = 10^{-2}$ for the linearized model. When comparing blob dynamics for these models in Fig. 49, we find that very small values of $\hat{\eta}$ give a slightly decreased blob velocity, compared to a simulation of the linearized model. Increasing $\hat{\eta}$ 0.02, yields simulations, where blobs travel faster than in the simulation with $\mathrm{Ra} = 10^4$ in the linearized model. But $\hat{\eta}$ $= 0.02$ gives also $\mathrm{Ra}' = 2 \times 10^4$ for the linearized model. From previous discussion we know that this yields also a slightly larger maximum radial COM velocity. The reference data used in the plots are from run # 6 of Tab. 10. Overall, we find an excellent agreement between simulation data from both models.

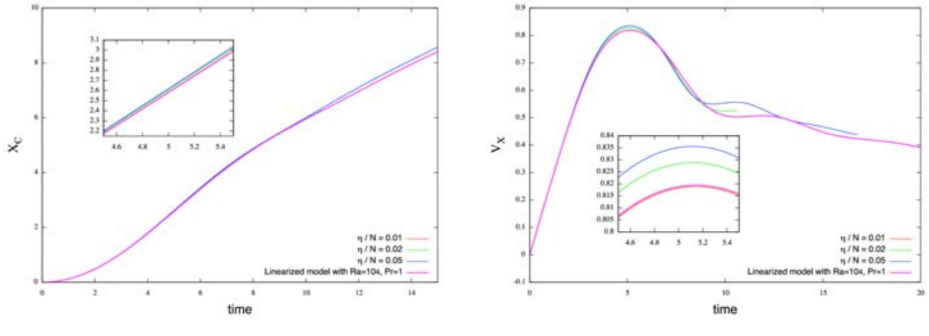

(a) COM position (b) COM velocity

Figure 49: Comparison if simulations from the linearized model to simulations of the non-linearized model with $\hat{\eta}$ ≤ 0.05.Times and velocities are scaled to units of the linearized model.

For a blob amplitude of $\hat{\eta}$ $= 0.1$ we see blob evolution that are similar to the previous simulations. The blob develops a density front on the right side, owed to the location of the velocity peak behind the front. We also see the evolution of the lobes, which roll up in different directions due to opposite sign of vorticity in the arms. Along the arms, a vorticity double layer arises due to vertical particle density gradients. The features of the blob are not different from the features of a blob for a simulation with $\mathrm{Ra} = 10^4$, which were shown in Fig. 25.

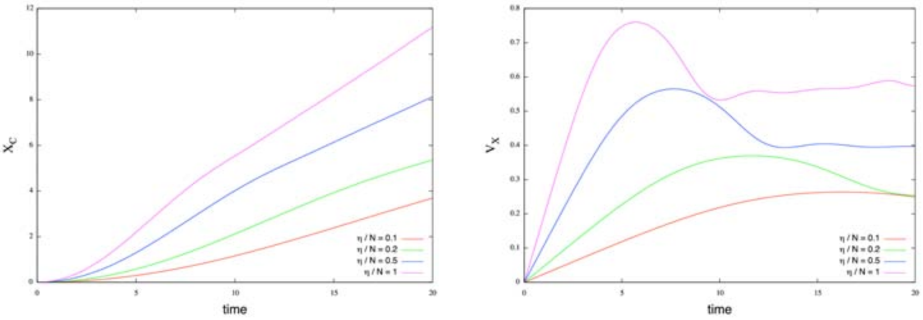

(a) COM coordinate (b) COM velocity

Figure 50: Radial COM coordinates for $\hat{\eta} \leq 1.0$.

Discussion for amplitudes $\hat{\eta} \geq 1.0$ Blob evolution for particle density perturbations $\hat{\eta} = 1.0$ are similar to run #9 in Tab. 10 from Sec. 4.2. Translated to the linear model, the viscosity and diffusion coefficients κ and μ are 10^{-3} in both models. Blob evolution is characterized by a pronounced density front that is unstable to the Rayleigh-Taylor mode at the front, and unstable to the Kelvin-Helmholtz mode at the lobes.

Blob evolution for larger values of $\hat{\eta}$ continues the trend of thinner fronts, larger velocities and earlier occurrence of instability driven behavior. In Fig. 51 we present the full particle density and electrostatic potential for simulation # 9 from Tab. 14, where the blob is subject to both discussed instabilities.

Fig. 52 presents the blob dynamics for large values of $\hat{\eta}$. The maximal radial COM velocity increases with $\hat{\eta}$ due to growing vertical gradients in the particle density for $\hat{\eta}$, yielding stronger interchange motions. For $\hat{\eta} \geq 10$ we find that the late blob evolution after the blob has reached its peak show an increasing COM velocity due to Rayleigh-Taylor instabilities at the blob front.

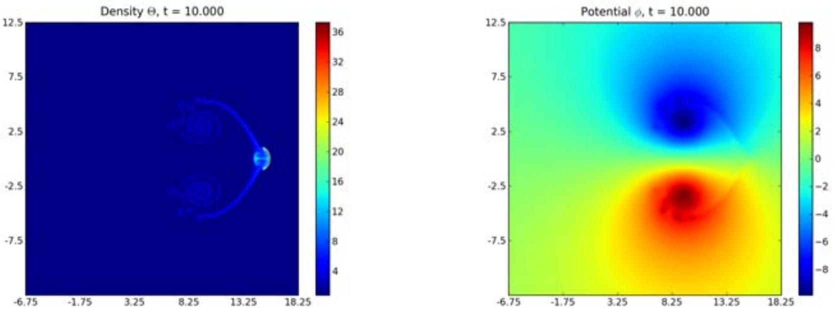

(a) Particle density, θ (b) Electrostatic potential ϕ

Figure 51: Particle density and electrostatic potential for $t = 10.0$ with $\hat{\eta} = 10.0$, $\kappa = \mu = 10^{-3}$.

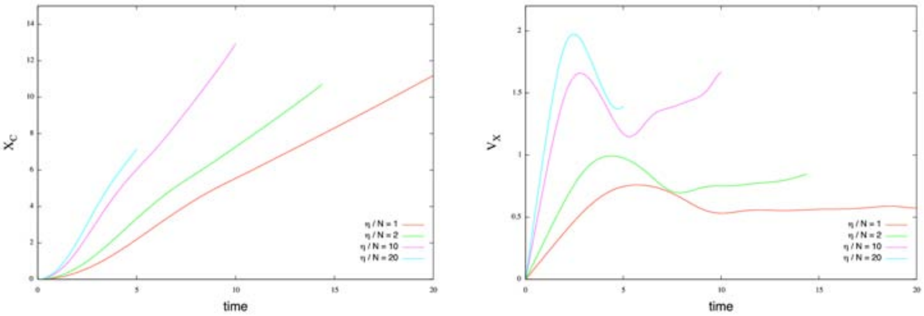

(a) COM coordinate (b) COM velocity

Figure 52: Radial COM coordinates for $\hat{\eta} \leq 20.0$.

6.3 Scaling properties

The discussion above presented that the blob amplitude has a significant influence on the blob dynamics. A comparison of the V_X curves shows, that the radial velocity increases with $\hat{\eta}$. In Fig. 53(a) we present the scaling of the radial COM velocity. The figure suggests a power law relation for both $\max(V_X)$ and $t(V_X = \max(V_X))$:

$$\begin{aligned} \max(V_X) &= \alpha \times \hat{\eta}^{\,\beta} \\ t(V_X = \max(V_X)) &= \epsilon \times \hat{\eta}^{\,\zeta}. \end{aligned}$$

We read from the figure, that there are two regimes where the parameters $\alpha, \beta, \epsilon, \zeta$ will assume different values.

For low values of relative amplitude, $\hat{\eta} \in [0.01 : 0.2]$ we find $\alpha = 0.827$ and $\beta = 0.489$, for $\hat{\eta} \in [50 : 1000]$ we find $\alpha = 1.380$ and $\beta = 0.146$. The residuals squared per number of degrees of freedom for the fits are of order $\mathcal{O}(10^{-6})$, which is practically exact. A larger blob amplitude causes larger vertical particle density gradients and thereby stronger interchange motions. One can speculate, that increasing velocity by this means is less effective for large blob amplitudes.

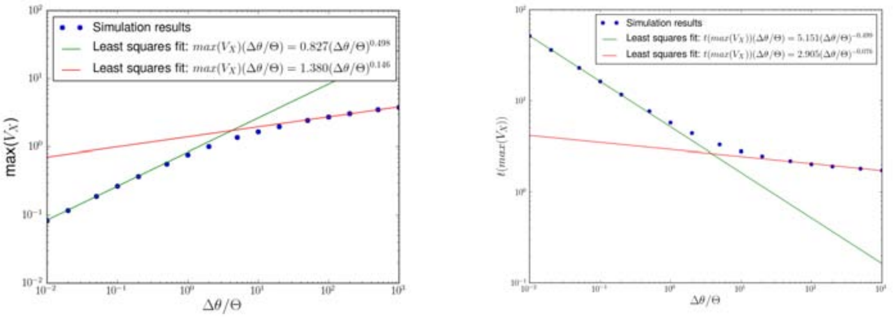

(a) $\max(V_{\mathrm{X}})$ scaling with $\hat{\eta}$

(b) $\max(V_{\mathrm{X}})$ scaling with $\hat{\eta}$

Figure 53: Scaling properties for $\hat{\eta}$

Least squares fit for $t(V_{\mathrm{X}} = \max(V_{\mathrm{X}}))$ yield $\epsilon = 5.151$ and $\zeta = -0.499$ for a fit over $\hat{\eta} \in [0.01 : 0.2]$ and $\epsilon = 2.905$ and $\zeta = 0.076$ for $\hat{\eta} \in [50 : 1000]$. The residuals for this least squares fit are of order $\mathcal{O}(10^{-3})$. From the convergence tests we discussed above in this section we see, that on the chosen domain size of 100×100, finite size effects are still relevant. Previous discussion showed that finite size effects have a more severe influence on $t(V_{\mathrm{X}} = \max(V_{\mathrm{X}}))$ than on $\max(V_{\mathrm{X}})$.

We found, that simulations for the non-linearized model show an excellent agreement with simulations for the linearized model. The found prefactor $\alpha = 0.827$ agrees with the limiting velocity we found in Fig. 30, where we found 0.858 as a limit velocity. The break of the scaling presented occurs at $\hat{\eta} \approx 1.0$. This is anticipated, since our theory is valid only for small values of $\hat{\eta}$, $\hat{\eta} \ll 1$.

6.4 Sheath dissipation

The effects of sheath dissipation on blob dynamics for the non-linearized model equations are studied. We are interested in the velocity scaling with the sheath dissipation parameter. In this chapter we present a short convergence test and present simulation parameters that yield converged simulations with sheath dissipation for the non-linearized model. We proceed then with a parameter scan for σ at fixed $\hat{\eta}$ and discuss blob dynamics and evolution. Finally, we investigate the scaling properties for V_{X} . A discussion of their physical interpretation is postponed to section Sec. 8.4.

The simulation setup is the same as in the previous section, but we include the sheath dissipation term $\sigma\phi$ in the vorticity equation. Initial conditions for the fields are the gaussian structure for the particle density and a zero field for the vorticity.
The convergence behavior is similar to the previous sheath dissipation parameter scan. Long spatial scales are suppressed by the $\widehat{\phi}_{\mathbf{k}}/k_\perp^2$ term in the vorticity equations, thus small simulation domains can be used for values of $\sigma \geq 0.01$. The domain sizes and number of modes on which convergence has been tested are listed in Tab. 15). The simulation domains used have been tested for a vanishing electrostatic potential at the upper and lower poloidal boundaries at times shortly before, at, and after the maximum velocity. Convergence with respect to number of modes has been tested for by comparing the curves for V_X and by examining surface plots of θ for unphysical artefacts. Parameters that yield converged simulations are marked in that table with a $\surd$.

$\hat{\eta}$			σ	Domain	Modes	Converged		
0.1	1.0	20.0	0.1	50×50	512×512	$\surd$		
0.1	1.0	20.0	0.1	50×50	768×768	$\surd$	$\surd$	$\surd$
0.1	1.0	20.0	0.1	50×50	1024×1024	$\surd$	$\surd$	$\surd$
0.1	1.0	20.0	1.0	20×20	512×512	$\surd$		
0.1	1.0	20.0	1.0	20×20	768×768	$\surd$	$\surd$	
0.1	1.0	20.0	1.0	20×20	1024×1024	$\surd$	$\surd$	$\surd$

Table 15: Convergence scan for sheath dissipation

In Fig. 54 we present COM velocity curves for several simulations to present the rate of convergence with increasing number of modes. For all presented resolutions, $\max(V_{\mathrm{X}})$ varies very little with the change in spectral resolution. The time where the blob travels with maximum velocity shows little variance as well. In the regime after $\max(V_{\mathrm{X}})$ is attained, the radial COM velocity curves show more variance. We therefore increase the resolution to 1536×1536 modes in the parameter scan for simulations with $\hat{\eta} \geq 1$ and $\sigma \geq 0.1$. Only $\max(V_{\mathrm{X}})$ and $t(V_{\mathrm{X}} = \max(V_{\mathrm{X}}))$ are used for quantitative analysis, we describe the late blob evolution qualitatively.

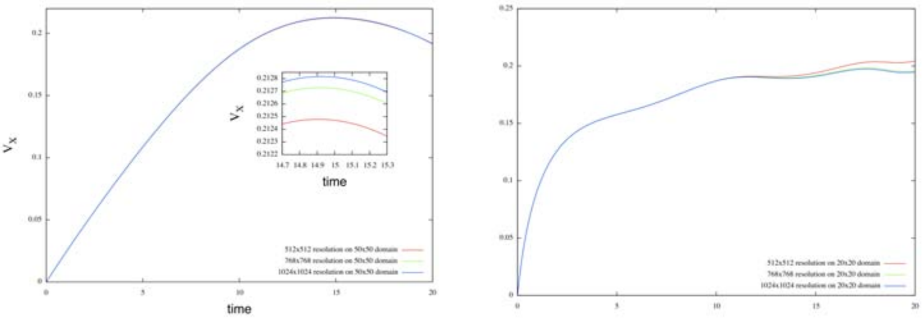

(a) COM velocity for $\hat{\eta}\ = 0.1$, $\sigma = 0.1$ (b) COM velocity for $\hat{\eta}\ = 1.0$, $\sigma = 1.0$

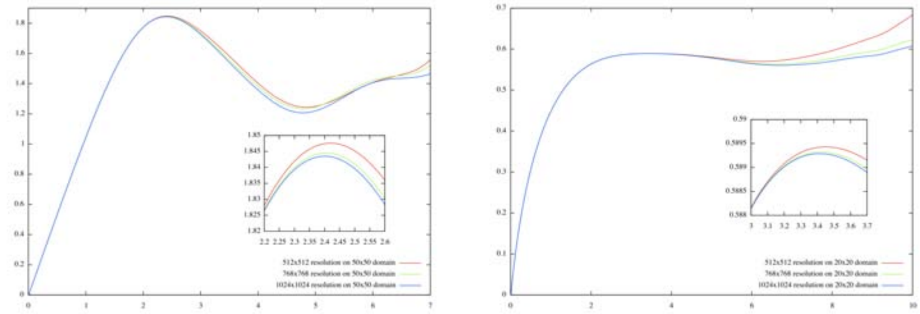

(c) COM velocity for $\hat{\eta}\ = 20.0$, $\sigma = 0.1$ (d) COM velocity for $\hat{\eta}\ = 20.0$, $\sigma = 1.0$

Figure 54: Convergence with respect to number of modes for different simulation parameters. Simulation results are from the non-linearized model.

6.4.1 Parameter scan

We proceed by varying the sheath dissipation parameter σ for a fixed relative characteristic particle density perturbation amplitude $\hat{\eta}$ and for fixed diffusion and viscosity coefficient κ and μ. In all simulations, we hold $\kappa = 10^{-3}$ and $\mu = 10^{-3}$. A time step of $\Delta_t = 10^{-3}$ is used, diagnostic output is written out every 10^{-2} time units, full output is written out every 5×10^{-1} time units. The simulations are presented in Tab. 16. We have chosen to run some simulations with a large value of σ longer than others, so that we can discuss the late blob evolution of these simulations.

In the previous section we have discussed that an increasing particle density perturbation has significant influences on the time scales of the blob dynamics. Large perturbations give an increased radial COM velocity. We now study how this effect competes with the dampening induced by sheath dissipation.

$\hat{\eta}$					σ	t_{end}				
0.1	0.2	1	2	10	0.01	20	20	10	10	10
0.1	0.2	1	2	10	0.02	20	20	10	10	10
0.1	0.2	1	2	10	0.05	20	20	10	10	10
0.1	0.2	1	2	10	0.10	20	20	10	10	10
0.1	0.2	1	2	10	0.20	20	20	10	10	10
0.1	0.2	1	2	10	0.50	20	20	10	10	10
0.1	0.2	1	2	10	1.00	40	20	20	10	20
0.1	0.2	1	2	10	2.00	40	20	20	10	20
0.1	0.2	1	2	10	5.00	40	20	20	10	20
0.1	0.2	1	2	10	10.00	40	20	20	10	20
0.1	0.2	1	2	10	20.00	40	20	20	10	20
0.1	0.2	1	2	10	50.00	40	20	20	10	20
0.1	0.2	1	2	10	100.00	40	20	20	10	20

Table 16: Simulation parameters for sheath dissipation parameter scan with variable particle density perturbation amplitude.

Discussion for sheath dissipation parameter $\sigma = 0.1$ Blob dynamics for different values of $\hat{\eta}$ are presented in Fig. 55. We see that small sheath currents habe a neglible effect on the blob dynamics. Compared to Fig. 50 and Fig. 52 from the previous section, we see that the maximal COM velocities are some 25 % lower than without sheath dissipation, through the whole simulation, the blobs travel with a lower radial velocity. Sheath dissipation is also responsible for the blobs reaching their maximum velocity earlier. The late evolution of the simulation with $\hat{\eta} = 10$, after $t \approx 7$ is dominated by a cascade of Rayleigh-Taylor instabilities occurring at the blob front. In the late evolution, the COM velocity is strongly reduced by sheath dissipation. Fig. 52 shows that without sheath dissipation the dispersed blob structure travels with a COM velocity of the same magnitude as the coherent plasma blob at peak velocity.

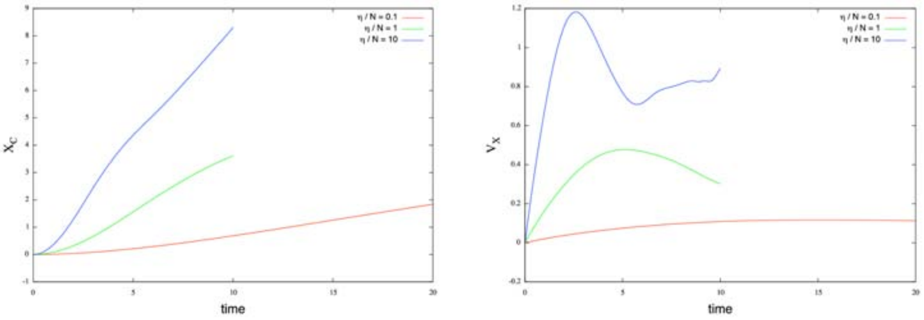

(a) Radial COM coordinate

(b) Radial COM velocities

Figure 55: Radial COM coordinates for simulations of the non-linearized model with $\sigma = 0.1$

Discussion for sheath dissipation parameters $1.0 \leq \sigma < 10$.

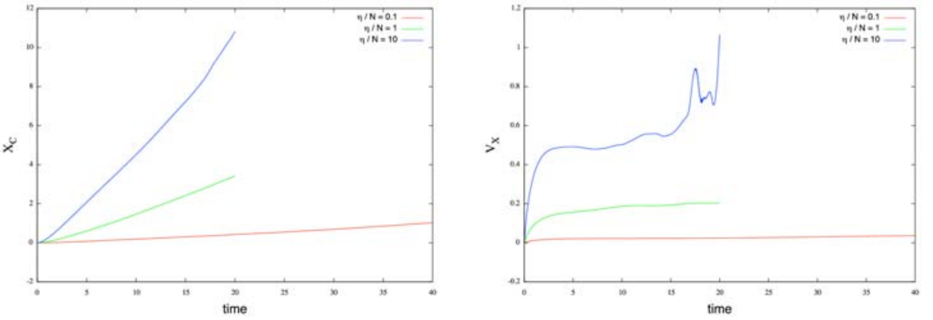

(a) Radial COM coordinate

(b) Radial COM velocities

Figure 56: Radial COM coordinates for simulations of the non-linearized model with $\sigma = 1.0$

Discussion for sheath dissipation parameter $\sigma = 1$ For sheath dissipation parameter $\sigma = 1$, there is a strong attenuation of the blob dynamics. Comparing Fig. 56 to Fig. 50 and Fig. 52 we see that $\max(V_\mathrm{X})$ is some 50% slower for simulations with $\hat{\eta} = 0.1, 1.0$ and 10.0. The simulations show also no deceleration of the blob after it reaches $\max(V_\mathrm{X})$. For $\hat{\eta}$ =1.0, another acceleration phase of the blob begins after $t \approx 5$, where V_X increases from $V_\mathrm{X} \approx 0.16$ at $t \approx 5$ to $V_\mathrm{X} \approx 0.19$ at $t \approx 12$. This acceleration is due to the blob front being subject to the Rayleigh Taylor instability. Contour plots of the blob evolution are presented in Fig. 57. Until $t \approx 5$, the particle density maximum has moved radially outwards, whereas the bulk plasma of the blob has moved only little. At $t \approx 5$ a bulk motion of the plasma blob sets in, giving an structure that is elongated over some 5 initial blob lengths. After 12 ideal interchange times, the blob is a coherent structure with its bulk density traveling radially outwards, shown in Fig. 57(a). Fig. 57(b) shows the electrostatic potential for the same time. Compared to a simulation without sheath dissipation, Fig. 47(b), we see a fundamentally different shape of the blob structure. Vertical gradients in particle density over a longer radial range cause the bulk plasma to build up a steep density front. This front is transported radially outwards at a larger speed than the bulk plasma. Since the front holds large mass, this increase is responsible for the continued increase in COM velocity. In Fig. 57(c) and Fig. 57(d) we present the blob at $t = 20$ where it has been subject to a cascade of instabilities at the front of the blob. The figure shows that the blob as a coherent structure, elongated over some 7 initial blob length units.

Fig. 57 presents an electrostatic potential with a characteristic length scale comparable to the blobs length scale. The spatially localized potential causes the blob to maintain a coherent structure. Simulations without sheath dissipation and $\hat{\eta} = 1.0$, as in Fig. 47(b), show a blob that extends over some 5 initial blob lengths in the poloidal direction.

A similar evolution occurs for a simulation with $\hat{\eta} = 10$ and $\sigma = 1$. The evolution after the blob has reached its peak velocity at $t \approx 5$ and has decelerated at $t \approx 7$, is dominated by instabilities. Large particle density gradients cause strong interchange motions that are

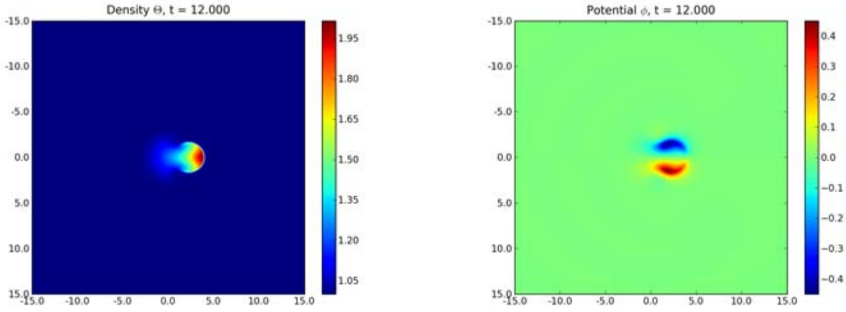

(a) Particle density at $t = 12.0$ (b) Electrostatic at $t = 12.0$

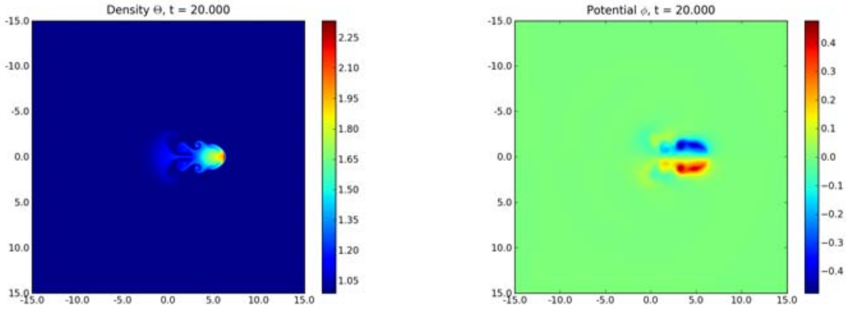

(c) Particle density at $t = 20.0$ (d) Electrostatic potential at $t = 20.0$

Figure 57: Blob evolution for $\hat{\eta} = 1.0$, $\sigma = 1.0$

damped by the sheath currents. The blob structure is subject to instabilities at the front, leading to a strong dispersion of the blob structure. From Fig. 56 we see, that at this point, the blob has already travelled 7 initial blob length units.

Discussion for sheath dissipation parameters $\sigma \geq 10.0$ Sheath dissipation parameters $\sigma \geq 10$ bring interchange motions almost to a complete halt. After a very quick initial acceleration, sheath dissipation damps further acceleration almost instantly and causes the blob to travel radially outwards at a constant speed. Simulations with a particle density amplitude $\hat{\eta} \geq 10$, show that an acceleration in the COM velocity curves, presented in Fig. 58.

The secondary acceleration for $\hat{\eta} = 10$ is due to the finger instability, illustrated in Fig. 59. This instability features plasma transport that is zero at the symmetry axis $y = 0$. Contour plots of the electrostatic potential show a vanishing gradient $\phi_y = 0$ at $y = 0$, so there is no advection due to the $E \times B$ drift on this axis. Plasma is transported around this barrier at $y = 0$.

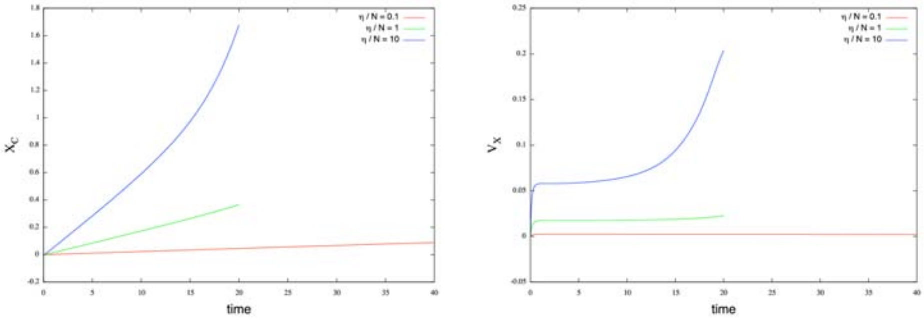

(a) Radial COM position (b) Radial COM velocities

Figure 58: Radial COM coordinates for simulations of the non-linearized model with $\sigma = 10.0$

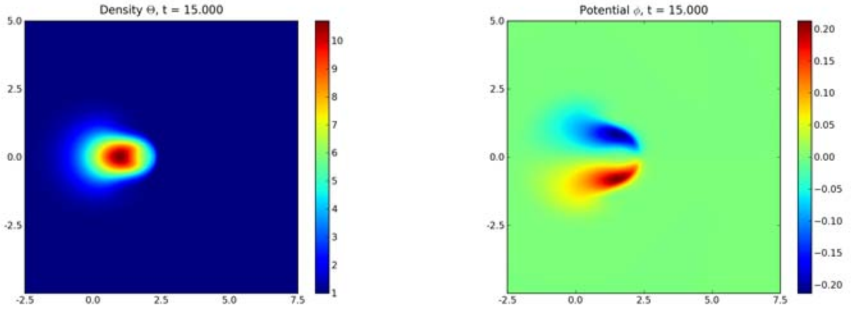

(a) Particle density $t = 15.0$ (b) Electrostatic potential $t = 15.0$

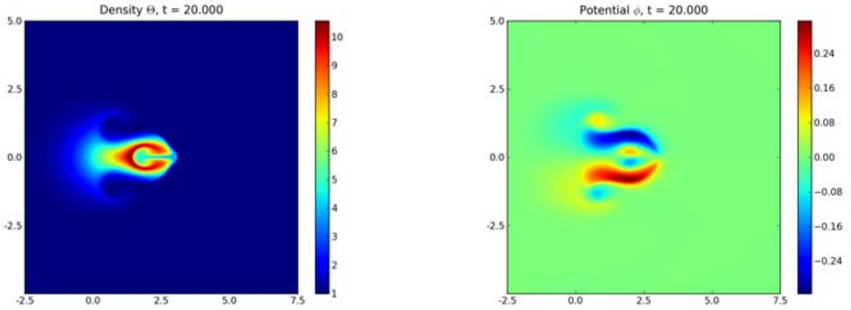

(c) Particle density $t = 20.0$ (d) Electrostatic $t = 20.0$

Figure 59: Blob evolution for simulation with $\sigma = 10.0$, $\hat{\eta} = 10.0$. We see the finger instability occur at the front of the blob.

6.4.2 Scaling properties

In the previous section we discussed qualitatively the dampening effect parallel electric currents have on the blob dynamics. We proceed by quantifying the effects sheath dissipation has on blobs with variable amplitude. We then present the impacts on the velocity scaling

with the blobs characteristic length l.
Determining $\max(V_X)$ from the V_X curves presents the same difficulties as discussed in Sec. 5.3. With increasing $\hat{\eta}$, the blob dynamics transit into a regime that features no pronounced maximum. Instead, the late blob dynamics features additional acceleration phases and depend sensitively on the model parameters κ and μ. These are due to the instabilities discussed in the previous subsections. We analyze the initial blob acceleration phase, since this evolution is common to all simulations. To determine the peak velocity before the blob enters this regime, we apply the same cutoff procedure as presented in Sec. 5.3. We define a cut-off time $t_{\max}$ by determining the minimum of $dV_X\ /dt$ and find $\max(V_X)$ on the interval $[0 : t_{\max}]$. This way, we find a good approximation for $\max(V_X)$ after the initial acceleration phase of the blob. This method yields acceptable results for $t(V_X = \max(V_X))$ in most cases. In Fig. 60 we present V_X for simulations with $\hat{\eta}\ = 10$ and σ from 0.1 to 100. V_X is drawn in a solid green line, continued with a red dashed line for times $t \geq t_{\max}$. The position of the used maxima $\max(V_X)$ is denoted with a vertical black line. In case of $\sigma = 2.0$, we set manually set $t_{\max} = 5.0$ since the inflection point method was giving unusable results.

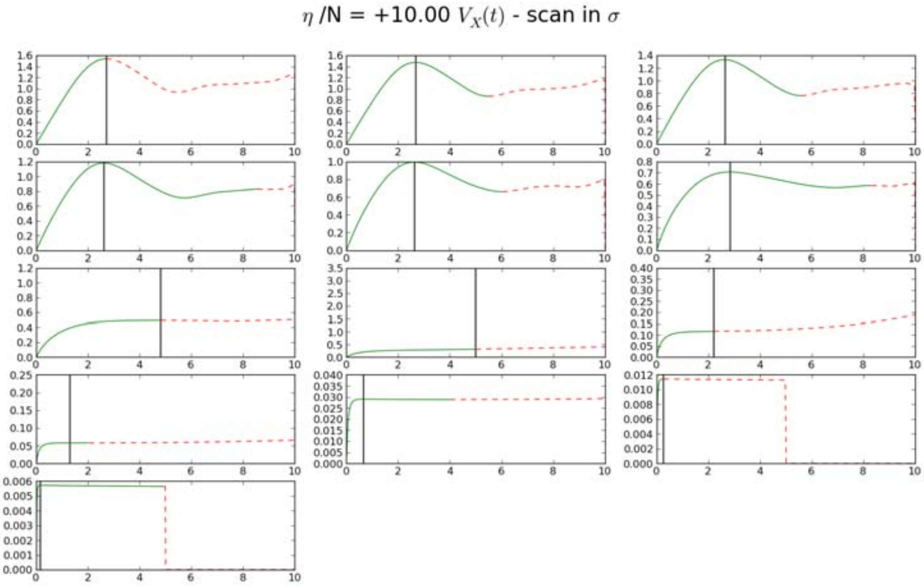

Figure 60: V_X curves for $\hat{\eta}$ =10, $\sigma = 0.1$ on the upper left plot and increases row wise over the values listed in Tab. 16 to $\sigma = 100$ in the lowest graph. $\max(V_X)$ is determined on the interval denoted by the solid green line. For $t \geq t_{\max}$, the graph is continued with a dashed red line. Vertical bars denote the position of $\max(V_X)$.

In Fig. 61(a) we present $\max(V_X)$ as a function of the sheath dissipation parameter for different values of the density perturbation amplitude. Values for which $\max(V_X)$ could not be exactly identified are presented by crosses not attached to the solid line. We find that

$\hat{\eta}$	α	β	ϵ	ζ
0.1	0.023	−0.992	13.362	−0.805
0.2	0.045	−0.994	13.421	−0.809
1.0	0.175	−0.998	15.401	−0.875
2.0	0.281	−1.001	19.975	−0.977
10.0	0.584	−1.003	13.010	−1.001

Table 17: Results for least squares fit to Eqn. (76) over $\sigma \in [5 : 100]$ and to Eqn. (77) over $\sigma \in [10 : 100]$.

.

$\max(V_X)$ is decreasing with increasing sheath dissipation for a given value of $\hat{\eta}$. The form of decrease suggests that for values of $\sigma \geq 5$ there is a power law relation between $\max(V_X)$ and σ:

$$\max(V_X)\ (\sigma) = \alpha \times \sigma^{\beta} \tag{76}$$

The results of a least squares fit for a power law fit over $\sigma \in [5 : 100]$ are presented in Tab. 17. The square of the residuals per degree of freedom for this fit are typically $\mathcal{O}(10^{-6})$, the fit is practically exact. We find that the exponent β shows only little variation while the coefficient α shows a significant increase for increasing $\hat{\eta}$.
A similar fit for $t(V_X = \max(V_X))$ is done on the domain $\sigma \in [10 : 100]$:

$$t(V_X = \max(V_X))\ (\sigma) = \epsilon \times \sigma^{\zeta}, \tag{77}$$

the found fit parameters are in principle exact. The fit parameters ϵ and ζ are presented in Tab. 17. The fit exponent ζ resembles the same trend as the fit exponent β, but much less pronounced. We see a small decay of ζ from −0.992 for $\hat{\eta}$ = 0.1 to −1.003 for $\hat{\eta}$ = 10.0, which indicates that this exponent approaches a limit slightly less than negative unity from above. The fit coefficient ϵ increases for $\hat{\eta} \leq 2$ and shows a sudden decrease for $\hat{\eta}$ = 10. This is anticipated from Fig. 61(b), where the V_X curve for $\hat{\eta} = 10$ lies beneath the V_X curves. These results are discussed in context of experimental findings and results from the linearized model in Sec. 8.4

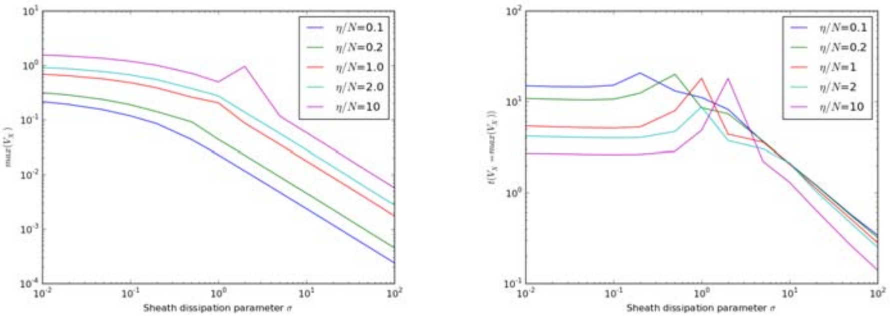

(a) Scaling for $\max(V_{\mathrm{X}})$ with σ.

(b) Scaling for $t(V_X = \max(V_{\mathrm{X}})\ )$ with σ.

Figure 61: COM velocity peak scaling with sheath dissipation parameter σ.

7 Secondary instabilities in blob simulations

In the previous section we saw the formation of hydrodynamical instabilities in some simulations, the Rayleigh-Taylor instability at the front of a blob and the Kelvin-Helmholtz instability at the arms of the blob. We now study these instabilities further. By choosing an appropriate set of initial conditions we simulate both instabilities with the `2dads` code and determine growth rates of initial perturbations to the initial conditions.

We use the term secondary instabilities to denote instabilities with length scales of the plasma blob. In this terms, a primary instability has a length scale associated to length scales of the SOL is the plasma blob itself.
By providing initial conditions that are known to be unstable to the Kelvin-Helmholtz mode, or the Rayleigh-Taylor mode respectively, and qualitatively comparing the resulting structures to previous blob simulations, we show, that the secondary instabilities are correctly identified.

7.1 Kelvin-Helmholtz instability

Blob simulations with $\mathrm{Ra} \gtrsim 10^6$ and $\mathrm{Pr} = 1$ showed that the blobs developed a mushroom shape, which feature plasma lobes stretching along the poloidal direction. Along these lobes, the vorticity Ω formes a double layer. It is this vorticity double layer that is unstable to the Kelvin-Helmholtz mode and causes a twirling of the plasma in the lobes, as presented in for example Fig. 51.

We observe that a vorticity double layer is unstable to the Kelvin Helmholtz mode. We therefore present simulations of an isolated vorticity double layer with in initial gaussian particle density profile. We ignore interchange motions in these simulations to present the instability that arise only because of the instable vorticity double layer. The particle density θ is treated as a passive scalar field and is only advected via the $E \times B$ drift. Initial conditions for the simulations read:

$$\begin{aligned}
\Theta(t=0) &= \exp(-x^2/2) \\
\Omega(t=0) &= \frac{\sinh(x)}{\cosh(x)^2} + \delta \exp(-x^2/2)\cos(2\pi\lambda y/L_y)
\end{aligned}$$

The perturbation chosen has an initial wavelength λ and a perturbation strength δ as a free parameter. The parameter λ is used to control the wavelength of the perturbation. Fig. 62 presents the $E \times B$ velocities and the electrostatic potential affiliate with the initial vorticity. Note that since $\Omega = \nabla_\perp^2 \Phi = \Phi_{xx} + \Phi_{yy}$, integrating Φ twice yields a function that is not periodic. We subtract a linear function from Φ: $\Phi \rightarrow \Phi' = \Phi - (\max\Phi - \min\Phi)x/L_x$. With this transformation, the electrostatic potential is periodic in x with $\Phi(-L_x) = \Phi(L_x) = 0$ as shown in Fig. 62. Solving the elliptic equations $\phi = \nabla^{-2}\Omega$ in Fourier space, the periodic solution is automatically assumed by the code.

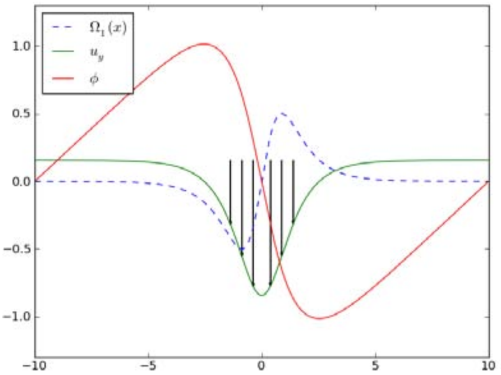

Figure 62: Initial vorticity profiles studied for the Kelvin-Helmholtz instability

μ	λ
10^{-2}	1 / 2 / 5 / 10
10^{-3}	1 / 2 / 5 / 10
10^{-4}	1 / 2 / 5 / 10

Figure 63: Parameters used for simulations of the Kelvin-Helmholtz stability.

We study the stability of the system by varying the wavelength of the perturbation λ and the viscosity μ, and study the growth rate of the mode λ. For this we define the quantity P via

$$P(k_y, t) = \sum_{k_x} |\hat{\Omega}_{\mathbf{k}}(t)|^2.$$

For a given mode k_y we summate the absolute value of the Fourier coefficients of the vorticity over all modes k_x. The initial perturbation wavelength λ is related to k_y, as $\lambda = 1$ is the lowest k_y value, $\lambda = 2$ is the second lowest k_y value and so on. The parameters we study are listed in Tab. 63. Simulations are carried out with both presented initial conditions for Ω. All simulations are run with a resolution of 1024×1024 on a 10×10 domain, with a perturbation amplitude of $\zeta = 10^{-2}$. Finite size effects are not relevant, since the electrostatic potential is forced to zero at the radial boundaries. Studies with a varying number of modes showed that a larger number of modes has no visible effect on contour plots of the fields and on the time evolution of P.

7.1.1 Simulations and growth rates

The simulations from Tab. 63 show, that the vorticity double layer is subject to strong perturbations. The initially straight layer between positive and negative vorticity is subject to elongations in the radial direction. In Fig. 64 we present vorticity and particle density after 50 ideal interchange times. We also observe that the vorticity double layer rolls up around a number of centers, that is equal to the number of local extrema of the initial perturbation along the poloidal direction. These roll ups are characteristic for the Kelvin-Helmholtz instability. The particle density rolls up in the same way, as it is advected with $E \times B$ velocity.

Simulations show, that both, initial perturbation wavelength λ, and viscosity have a signif-

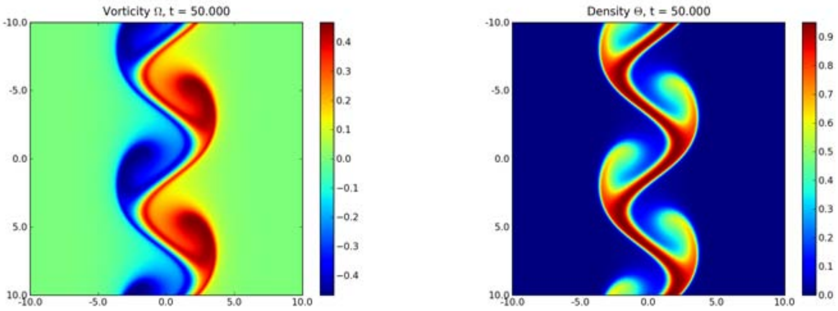

(a) Vorticity Ω for $\lambda = 2$ and $\mu = 10^{-4}$ at $t = 50$

(b) Particle density θ for $\lambda = 2$ and $\mu = 10^{-4}$ at $t = 50$

Figure 64: Contour plots for evolution of initial vorticity double layer

icant influence on the scale of the rolled up structures. This is shown in Fig. 65, where we present the evolution of $P(k_y, t)$ for initial values of $\lambda = 1, 2, 5, 10$ and $\mu = 10^{-2}, 10^{-3}$ and $\mu = 10^{-4}$. The mode k_y corresponds to the initial perturbation wavelength λ. For all values of λ we read, that viscosity has a dissipative effect on the evolution of P. Further do we see that an increasing value of λ has a stabilizing effect on the instability. For $\lambda = 10$ we see that after a initial growth phase, P decays to values close to zero. This shows the strong non-linear character of the instability. The initial power of this mode is transferred to other modes in the spectrum and therefore dissipated. This causes a dampening of the initial wavelength λ and the instability cannot grow in time as it would for small values of λ.

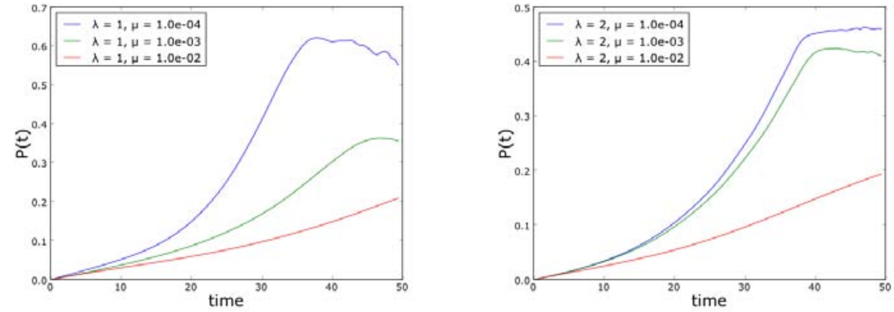

(a) $\lambda = 1$ (b) $\lambda = 2$

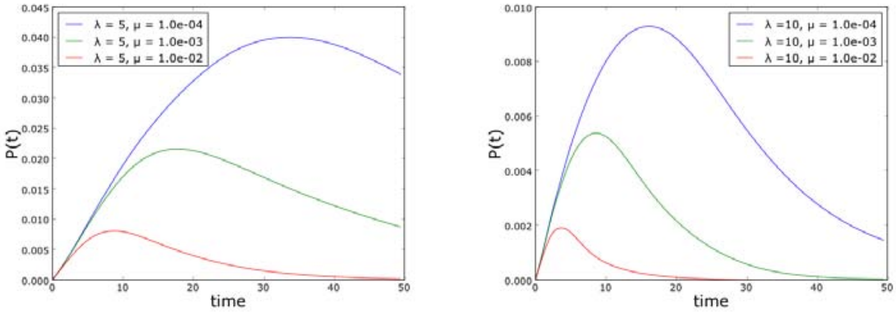

(c) $\lambda = 5$ (d) $\lambda = 10$

Figure 65: Evolution of the initial perturbation wavelength λ for the vorticity double layer.

7.2 Rayleigh-Taylor instability

Another observed secondary instability is observed at the blob front. Surface plots of the particle density in Fig. 57 show that the blob front is subject to a cascade of instabilities. These are most likely due to the Rayleigh-Taylor instability. In Sec. 6.4 we discussed that V_X in simulations for large blob amplitude and a sheath dissipation parameter $\sigma \geq 1$ is likely to be heavily influenced by the instability occurring at the blob front.

Simulations for small blob amplitude suggest the same instability mechanism operating at the blob front, as can be seen from Fig. 27 in Sec. 4. In this plot, we observe that a secondary blob detaches itself from the initial structure.

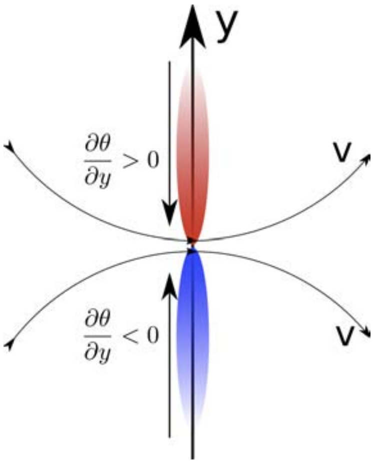

Figure 66: Phyiscal mechanism of the Rayleigh-Taylor instability observed at the blob front.

The physical mechanism of the instability is presented in Fig. 66. Vertical density gradients, denoted by the vertical ellipses, with different signs cause the generation of vorticity according to Eqn. (42). This vorticity implies a velocity field which is denoted by the circular arrows. For large enough vertical particle density gradients, this mechanism causes the blob front to drive away from the coherent structure. In simulations we see, that this can effectively separate the front from the rest of the blob.

A more abstract point of view, describes the vertical particle density gradient as an interface between two regions. The interchange term $\partial\theta/\partial y$ is acting as an effective gravity g, causing a net acceleration of the particle density left of the boundary towards the right.

7.2.1 Simulations and growth rates

For simulations of an isolated Rayleigh-Taylor instability we use the following initial conditions:

$$\theta(t=0) = \theta_0 \times \left(\frac{\sinh(x)}{\cosh(x)} - \frac{2x}{L_x}\right) + \zeta \exp(-x^2/2)\cos(\lambda 2\pi y/L_y)$$
$$\Omega(t=0) = 0.$$

The initial profile for the density features a sharp horizontal gradient at $x = 0$ and has boundary periodic conditions $\theta(t=0,-L_x) = \theta(t=0,+L_x)$. A perturbation with amplitude ζ and wavelength λ is added in the y direction to create initial vorticity. Simulations are run on a 10×10 domain with 1024×1024 modes in each direction. A time step of $\Delta_t = 10^{-3}$ is used, *tdiag* is 10^{-2} and *tout* is set to 5×10^{-1}. We study simulations where we set the $\lambda = 1, 2, 5, 10$ and vary the Rayleigh number over Ra $= 10^4, 10^6$ and 10^8 for each λ.
The evolution of the instability with $\lambda = 1$ is presented in Fig. 7.2.1. We see that a velocity profile as discussed previously is generating interchange motions, causing a motion of the bulk plasma to the right.

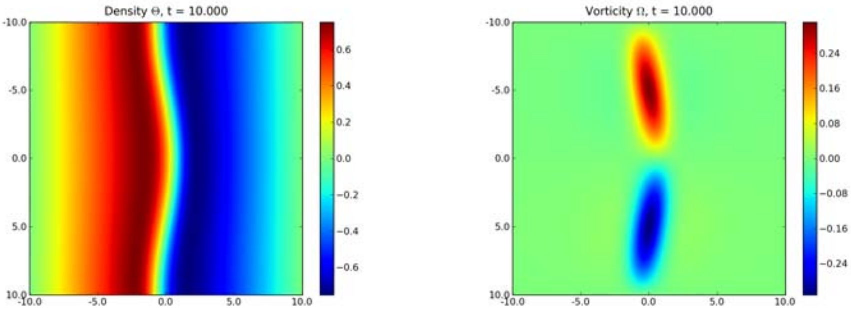

(a) Particle density $t = 10.0$ (b) Vorticity $t = 10.0$

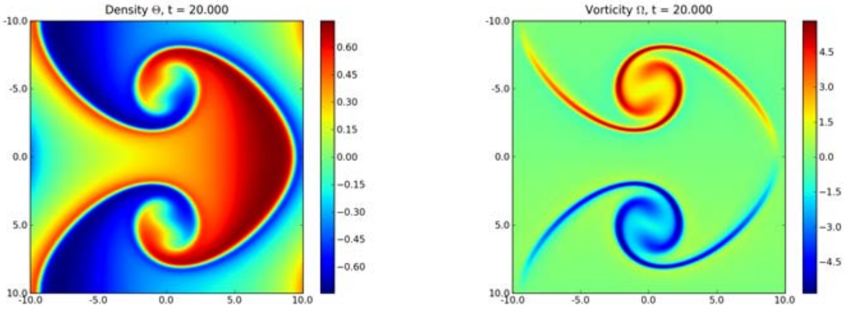

(c) Particle density $t = 20.0$ (d) Vorticity $t = 20.0$

Figure 67: Evolution of the rayleigh Taylor instability for initial perturbation wavelength $\lambda = 1$ and initial perturbation strength of $\zeta = 0.01$.

To study the effect of dissipation on the Rayleigh-Taylor instability we define the quantity P in the same manner as in Sec. 7.1:

$$P(k_y,t) = \sum_{k_x} |\hat{\theta}_{\mathbf{k}}(t)|^2.$$

With this, we can describe the growth of the initial perturbation with wavelength λ. In Fig. 68 we present the evolution of P for $\lambda = 1, 2, 5, 10$. We see, that dissipative forces have a dampening effect on the instability. We also see, that an increasing wavelength has little effect on P. For each wavelength the instability grows on similar time scales and with equal strength.

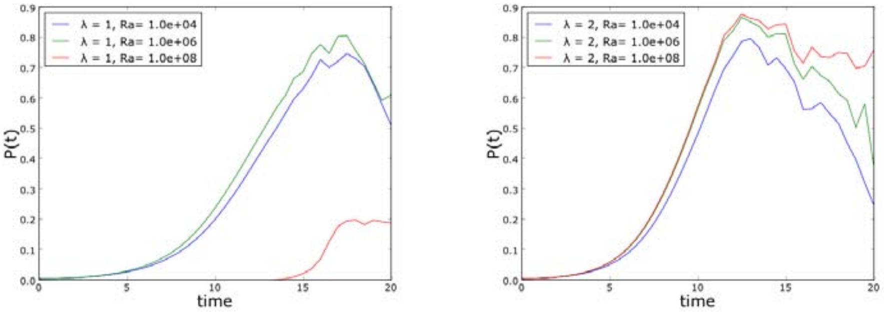

(a) $\lambda = 1$ (b) $\lambda = 2$

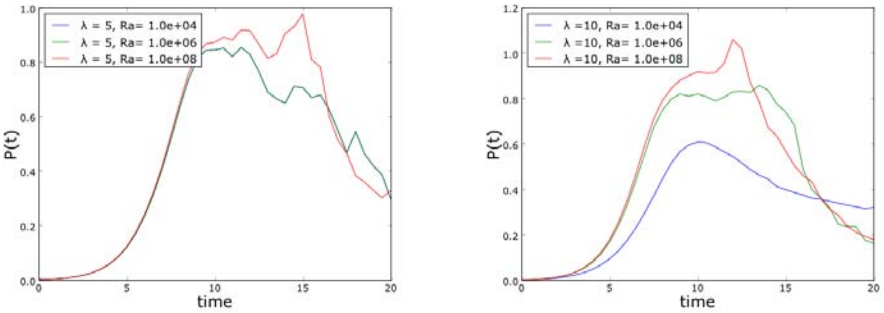

(c) $\lambda = 5$ (d) $\lambda = 10$

Figure 68: Evolution of the initial perturbation wavelength λ for the vorticity double layer.

8 Discussion

We continue with a discussion of the simulation results and adress issues with the method. The simulation results are set in relation to experimental measurements of plasma filaments of SOL plasmas in low and high confinement mode. Readily available experimental data allow the discussion of the results for plasmas in both confinement modes. Low confinement mode measurements show intermittent radial transport due to blob structures. Plasmas in the H mode show radial filament transport via ELMs which is due to a quasi-periodic teardown of the plasma confinement barrier.
In the second part of this section, we discuss issues concerning the applied method. A discussion of the aliasing error is presented, and other limiting factors on the efficiency of the implemented spectral method.

8.1 Blob propagation mechanism

All blob simulations show the radial propagation of an initial isolated particle density perturbation radially out over. The dynamic equations we simulate are in the simplest case given by:

$$\begin{aligned} \frac{\partial \theta}{\partial t} + \{\phi, \theta\} &= \kappa \nabla_\perp^2 \theta \\ \frac{\partial \Omega}{\partial t} + \{\phi, \Omega\} + \frac{\partial \theta}{\partial y} &= \mu \nabla_\perp^2 \Omega. \end{aligned}$$

The evolution equation for Ω is derived from the electric current continuity equations which includes polarization drift for ions, the diamagnetic drift for the electrons, as well as viscous stresses. The particle density θ is evolved with a simple advection-diffusion equation. When we neglect diffusion in the vorticity equation, we find

$$\frac{\partial \Omega}{\partial t} + \{\phi, \Omega\} = -\frac{\partial \theta}{\partial y}.$$

This identifies the interchange mechanism as the driving mechanism for blob motions. The interchange mechanism causes a polarization of the initial structure. This polarization causes an advection with the $E \times B$ drift of the blob as a coherent structure radially outwards. We can say, that the intertial response of the blob is due to the interchange drive.
Simulations of blobs presented in this study all show characteristic features of radial filament transport measured experimentally. This includes most prominently a steep front of the structure and a trailing wake. The simulations show, that the blob propagates as a coherent structure. It develops a mushroom-like front, with a strong radial particle density gradient at the front. In the absence of sheath dissipation we also observe poloidal stretching of the plasma blob and the development of lobes, which curl inward and propagate at a lower radial velocity outwards than the front of the blob.
For small values of collisional diffusion we observe small scale structures developing. The

front of the blob is unstable to the Rayleigh-Taylor mode. At the lobes, we observe the creation of a vorticity double layer that is unstable to the Kelvin-Helmholtz instability. We discuss both instabilities in Sec. 7.

Simulations with sheath dissipation revealed that an increasing value of the sheath dissipation parameter σ alters the characteristic length scales of the electrostatic potential ϕ. We can interpret this by the effect of the parallel electric sheath currents. For large values of σ, the diamagnetic currents are cancelled by parallel currents. They deplete the accumulated spatial charges and damp radial electric drifts. This explains the decreasing radial velocities, of the blob structures for increasing values of the sheath dissipation parameter σ.
By neglecting the electric drift advection terms and the interchange term in the vorticity equation, we find that the dynamics of the Fourier coefficients for the electrostatic potential are given by:

$$\frac{\partial \phi}{\partial t} = \nabla_\perp^{-2} \sigma \phi.$$

This solution suggests a solution in Fourier space, $\widehat{\phi}_k \sim \exp\left(-\sigma t / k_\perp^2\right)$. We observe this for the Fourier coefficients $\widehat{\phi}_k$ in simulations of the linearized parameter model with Ra $= 10^2$ for values of $\sigma \geq 0.1$, as shown in Fig. 69. The absolute value of the Fourier coefficient decay exponentially for both values of σ. The approximate solution above describes Fourier coefficients for the electrostatic potential only when we can neglect radial currents. The value of σ, for which the suggested exponential decay is dominant, increases with the Rayleigh number, due to increasing electric drift velocity of the blob structure. We also see $|\widehat{\phi}_k|$ assume smaller for $\sigma = 10$ than for $\sigma = 0.1$. Since an increasing value of σ effectively decreases the characteristic length of ϕ, we find a smaller contribution to ϕ from Fourier coefficients from base functions with long wavelength. The plot shows Fourier coefficients for base functions with long wavelength.

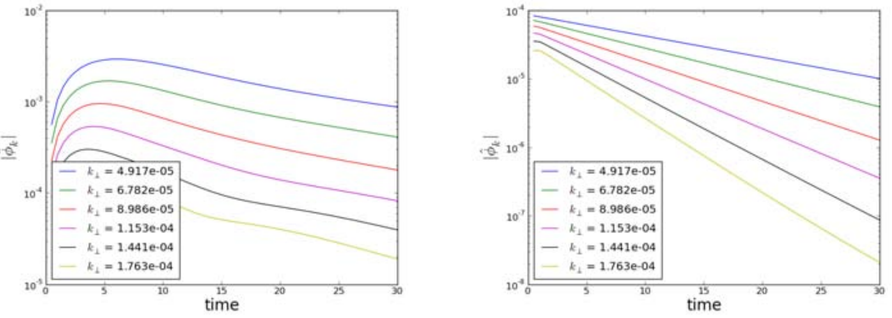

(a) Simulation #4, $\sigma = 0.1$ (b) Simulation #10, $\sigma = 10.0$

Figure 69: Fourier coefficients $|\widehat{\phi}|_k$ with small values of $k_\perp$ for simulations with Ra $= 10^2$ from Tab. 5.2.

8.2 Velocity scaling with Rayleigh number

In Fig. 30 we present the scaling of $\max(V_\mathrm{X})$ and $t(V_\mathrm{X} = \max(V_\mathrm{X}))$ with increasing Rayleigh number. We find that for increasing Rayleigh numbers $\max(V_\mathrm{X})$ asymptotically approaches a numerical value close to unity. The transition into the regime, where $\max(V_\mathrm{X})$ becomes independent of the Rayleigh number occurs at $\mathrm{Ra} \gtrsim 10^5$. In physical terms, a large Rayleigh number implies a regime where diffusion and viscosity are negligible. We convert the dimensionless velocity into a dimensional velocity we find:

$$V \sim C_s \sqrt{\frac{2l}{R}\frac{\Delta\theta}{\Theta}}.$$

Our results show that the blob velocity approaches a velocity that is of the order of the acoustic velocity times the root of the blob amplitude and structure size.

8.3 Scaling with large blob amplitude

The simulations with variable amplitude, Sec. 6.3 present the a power law relation between $\max(V_\mathrm{X})$ and $t(V_\mathrm{X} = \max(V_\mathrm{X}))$ and the blob amplitude $\hat{\eta}$. We find, the blobs maximal radial center of mass velocity scales with the blob amplitude as

$$\max(V_\mathrm{X})\ (\hat{\eta}\ ) \sim 0.827 \times \hat{\eta}^{\ 0.497}.$$

This results agrees with previous theoretical predictions in [15]. Also note, that the factor 0.827 agrees excellent with the scaling behavior of $\max(V_\mathrm{X})$ for large Rayleigh numbers discussed in the previous section. This scaling is found for relative blob amplitudes $\hat{\eta} \in [0.01 : 0.2]$. Our results suggest that in this region, the blob velocity is independent of the Rayleigh number. The Rayleigh number is defined as $\mathrm{Ra} = 1/\kappa\mu$, a large Rayleigh number indicates a low diffusion and a low viscosity.
Our results also show that this scaling breaks for blob amplitude $\hat{\eta} \geq 1.0$. In this regime we find that the velocity scales as $\max(V_\mathrm{X})\ (\hat{\eta}\ ) = 1.380 \times \hat{\eta}^{\ 0}.146$, which suggests a growing radial velocity for blobs with large amplitude. In this regime, the maximal radial blob velocity depends weaker on the blob amplitude. The region where the scaling transits gives a limit, for which the linearization of the interchange term is valid.

8.4 Velocity scaling with sheath dissipation

The results from Sec. 5.3 quantify the effect of the sheath dissipation parameter σ on blob dynamics for the linearized model. We read from Fig. 42(a), that $\max(V_\mathrm{X})$ decreases with increasing σ and from Fig. 42(b), that the initial blob acceleration period also decreases with increasing σ. The functional relation suggested from the data is in both cases a power law, $y = \alpha \times \sigma^\beta$. Due to uncertainties in determining $t(V_\mathrm{X} = \max(V_\mathrm{X}))$, we fit the model parameters α and β only for the relation $\max(V_\mathrm{X})\ (\sigma) = \alpha\sigma^\beta$. The fit parameters are presented in Fig. 44, for large Rayleigh numbers we find $\alpha \approx 0.24$ and $\beta \approx -1.0$. In the limit where diffusion and viscosity becomes negligible, the dampening effect of sheath dissipation approaches

a limit.
This limiting behavior is shown explicitly in Fig. 43 and compared to the simulation results without sheath currents. This limit has been previously discussed in Sec. 8.2 and was originally presented in [15] in the absence of sheath currents. Our findings show the significant reduction of $\max(V_{\mathrm{X}})$ to velocities some 20% of the acoustic velocity times the blob size when we consider sheath currents.

We now discuss the results of simulations with large blob amplitude with the non-linearized model. The results we discuss are presented in Sec. 6.4.2. From Fig. 61 we read the dampening effects of sheath dissipation on blob dynamics for different blob amplitudes. Here we find that the dissipative effect of sheath dissipation on the blob dynamics can be quantified in the same manner. The results from this chapter show that a functional relation suggested for both, $\max(V_{\mathrm{X}})\ (\sigma)$ and $t(V_{\mathrm{X}} = \max(V_{\mathrm{X}}))\ (\sigma)$ is a power law.

We proceed by translating the finding for both models into a scaling for the physical blob velocity v_{phys} with the blob length l

$$v_{\mathrm{phys}} \sim \alpha l^{\beta}.$$

For this, note first that in both parameter studies we found a result of the form

$$v \sim \mu^{\alpha} \kappa^{\beta} \sigma^{\epsilon} \hat{\eta}^{\,\zeta}. \tag{78}$$

In simulations with the linearized model we varied σ for a fixed Rayleigh number whereas in simulations for the non-linearized model we varied σ for a given blob amplitude $\hat{\eta}$ and Rayleigh number. All the quantities but $\hat{\eta}$ on the right hand side of Eqn. (78) depend on the characteristic length scale l. But as discussed in Sec. 4 we know, that the blob velocity varies only little with Ra for Ra $\gtrsim 10^4$. Our simulations are all well within this ideal regime. This allows us to neglect the influence of κ and μ in the analysis of how v_{phys} depends on l.
As both models used feature a different normalization, we calculate the dependence of the physical velocity v_{phys} on l separately for both models. For the linearized model, we convert Eqn. (74) to physical units via Eqn. (35) and find:

$$\begin{aligned} V_{\mathrm{X}} \sim \alpha \sigma^{\beta} \Rightarrow \frac{v_{\mathrm{phys}}}{\gamma l} &\sim \alpha \left(\frac{2 C_s l^2}{\gamma L_{\|} \rho_s^2} \right)^{\beta} \\ \Leftrightarrow v_{\mathrm{phys}} &\sim \alpha \gamma_0^{1-\beta} l^{1+2\beta} \sqrt{\hat{\eta}} \left(\frac{2 C_s}{L_{\|} \rho_s^2} \right)^{\beta} \\ \Leftrightarrow v_{\mathrm{phys}} &\sim \alpha l^{\frac{1+5\beta}{2}} g^{\frac{1-\beta}{2}} \sqrt{\hat{\eta}} \left(\frac{2 C_s}{L_{\|} \rho_s^2} \right)^{\beta}. \end{aligned} \tag{79}$$

This equations gives the scaling law for the physical velocity in case of small blob amplitudes. Numerically computed values for the fit parameters α and β are presented in Fig. 44.

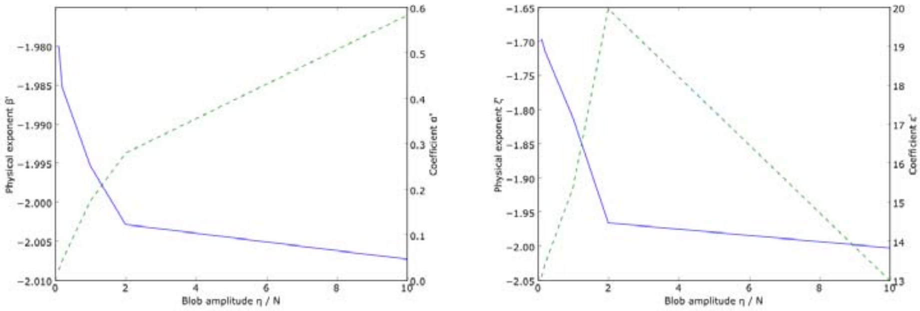

(a) Physical length exponent β' for v_{phys} (b) Physical length exponent ζ' for $t(v_{\text{phys}} = \max(v_{\text{phys}}))$

Figure 70: Physical scaling exponents. The solid line is the scaling exponent with its scale on the left axis ticks, the scaling coefficient is denoted by the green dashed line with its scale on the right y axis ticks.

For large blob amplitudes, a similar analysis with the normalization of the non-linear model yields:

$$v_{\text{phys}} \sim \alpha l^{\frac{1+5\beta}{2}} g^{\frac{1-\beta}{2}} \left(\frac{2C_s}{L_{\|}\rho_s} \right)^{\beta} = l^{\beta'}$$

$$t \sim \epsilon l^{\frac{-1+3\zeta}{2}} g^{\frac{1+\zeta}{2}} \left(\frac{2C_s}{L_{\|}\rho_s} \right)^{\zeta} = l^{\zeta'}.$$

The numerically found values for fit parameters α, β, ϵ and ζ were presented in Tab. 17. Note that for small blob amplitudes, we predict a velocity scaling $v_{\text{phys}} \sim \sqrt{\hat{\eta}}$, which is imminent in the model normalization. This compares favorably with the scaling we found in numerical studies where we explicitly set the blob amplitude as a model parameter.
Values for the physical scaling law of the non-linearized model are presented in Fig. 70(b). We read, that the scaling exponent ζ' approaches values of $l \approx -2$ for large blob amplitudes. For both models, we find a scaling of $\max(V_{\text{X}})\ (\sigma) \sim \sigma^{-1}$. This translates to a scaling for the physical velocity with the blob length,

$$v_{\text{phys}} \sim l^{-2}$$

for both models. The result we find is well known in literature and presented in various articles, [5, 26, 12, 11, 10, 26]. It remains to compare this scaling to analytically obtained scaling laws and compare the velocities predicted by both models.

We continue by presenting the analytic solution.
Recall that we derived the vorticity equation Eqn. (42) from the quasi-neutrality condition:

$$\underbrace{\frac{\partial \Omega}{\partial t} + \{\Omega, \phi\}}_{\nabla J_p} + \underbrace{\frac{\partial \theta}{\partial y}}_{\nabla J_d} = -\nabla J_{\|}.$$

For small values of σ, quasi neutrality requires, that polarization currents are cancelled by diamagnetic currents. They give rise to strong radial electric drifts. For large values of σ, the diamagnetic currents are cancelled by parallel currents. These deplete the accumulated spatial charges and damp radial electric drifts. If we the neglect viscous stress, we write the dimensional vorticity equation as

$$\frac{g}{n}\frac{\partial n}{\partial y} = \sigma_{\mathrm{phys}}\phi,$$

with the dimensional sheath dissipation parameter $\sigma_{\mathrm{phys}} = 2C_s/L_{\|}\rho_s^2$. Linearizing the interchange term for small blob amplitudes gives $\sigma_{\mathrm{phys}}\phi = g/l\Delta n/N$, where l is the characteristic scale on which the particle density varies. We know that the dominant velocity the blob moves with is the $E \times B$ velocity. Its radial component is given by $\underline{u}_{E,x} = 1/B - \phi_y$. Assuming that the electrostatic potential varies over the same length as the particle density, we find that $\phi \sim \underline{u}_{E,x}Bl$. Inserting this in the linearized expression gives a scaling of the physical blob velocity:

$$v \sim \frac{1}{\sigma_{\mathrm{phys}}}\frac{g}{l^2}\frac{\Delta n}{N}.$$

We find a similar analytical scaling if we do not linearize the interchange term. The equation with neglected polarization drift term admits solution of the form:

$$n(x, y, t) = \eta(x - \frac{g}{\sigma_{\mathrm{phys}}}t) \times \exp\left(-\frac{y^2}{2l^2}\right),$$

where the function $\eta(x, t)$ is the initial condition for the particle density, $n(x, t = 0) = \eta(x)$. The blob length scales in the poloidal direction are normalized by the blobs characteristic length scale l. Solving this equation for ϕ, we find:

$$\phi = -\frac{gy}{\sigma_{\mathrm{phys}}}$$

and note that this solves the particle density evolution equation when we neglect collisions. This shows, that the equations admit a solution that describes the radial advection of an initial structure radially outward with a velocity that is constant in space. Further do we note, that the electrostatic potential is uniform in the radial direction and depends only on the poloidal coordinate. The analytical result is valid for infinite blob amplitudes only, as the solution does not admit functions with a constant background. Also note, that vorticity dynamics does not enter this theory, as the velocity is a gradient field.
A comparison between the velocities predicted from analytical results and our numerical studies are presented in Fig. 71. From the figure we read, that while the l^{-2} scaling is verified, the analytical overestimates the prefactors of the velocities by a significant amount. This shows, that interchange motions and vorticity dynamics have a significant influence on the blob dynamics.

8.5 Comparison to experiments

This sections presents a discussion of the numerical results in context with experiments. We present experimental measurements of filament structures in the SOL of magnetically

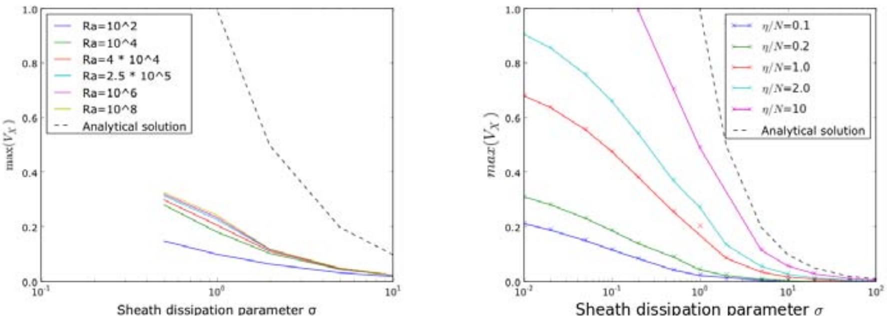

(a) Linearized model (b) Linearized model

Figure 71: Comparison between analytically predicted velocity scaling and numerical results.

confined plasmas. Due to their different characteristics, we discuss SOL turbulence and ELM filaments separately.

SOL turbulence Turbulences in the SOL of magnetically confined plasma are characterized by a intermittent fluctuations of the plasma. Experimental data from measurements of SOL turbulence in various Tokamaks, see for example [30, 39, 23, 19] , present large burst fluctuations in the time series of conditionally averaged particle density. These burst fluctuations account for a large fraction of the total radial transport in the SOL. The shape of the averaged particle density time series indicate, that the radial transport is due to radially propagating structures. This is supported by measurements of the plasma in the plane perpendicular to the magnetic field in the SOL. Measurements using high speed cameras [33] and gas puff imaging [41, 34] observe coherent structures that extend in the radial-poloidal domain and feature a strong particle density maximum. The observed structures have a extend of $\approx$ 1cm, typical radial velocities are ca. $1 - 10$ % of the acoustic velocity.
Physical parameters for the mid SOL of a plasma confined with the L mode are taken to be

$$\begin{aligned} n \approx 10^{20}\mathrm{m}^{-3}, \qquad & T_e = T_i = 25\mathrm{eV} \\ R \approx 1\mathrm{m}, \qquad & B \approx 1\mathrm{T}, \qquad L_{\|} \approx 10\mathrm{m}. \end{aligned} \tag{80}$$

Typical parameters measured for blob structures are

$$l \approx 0.01\mathrm{m} \qquad \hat{\eta} \approx 0.5.$$

We take these parameters from [15]. Similar values are used elsewhere in literature, [20, 26]. With this we can compute values for the acoustic velocity C_s, the strength of the effective gravity g, the ideal interchange time unit $1/\gamma$ and the ion thermal gyro radius, $\rho_s = C_s/\omega_{ci}$:

$$C_s \approx 5 \times 10^4\mathrm{m/s} \qquad g \approx 5 \times 10^9\mathrm{m/s}^2 \qquad \gamma \approx 5 \times 10^5\mathrm{s}^{-1} \qquad \rho_s \approx 10^{-3}\mathrm{m/s}.$$

Values for the Rayleigh and Prandtl number are then given with Ra $\approx 6 \times 10^5$, Pr ≈ 20 and the dimensional sheath dissipation parameter evaluates as $\sigma \approx 2$. With a Rayleigh number

this large, the blobs maximum velocity will be independent of dissipative forces. Note that with these units, we can identify the unit velocity with 5km/s and the ideal interchange time with 2×10^{-6}s in the simulation results for small blob amplitude. Results from the non-linear model can be identified with dimensional quantities if we identify unit velocity with 7km/s and the ideal interchange time with 1.5×10^{-6}s.
Using these values, the results in Sec. 4 read, that the blob approaches a limiting maximum velocity of 4.5km/s. This velocity reduces according to Fig. 43 to 0.45m/s, if we assume a sheath-connected regime.
For the non-linearized model and neglecting sheath dissipation, we read a maximum radial blob velocity of 4km/s from Tab. 14. Our simulations show that the blob assumes this velocity after 10×10^{-6}s. If we take sheath dissipation into account, simulation data from Fig. 61 give a maximal blob radial velocity of between 70 and 700m/s. As we lack simulation data for $\hat{\eta} = 0.5$ we only predict it lies in between the velocity for blobs with $\hat{\eta} = 0.2$ and $\hat{\eta} = 1.0$.

The such obtained results agree favorable with experimental findings. In [33], blob motion were measured in the NSTX tokamak by a gas puff imaging method. They measure radial blob velocities in the range of 0 - 2km/s.
When comparing values from the simulations with sheath dissipation to experimental values, we have to be cautious. Experimental findings suggest a limited correlation length of the structures along the field lines, as shown in [20]. They present gass puff images from a camera pointing radially inwards into the Alcator C-Mod tokamak. In Fig. 2 of their paper we can see, that the turbulent structures have a limited extension along the magnetic field lines. Our model equations on the other hand are for field-line averaged quantities. They imply structures along the field line that extend uniformly over the connection length $L_{\|}$. Along the magnetic field lines, plasma is transported with velocities only little different than C_s. With typical cross field transport velocities for the blobs we find, that $L_{\|}/C_s = 100 \times l\ v$. Here l denotes the blobs characteristic length and v is the blobs radial velocity. This means, that the blob has travelled one blob length radially outwards, before the structure can extend over one connection length. This demonstrates a competition between the blobs radial motion outover and a stretching along the magnetic field line. Clearly, field line averaged model equations are only an apt model, when the filament elongates over the full connection length. The time after which this criterion is fulfilled depends sensitively on the plasma and confinement parameters.

ELM filaments Plasmas confined with the high confinement mode are subject to a quasiperiodic destruction of the edge transport barrier. The characteristic steep radial density gradient relaxates and causes the formation of field-line elongated filaments that transport energy and particles out of the plasma. Radially outward travelling ELM filaments have been experimentally measured with velocities in a range between 1 and 10km/s. Other measurements determining filament sizes perpendicular to the magnetic field of 1 - 5cm. Our discussion of the simulation results compared to experimental ELM measurements is analog to the previous section. We first present typical parameters in the SOL for plasmas in high confinement mode:

Typical edge region plasma parameters for a plasma in high confinement mode are taken to be

$$\begin{aligned} n \approx 10^{19}\mathrm{m}^{-3}, \qquad T_e = 50\mathrm{eV} \qquad T_i = 100\mathrm{eV} \\ R \approx 2\mathrm{m}, \qquad B \approx 2\mathrm{T} \end{aligned} \tag{81}$$

and ELM filament dimension are taken to be

$$l \approx 0.02\mathrm{m} \qquad \hat{\eta} \approx 5.$$

These values are taken from [15]. ELM filaments show a large particle density perturbation amplitude. This implies that the linearized model makes qualitatively better predictions for ELM dynamics than the non-linearized model.

Still, applying the results from the non-linearized model is problematic in several ways. First, do the plasma parameters vary considerably between tha background plasma and the ELM peak particle density as we assume $\hat{\eta} \approx 5$. The electron ion collision frequency increases by a factor five, implying different diffusion parameters in the ELM particle density peak and the background plasma. Further will one expect large gradients in both, temperature and density which suggests an independent treatment of the two gradient fields. This requires a separate evolution equation for the temperature as an independent variable.

Keeping in mind these limitations when we compare our results to ELM measurements, we evaluate the dimensional parameters as:

$$C_s \approx 8 \times 10^4\mathrm{m/s} \qquad g \approx 7 \times 10^10\mathrm{m/s}^2 \qquad \gamma \approx 10^6\mathrm{s}^{-1} \qquad \rho_s \approx 10^{-3}\mathrm{m/s}.$$

Again, we evaluate the Rayleigh and Prandtl number as well as the dimensionless sheath dissipation parameter, Ra $\approx 2 \times 10^7$, Pr ≈ 10 and $\sigma \approx 3$. Evaluating these parameters at the peak particle density yields a lowered Rayleigh number of Ra $\approx \times 10^6$ as well as a lowered sheath dissipation parameter $\sigma \approx 2$. The Rayleigh number at the peak particle density is still well in the ideal regime. Note that the dimensionless sheath dissipation parameter is larger than in the case for SOL turbulence. This implies the importance of sheath currents for radial ELM dynamic. The results from the linearized model can be transfered into dimensional number by identifying unit velocity with 25km/s and one ideal interchange time with 7.5×10^{-7}s. This yields a velocity of 22.5km/s for SOL structures in the ideal regime from Fig. 43. This velocity is reduced to 2.5km/s if we consider sheath currents. Results from simulations for the non-linearized model suggest radial blob velocities in the sheath-detached regime of 30km/s which reduces to 1.5km/s if we account for a sheath dissipation parameter of $\sigma = 3$.

Comparison to experimental scaling properties of ELMs Finally, we discuss experimentally found scaling properties of ELMs and compare them to our presented results. A scaling of the blob radial velocity with its amplitude has been suggested in [15]. Probe measurements in experiments have indicated, that radial ELM filament velocity increases with ELM filament amplitude, [32]. Recent experiments in ASDEX upgrade present a comprehensive study of radial ELM filament velocity, [31]. They find that the radial filament velocity scales as $v_{\mathrm{rad}} \sim \sqrt{l}\sqrt{\hat{\eta}}$. As the $\sqrt{l}$ dependence is not in compliance with blob motions in a sheath connected regime, the found scaling with $\hat{\eta}$ agrees favorable with our presented scaling obtained for blobs in the sheath connected regime. On the other hand, do our numerical results suggest an inverse square scaling of the blobs radial velocity with increasing blob length. The results presented in this article also show a broadening in the radial direction of the filament extension. This complies with our simulation results for blobs in the sheath connected regime.

8.5.1 Discussion of secondary instabilities

We discuss the secondary instabilities observed in blob simulations. We compare them qualitatively to simulations of isolated instabilities.

Kelvin-Helmholtz instability For low collisional dissipation, blob simulations present a curled up lobes that show the formation of eddies. These are characteristic for the Kelvin-Helmholtz instability. The same characteristic eddies are observed in simulations of the isolated vorticity double layer. In Fig. 8.5.1 both simulations. At $t = 15.0$ we see that the vorticity double layer at presents a gradient and a small perturbation from its smooth curvature. At 20 ideal interchange time units, the region with the initial mild perturbation of the vorticity double layer is dominated by large turbulent fluctuations in vorticity. We find eddies or vorticity eyes, the vorticity double layer has no recognizable coherent structure. By counting the eddies we find, that the dominant wavelength of the initial perturbation is large. Simulations of an isolated vorticity double layer, contour plots Fig. 72(e) - Fig. 72(h), show a similar character. We find that a small initial perturbation in the vorticity double layer leads to the evolution of vorticity eddies similar in character to those we find in blob simulations. The time it takes for the instability to grow is much larger than in blob simulations. This may be attributed to the small perturbations via the initial conditions. The vorticity perturbation amplitude used in simulations is 1 % from its peak value, blob simulations show a larger vorticity gradient in the parts of the lobes that are subject to the Kelvin-Helmholtz instability. Our simulation show, that a perturbed vorticity double layer is responsible for the Kelvin-Helmholtz instability observed at the lobes of blob simulations. Computed growth rates of the instability from Fig. 65 showed that the power from perturbations with small wavelength are quickly dissipated to the other Fourier modes. Blob simulations suggest, that the initial wavelength that perturbs the vorticity double layer in the lobes is large.

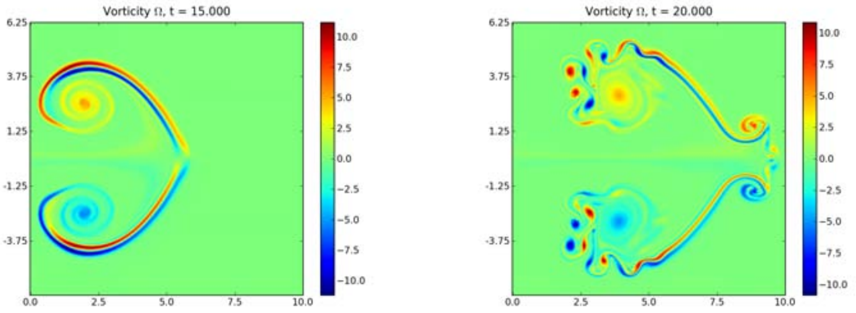

(a) Vorticity Ω, $t = 15.0$ (b) Vorticity Ω, $t = 20.0$

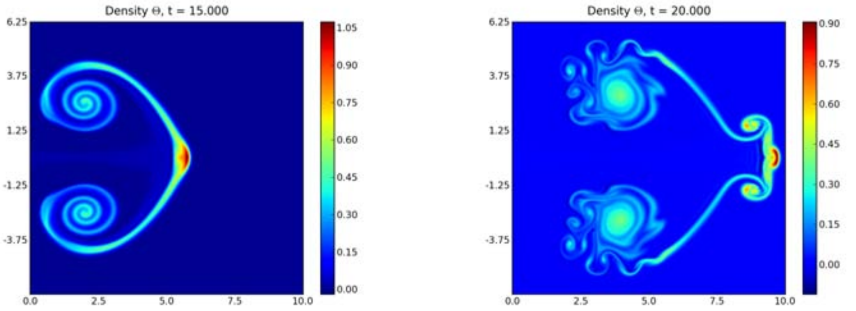

(c) Vorticity θ, $t = 15.0$ (d) Vorticity θ, $t = 20.0$

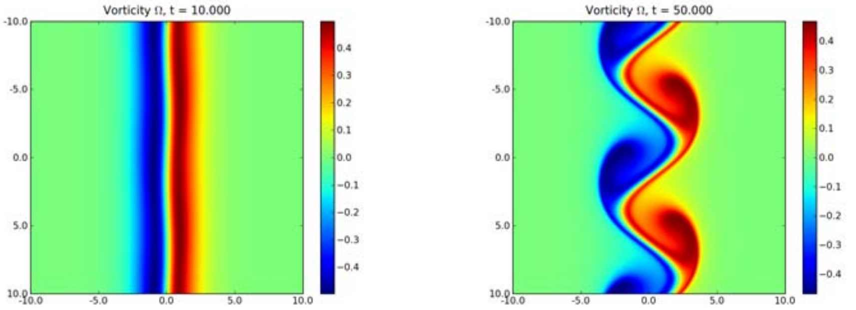

(e) Vorticity, Ω, $t = 10.0$ (f) Vorticity, Ω, $t = 50.0$

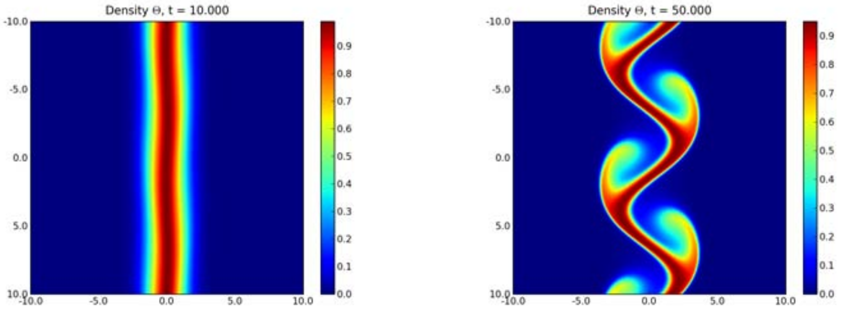

(g) Vorticity, θ, $t = 10.0$ (h) Vorticity, θ, $t = 50.0$

Figure 72: Late evolution of simulation for small blob amplitude with Ra $= 10^6$, Pr $= 1$ compared to evolution of an isolated vorticity double layer. Simulation # 9 from Tab. 10. Double layer initial wavelength $\lambda = 2$ and Ra $= 10^6$, Pr $= 1$.

Rayleigh-Taylor instability In simulations with low collisional diffusion and viscosity we find that the blob front is unstable to the Rayleigh-Taylor mode. See for example simulations with a blob amplitude $\hat{\eta}\ = 1.0$ and a sheath dissipation parameter $\sigma = 10$ in Fig. 57, or simulations for small blob amplitude and $\sigma = 1$ in Fig. 35. The front of the blob develops in both simulations a light curvature which leads to vertical particle density gradients.

In Fig. 8.5.1 we compare a simulation with an unstable front explicitly to simulation results of the Rayleigh-Taylor instability. We see that the blob simulation features horizontal particle density gradients and that the vorticity has asymmetric around the axis $y = 0$. The vertical velocity sheath in Fig. 73(a) develops kinks in the radial outward direction as seen in Fig. 73(b). Over the same time we observe that the front is unstable and emitts a secondary blob.

A direct comparison to the vorticity and particle density evolution for the isolated Rayleigh-Taylor instability shown in Fig. 73(e) - Fig. 73(h) strongyl suggests, that the instability observed in blob simulations is the Rayleigh-Taylor mode.

Most simulations presented in this thesis that are unstable to the Rayleigh-Taylor mode have an initial perturbation wavelength that has one crest. In Fig. 59 we present a simulation that features a blob that is split in the middle and seems to reconnect in the middle, as if flowing around an obstable. This behavior is presented elsewhere in the literature, [10]. Simulations in this paper suggest that the blobs bifurcates completely. This instability is called the finger instability. Surface plots from the vorticity show a different vorticity profile than we find for simulations of a perturbed particle density sheath which are unstable to the Rayleigh-Taylor mode. It is most likely due to the growth of a mode with $k_y \neq 0$ at the blob front.

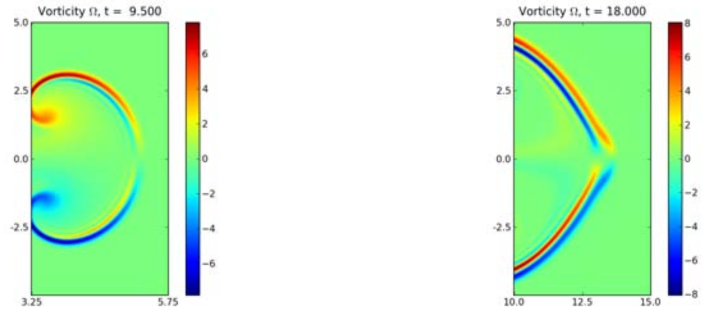

(a) Vorticity Ω, $t = 9.5$ (b) Vorticity Ω, $t = 18.0$

(c) Particle density θ, $t = 9.5$ (d) Particle density θ, $t = 18.0$

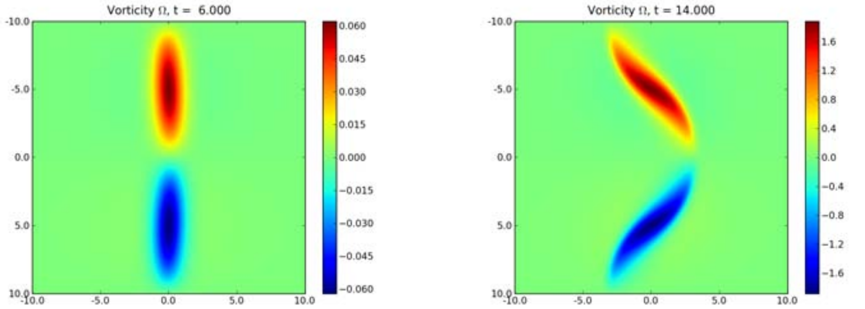

(e) Vorticity Ω, $t = 6.0$ (f) Vorticity Ω, $t = 14.0$

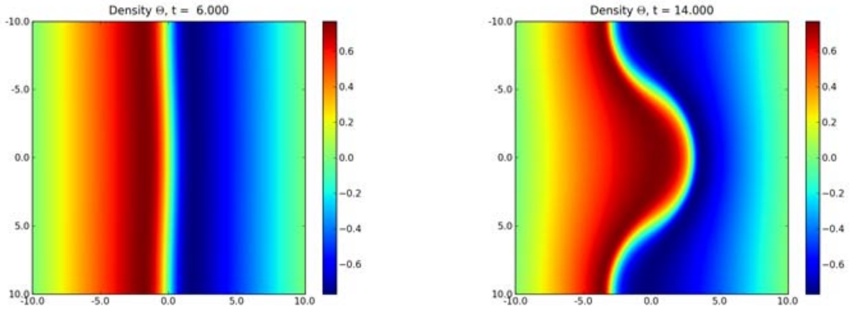

(g) Particle density θ, $t = 6.0$ (h) Particle density θ, $t = 14.0$

Figure 73: Comparison of blob front evolution for a simulation with $\hat{\eta} = 1.0$, # 7 from Tab. 14 compared to evolution of isolated particle density gradient with initial perturbation $\lambda = 1$ and Ra $= 10^6$.

We now discuss relevant issues with the numerical method used. We focus on aliasing where we also discuss mass conservation of the implemented spectral method. We present an alternative method to quantify finite size effects.

8.6 Aliasing

The results of the presented numerical simulations have all been achieved without compensating for aliasing. The aliasing error has briefly been described in Sec. 3.3. As discussed, it is a effect of the finite resolution we use in Fourier space that leads to the Fourier coefficients for a modes having erroneous contributions from other modes. With the Parseval theorem

$$\sum_{k_x=-N_x/2}^{k_x=N_x/2-1} \sum_{k_y=-M_y/2}^{k_y=M_y/2-1} |\widehat{u}_{\mathbf{k}}|^2 = \frac{1}{N_x M_y} \sum_{n=1}^{N_x} \sum_{m=1}^{M_y} |u(x_n, y_m)|^2$$

we see, that the aliasing error directly translates into mass conservation for the field u. This says, that we can estimate the aliasing error by the change in mass for the field u. As an estimate for the aliasing error we study the diagnostic output *thetaint* .

Mass conservation for simulations of the linearized interchange term model are presented in Fig. 74. We see that θ is conserved to machine accuracy.

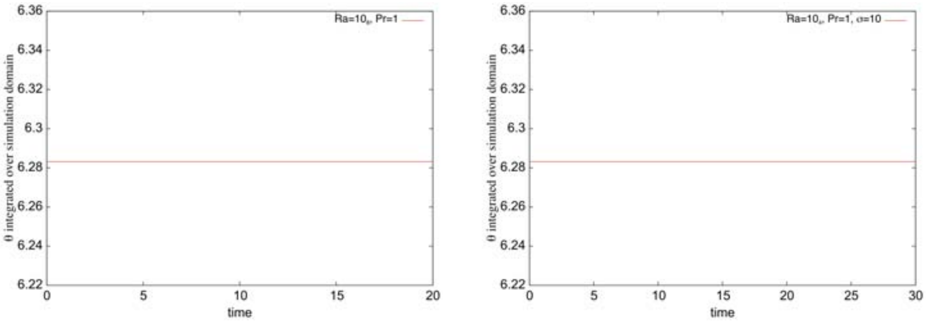

(a) *thetaint* for a simulation with $\mathrm{Ra} = 10^8$, $\mathrm{Pr} = 1$, simulation #12 from Tab. 10.

(b) *thetaint* for a simulation with $\mathrm{Ra} = 10^4$, $\sigma = 10$, simulation #20 from Tab. 5.2.

Figure 74: Integrated field variable θ for simulations of the linearized model and large Rayleigh number.

We see that the integral of the particle density perturbation, θ is conserved to machine accuracy. It also shows, the aliased Fourier coefficients have small absolute value. These modes represent base functions with small wavelengths which are used to describe features of the simulated structure with small spatial extend. A low aliasing error shows that the simulations are well resolved.

Simulations of the non-linearized model require the computation of additional convolution sums for θ, as discussed with Eqn. (45). To discuss the aliasing error, we define the quantity $Q(t) = \sum_{m,n} |\theta(x_n, y_m, t)|^2$, which is the same, as the sum over the squares of the Fourier coefficients, $\widehat{\theta}$. In Fig. 75, we present the evolution of $Q(t)/Q(t=0)$ compared to the evolution of $\max(V_\mathrm{X})$. For values $\hat{\eta}\ = 1.0$, we read, that the aliasing error is negligible, Q remains constant over the whole simulation. Increasing $\hat{\eta}\ = 10$, we find that Q decreases for $t \leq 0.4$ and then begins to increase significantly only after V_X reached its peak. The same behavior can be read from Fig. 75(b), for $\hat{\eta}\ = 100$ and $\hat{\eta}\ = 1000$. This shows, that an increased mass due to aliasing error has little influence on analysis depending on $\max(V_\mathrm{X})$.

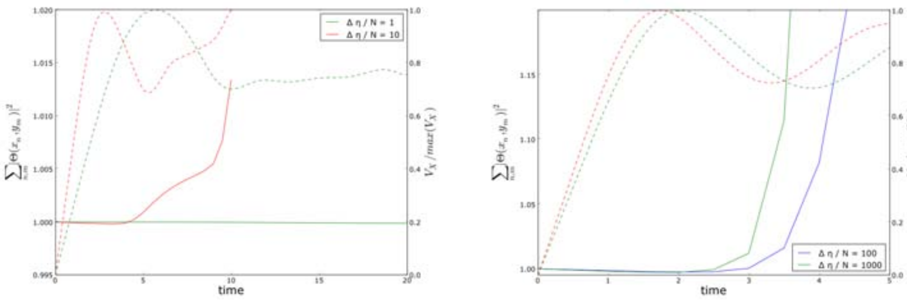

(a) Variation in Q for simulations of the three-parameter model.

(b) Variation in Q for simulations of the three-parameter model.

Figure 75: Integrated field variable θ for simulations of the non-linearized model. All simulations have $\kappa = \mu = 10^{-3}$ in units of the model. Time units are in simulation time units.

8.7 Finite size effects

The discussions of the convergence with respect to simulation domain size show, that the artificial zero crossing of ϕ at the domain boundary has significant influence on $\max(V_\mathrm{X})$. To further elucidate this behavior we note, that the that the initial vorticity profile generated by a plasma blob has a dipole structure, as shown in Fig. 9(b), Sec. 4. Since we close the model equations with the Laplace equation, $\Omega = \nabla^2\phi$, we have that ϕ behaves like a dipole potential and decays algebraically as $|\phi(r)| \propto 1/r^2$ for $r \to \infty$. When there is no initial flow present, the initial vorticity profile is generated by:

$$\begin{aligned} \frac{\partial\Omega}{\partial t} \rightarrow \frac{\Omega^{i+1} - \Omega^{i}}{\Delta_t} &= \frac{\partial}{\partial y}\theta \\ \Omega^{i+1} &\propto \frac{\partial}{\partial y}\theta. \end{aligned}$$

For an gaussian initial particle density profile, this shows that both θ and Ω decay geometrically, while ϕ decays algebraically. This is in agreement with experiments where measurements of structures propagating radially outwards in the SOL show the characteristics of a dipole field, which has the same spatial length as the characteristic length scale of the blob, [20].

One can use this, to determine the goodness of convergence with respect to the simulation

domain by fitting a function $p(y) = \alpha \times \phi^{\beta}$ to ϕ along the radial direction. The dipole moment of ϕ is along the poloidal direction, in this direction the monopol moments of ϕ still give a significant contribution.
We proceed by analyzing simulations #4 - # 12 from Tab. 7 with this method. The fit parameter β is presented in Fig. 76(a), we used the residuals squared per degree of freedom as an error estimate and find that the determined parameters are practically exact. The result show, that for a domain size of 100×100, the dipole character for ϕ is eminent and that an increased simulation domain of 200×200 has little influence on the radial decay of ϕ. We find a value lower than -2 because Ω is not a mathematical dipole. Since higher multipole moments decay even faster than r^{-2} it is unlikely that we observe a significant contribution from them.

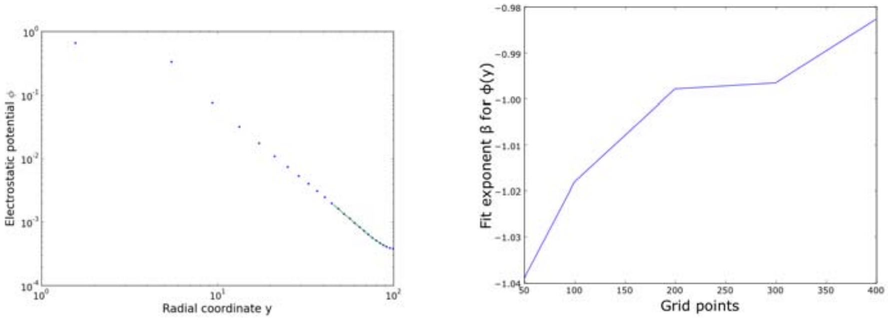

(a) Least sqaures fit to the electrostatic potential along the radial direction. Data from simulation #4 , Tab. 7 with Ra $= 10^2$, Pr $= 1$ and $t = 7.0$, every 10th data point is drawn.

(b) Fit exponent β for increasing simulation domain size.

Figure 76: Dipole fit to decaying electrostatic potential. Simulations with Ra $= 10^2$, Pr $= 1$, #2 – #6 from Tab. 7.

9 Conclusion

In this thesis we have presented numerical studies of a two-field model for radial transport of filament structures in the SOL of toroidal plasma confinement devices. For this we developed a spectral method to solve a system of non-linear partial differential equations. Comparison to previous numerical results show an excellent agreement with the method we developed. By running extensive convergence studies, we quantify the influence of finite size effects and spectral resolution on the diagnostic output of the code. Further was the code parallelized with `OpenMP` . This allows the code to run significantly faster on modern multiprocessor CPUs. Binary output implemented with `HDF5` 5 allows an efficient storage of large data output.

We present a detailed derivation of the model equations starting from the momentum equation of fluid dynamics. By linearizing the model equations for a small blob amplitude, we motivate a reduced model with a reduced parameter set.

A parameter study for blobs with low amplitude where we vary the diffusion parameters of the model is presented. We discuss radial interchange motions over a broad range of diffusion parameters and identify secondary instabilities that have length scales comparable to the blobs characteristic length scale. We reconstruct a known velocity scaling for the radial blob velocity in the limit of weak collisional diffusion and viscosity. In this limit, the blob structure approaches a limiting velocity that is proportional to the ion acoustic velocity times the square root of the blob amplitude relative to the background plasma and proportional to the square root of the blobs characteristic length scale.

A parameter study for simulations of radial blob motion with large amplitude blobs verify the scaling of the radial velocity proportional to the square root of the blob for small amplitudes. This scaling is valid for blob amplitudes smaller than unity only. For larger blob amplitudes we find a scaling that is proportional to the blob amplitude with an exponent of about 0.15.

The effects of sheath dissipation on blob dynamics for small and large amplitude blobs is studied and compared to experimental findings. The numerical results show that dissipative effects due to sheath parallel currents give a significant dampening of the radial blob velocity. We find that the limiting velocity the blob approaches in the limit of small collisional dissipation is proportional to the inverse of the sheath dissipation parameter. Translating these results to dimensional units, we find that this implies that the maximal radial blob velocity is proportional to the inverse square of the blob characteristic length. This finding is found for simulations of both models.

We also verify the scaling predicted by the analytic blob solution numerically. But we also find that the pre factor of the analytic blob solution grossly overestimates radial blob velocities. This indicates the importance of vorticity dynamics, which are neglected in the analytical solution.

Secondary instabilities have been identified in blob simulations, and by isolated simulations of their supposed driving mechanism it could be verified that the Kelvin-Helmholtz mode is driving eddies in the blob lobes and that the blob front is unstable to the Rayleigh-Taylor mode. Numerical simulations identify a vorticity double layer as the source for the observed instability at the blobs lobes. Diffusion has a dampening effect on this instability as small scale structures diffuse quickly. Numerical simulations show that for small dissipative forces, the blob emits secondary structures from the front causing a large radial elongation of the structure. Via comparison to simulations of an isolated particle density front with a perturbation localized in the radial direction, we showed, that this mechanism can be attributed to the Rayleigh-Taylor instability.

Suggestions for future work The developed spectral code shows a good performance in simulations of small scale structures on a bi-periodic domain. Further use of the code might include simulations of other turbulent structures in the SOL.
The comparison between our results and experimental findings confirms the importance of sheath dissipation as an dissipation mechanism in the blob model. With field line averaging we include sheath dissipation by a zero-dimensional approximation. This implies that the filament simulated extends homogenously over the connection length. This is neither observed for radial structures associated to SOL turbulence nor for ELM filaments travelling radially outwards, both have a finite correlation length along the field lines. To give a more accurate picture, future work might include a more detailled description of field-parallel dynamics. By including a dynamic variable for the sheath-parallel currents, a more realistic model can be obtained. This would help estimate radial filamentary motion in the SOL of future fusion reactors, as ITER.

A The interchange instability

Blob motion discussed in this thesis is generated by the interchange mechanism. This mechanism is not distinct to blob motion, but has been well known. The fundamental innovation with the blob mechanism is to apply the interchange mechanism to this special setting. In this section we commpare the interchange mechanism driving radial motion in toroidal confined plasmas to the interchange motion in classical hydrodynamics.

A.1 Interchange mechanism for blob dynamics

In radial confinement devices, one observes plasma filaments, with excess plasma pressure and particle density. In the cross section in the radial – poloidal drift plane, perpendicular to the field lines, they are an isolated, blob like structure, as presented in Fig. 77.
In the toroidal confinement devices, the magnetic curvature vector $\underline{\kappa}$ and the magnetic field gradients $\nabla \ln B$ point both radially inwards. They cause guiding center drifts according to Eqn. (20) that are in opposite direction for the negatively electrons and positively charged ions. These currents cause a vertical polarization of the blob structure as shown in Fig. 77. The polarized blob structure is then advected radially outwards by a $E \times B$ drift, that is uniform regardless of particle charge.

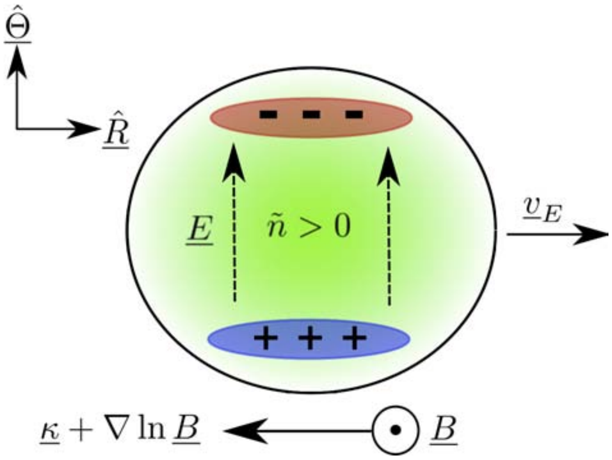

Figure 77: Driving forces of the interchange mechanism for an isolated density blob in a magnetized plasma. The bulk structure is transported radially outwards.

A.2 Analogy to classical hydrodynamics

The key feature of the interchange model is the creation of vorticity by vertical particle density gradients, via the $\frac{\partial}{\partial z} n$ term in the vorticity equation of the two field model, Eqn. (26). In classical hydrodynamics we find a similar mechanism, called baroclinic generation of vorticity. We describe this mechanism briefly to elucidate the nature of the interchange mechanism.
Let us begin with the Naver-Stokes equation for incompressible fluids:

$$\left(\frac{\partial}{\partial t} + \underline{v}\cdot\nabla\right) = -\frac{1}{\rho} + g + \nu\nabla^2\underline{v} \tag{82}$$

$$\tag{83}$$

taking the curl of it, and using $\underline{v}\cdot\nabla\underline{v} = \nabla\frac{1}{2}\underline{v}\cdot\underline{v} - \underline{v}\times(\nabla\times\underline{v})$, we get:

$$\nabla\times\left(\frac{\partial}{\partial t} + \underline{v}\cdot\nabla\right) = -\nabla\times\frac{1}{\rho}\nabla p + \nabla\times\underline{g} + \nu\nabla^2\nabla\times\underline{v} \tag{84}$$

$$\Leftrightarrow \left(\frac{\partial}{\partial t} + \underline{v}\cdot\nabla\right)\Omega = \underbrace{(\Omega\cdot v)\underline{v}}_{1} + \underbrace{\frac{1}{\rho^2}\nabla\rho\times\nabla p}_{2} + \underbrace{\nu^2\nabla^2\Omega}_{3}. \tag{85}$$

We see that there are three contributions to the generation of vorticity.

1. Vortex stretching. This is characteristic to fluids in three dimensions. An increase of the fluids velocity along the direction of the vorticity, increases the vorticity.
2. Baroclinic generation of vorticity. Whenever pressure and density gradients are not parallel, there is a generation of vorticity in this point. When surfaces of constant pressure and density are parallel, no vorticity is generated. Note, that for fluids where pressure is a function of density, $p = p(\rho)$, this term vanishes since $\rho = \text{const} \Rightarrow p = \text{const}$ holds.
3. Collisionality does also affect vorticity generation.

Recall that in a static equilibrium, the density gradients in a fluid are parallel to the gravity:

$$\nabla p = \rho\underline{g}.$$

Baroclinic generation of vorticity is elementary in fluid dynamics. Next we explain a typical setting in which we find the mechanism. The mechanism is seen in Fig. 78. It shows a fluid denisty agglomeration with gradients pointing radially inward to the center of the fluid density agglomeration. Gravity and pressure gradient point downwards. On the left and the right side are drawn to arrows denoting local fluid density gradients. They cause a generation of vorticity Ω denoted by the arrow pointing in and out of the domain. This creates a circular velocity field, depicted by the circular arrows for the fluid velocity $\underline{v}$.

A setting where this mechanism is important, is for liquids with temperature gradients, as presented in Fig. 79. Assume that we have a fluid in a glass whose temperature T is kept at T_0 at the top and at $T_0 + \Delta T$ at the bottom, where $\Delta T > 0$ and a density of $\rho_0 + \Delta\rho$ at the top and ρ_0 at the bottom. The fluid at the bottom is warmer and thus the thermal motion of the particles are larger – the fluid tries to expand. At the top the fluid is colder, here the fluid will be compressed.

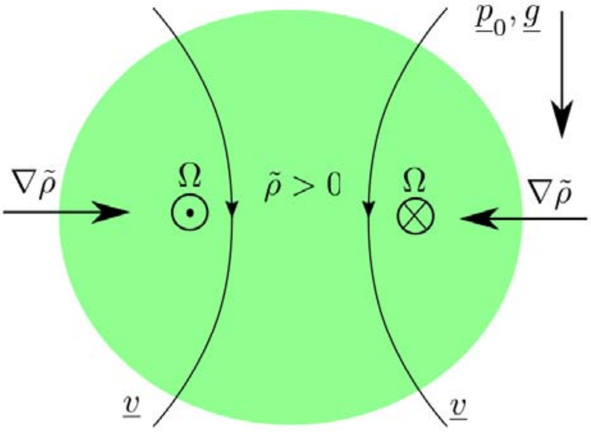

Figure 78: Scetch of baroclinic generation of vorticity for a local density perturbation $\tilde{\rho}$. Density gradients leading to the center of the perturbation create vorticity via $\nabla p \times \nabla \rho$.

The mechanism presented above is responsible for the development of larger convection cells as they are found often in nature. On Jupiter one observes large thermal convection cells, as pictured in Fig. 79) for example. Instead for density it is temperature that is transported by baroclinic generation of vorticity, but the mechanism by which the transport occurs is the same.
In the interchange model, the $\frac{\partial\theta}{\partial y}$ term takes the role of the baroclinic term in Eqn. (85)). In the two field models, the $E \times B$ drift causes a collective motion of the structure and can be seen as an effective gravity. In the dimensional linear two fluid model, Eqn. (36)), the factor of the interchange term is $\frac{2P}{\rho R}$. The acoustic velocity in an ideal gas is given with $C_S = \sqrt{P/\rho}$, defining the effective gravity

$$g = 2\frac{C_S}{R} \tag{86}$$

the interchange term in the two field model equations can be written with the same factor g as the baroclinic vorticity term in Eqn. (85). This shows the analogy between generation of vorticty by diamagnetic drift compression in the two field model we are working with, and baroclinic generation of vorticity in classical hydrodynamics.

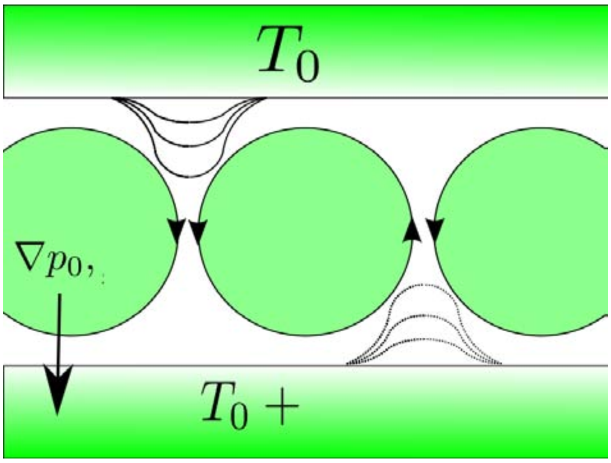

Figure 79: Illustration of large scale convection cells for temperature. Temperature is transported from the warm bottom to the cold top via large scale convection cells that form due to baroclinic generation of vorticity. The full and dashed profile line indicate how temperature from the reservoirs is convected along the circular convection cells.

References

[1] May 2010.

[2] 2dads documentation. 2dads documentation.

[3] Ghassan Y. Antar, Glenn Counsell, Yang Yu, Brian Labombard, and Pascal Devynck. Universality of intermittent convective transport in the scrape-off layer of magnetically confined devices. *Physics of Plasmas*, 10(2):419–428, 2003.

[4] A. Arakawa. Computational design for long-term numerical integration of the equations of fluid motion. *Journ. Comp. Phys.*, 1:119–143, 1966.

[5] A. Y. Aydemir. Convective transport in the scrape-off layer of tokamaks. *Physics of Plasmas*, 12(6):062503, 2005.

[6] N. Bian, S. Benkadda, J.-V. Paulsen, and O. E. Garcia. Blobs and front propagation in the scrape-off layer of magnetic confinement devices. *Physics of Plasmas*, 10(3):671–676, 2003.

[7] J. A. Boedo, D. L. Rudakov, E. Hollmann, D. S. Gray, K. H. Burrell, R. A. Moyer, G. R. McKee, R. Fonck, P. C. Stangeby, T. E. Evans, P. B. Snyder, A. W. Leonard, M. A. Mahdavi, M. J. Schaffer, W. P. West, M. E. Fenstermacher, M. Groth, S. L. Allen, C. Lasnier, G. D. Porter, N. S. Wolf, R. J. Colchin, L. Zeng, G. Wang, J. G. Watkins, and T. Takahashi DIII-D Team. Edge-localized mode dynamics and transport in the scrape-off layer of the diii-d tokamak. *Physics of Plasmas*, 12(7):072516, 2005.

[8] S.I Braginskii. Transport processes in a plasma. *Review of Plasma Physics*, 1:205–311, 1965.

[9] A. Quarteroni C. Canuto, M.Y. Hussaini and T.A. Zang. *Spectral Methods in Hydrodynamics*. Springer Verlag, 1987.

[10] S.I. Krashenninikov D.A. D'Ippolito, J.R. Myra. Blob transport in the tokamak scrape-off layer. *Contrib. Plasma Phys*, 44(1-3):205–216, 2004.

[11] D. A. D'Ippolito and J. R. Myra. Blob stability and transport in the scrape-off-layer. *Physics of Plasmas*, 10(10):4029–4039, 2003.

[12] D. A. D'Ippolito, J. R. Myra, and S. I. Krasheninnikov. Cross-field blob transport in tokamak scrape-off-layer plasmas. *Physics of Plasmas*, 9(1):222–233, 2002.

[13] Matteo Frigo and Steven G. Johnson. The design and implementation of FFTW3. *Proceedings of the IEEE*, 93(2):216–231, 2005. Special issue on “Program Generation, Optimization, and Platform Adaptation”.

[14] M. Israeli G. E. Karniadakis and S. A. Orszag. High-order splitting methods for the incompressible navier-stokes equation. *Journ. Comp. Phys.*, 97:414–443, 1991.

[15] O. E. Garcia, N. H. Bian, and W. Fundamenski. Radial interchange motions of plasma filaments. *Physics of Plasmas*, 13(8):082309, 2006.

[16] O. E. Garcia, N. H. Bian, V. Naulin, A. H. Nielsen, and J. Juul Rasmussen. Mechanism and scaling for convection of isolated structures in nonuniformly magnetized plasmas. *Physics of Plasmas*, 12(9):090701, 2005.

[17] O E Garcia, J Horacek, R A Pitts, A H Nielsen, W Fundamenski, J P Graves, V Naulin, and J Juul Rasmussen. Interchange turbulence in the tcv scrape-off layer. *Plasma Physics and Controlled Fusion*, 48(1):L1, 2006.

[18] O.E Garcia. Blob transoprt in the plasma edga: a review. *Plasma and Fusion Rsearch: Review Articles*, 4(019), 2008.

[19] O.E. Garcia, J. Horacek, R.A. Pitts, A.H. Nielsen, W. Fundamenski, V. Naulin, and J. Juul Rasmussen. Fluctuations and transport in the tcv scrape-off layer. *Nuclear Fusion*, 47(7):667, 2007.

[20] O. Grulke, J. L. Terry, B. LaBombard, and S. J. Zweben. Radially propagating fluctuation structures in the scrape-off layer of alcator c-mod. *Physics of Plasmas*, 13(1):012306, 2006.

[21] Per Helander and Dieter J. Sigmar. *Collisional Transport in Magnetized Plasmas*. Cambridge University Press, 2002.

[22] C. Hidalgo, B. Goncalves, C. Silva, M. A. Pedrosa, K. Erents, M. Hron, and G. F. Matthews. Experimental investigation of dynamical coupling between turbulent transport and parallel flows in the jet plasma-boundary region. *Phys. Rev. Lett.*, 91(6):065001, Aug 2003.

[23] J.P. Graves J. Horacek, R. A. Pitts. Overview of edge electrostatic turbulence experiments on tcv. *Czechoslovak Journal of Physics*, 55(3):271–283, 2005.

[24] N.P. Basse I Cziegler et eal J.L. Terry. Transport phenomena in the edge of alcator c-mod plasmas. *Nucl. Fusion*, 45:1321–3127, 2005.

[25] A. Kirk, H. R. Wilson, G. F. Counsell, R. Akers, E. Arends, S. C. Cowley, J. Dowling, B. Lloyd, M. Price, and M. Walsh. Spatial and temporal structure of edge-localized modes. *Phys. Rev. Lett.*, 92(24):245002, Jun 2004.

[26] S. I. Krasheninnikov. On scrape off layer plasma transport. *Physics Letters A*, 283(5-6):368 – 370, 2001.

[27] S. I. KRASHENINNIKOV, D. A. D'IPPOLITO, and J. R. MYRA. Recent theoretical progress in understanding coherent structures in edge and sol turbulence. *Journal of Plasma Physics*, 74(05):679–717, 2008.

[28] Micheal A. Lieberman and Allan J. Lichtenberg. *Principles of plasma discharges and materials processing*. Wiley-Interscience, 1994.

[29] A. Loarte, G. Saibene, R. Sartori, T. Eich, A. Kallenbach, W. Suttrop, M. Kempenaars, M. Beurskens, M. de Baar, J. Lönnroth, P. J. Lomas, G. Matthews, W. Fundamenski, V. Parail, M. Becoulet, P. Monier-Garbet, E. de la Luna, B. Gonçalves, C. Silva, Y. Corre, and Contributors to the EFDA-JET Workprogramme. Characterization of pedestal parameters and edge localized mode energy losses in the joint european torus and predictions for the international thermonuclear experimental reactor. *Physics of Plasmas*, 11(5):2668–2678, 2004.

[30] D L Rudakov, J A Boedo, R A Moyer, S Krasheninnikov, A W Leonard, M A Mahdavi, G R McKee, G D Porter, P C Stangeby, J G Watkins, W P West, D G Whyte, and G Antar. Fluctuation-driven transport in the diii-d boundary. *Plasma Physics and Controlled Fusion*, 44(6):717, 2002.

[31] A Schmid, A Herrmann, H W Müller, and the ASDEX Upgrade Team. Experimental observation of the radial propagation of elm induced filaments on asdex upgrade. *Plasma Physics and Controlled Fusion*, 50(4):045007, 2008.

[32] C. Silva, B. Goncalves, C. Hidalgo, K. Erents, A. Loarte, G. Matthews, and M. Pedrosa. Determination of the particle and energy fluxes in the jet far sol during elms using the reciprocating probe diagnostic. *Journal of Nuclear Materials*, 337-339:722 – 726, 2005. PSI-16.

[33] R.J. Maqueda et al S.J. Zweben. High-speed imaging of edge turbulence in nstx. *Nucl. Fusion*, 44, 2004.

[34] J. L. Terry, S. J. Zweben, K. Hallatschek, B. LaBombard, R. J. Maqueda, B. Bai, C. J. Boswell, M. Greenwald, D. Kopon, W. M. Nevins, C. S. Pitcher, B. N. Rogers, D. P. Stotler, and X. Q. Xu. Observations of the turbulence in the scrape-off-layer of alcator c-mod and comparisons with simulation. *Physics of Plasmas*, 10(5):1739–1747, 2003.

[35] F. Wagner, G. Becker, K. Behringer, D. Campbell, A. Eberhagen, W. Engelhardt, G. Fussmann, O. Gehre, J. Gernhardt, G. v. Gierke, G. Haas, M. Huang, F. Karger, M. Keilhacker, O. Klüber, M. Kornherr, K. Lackner, G. Lisitano, G. G. Lister, H. M. Mayer, D. Meisel, E. R. Müller, H. Murmann, H. Niedermeyer, W. Poschenrieder, H. Rapp, and H. Röhr. Regime of improved confinement and high beta in neutral-beam-heated divertor discharges of the asdex tokamak. *Phys. Rev. Lett.*, 49(19):1408–1412, Nov 1982.

[36] F Wagner and U Stroth. Transport in toroidal devices-the experimentalist's view. *Plasma Physics and Controlled Fusion*, 35(10):1321, 1993.

[37] W.T. Vetterlin B.P. Flannery W.H. Press, S.A. Teukolsky. *Numerical Recipes in C++*. Cambridge University Press, 2002.

[38] A. J. Wootton, B. A. Carreras, H. Matsumoto, K. McGuire, W. A. Peebles, Ch. P. Ritz, P. W. Terry, and S. J. Zweben. Fluctuations and anomalous transport in tokamaks. *Physics of Fluids B: Plasma Physics*, 2(12):2879–2903, 1990.

[39] Y H Xu, S Jachmich, R R Weynants, and the TEXTOR team. On the properties of turbulence intermittency in the boundary of the textor tokamak. *Plasma Physics and Controlled Fusion*, 47(10):1841, 2005.

[40] G. Q. Yu, S. I. Krasheninnikov, and P. N. Guzdar. Two-dimensional modelling of blob dynamics in tokamak edge plasmas. *Physics of Plasmas*, 13(4):042508, 2006.

[41] S. J. Zweben, D. P. Stotler, J. L. Terry, B. LaBombard, M. Greenwald, M. Muterspaugh, C. S. Pitcher Alcator C-Mod Group, K. Hallatschek, R. J. Maqueda, B. Rogers, J. L. Lowrance, V. J. Mastrocola, and G. F. Renda. Edge turbulence imaging in the alcator c-mod tokamak. *Review,Tutorial and Invited Papers from the 43rd Annual Meeting of the APS Division of Plasma Physics*, 9(5):1981–1989, 2002.